

Copyright
by
Michael D. Ryan
2006

**The Dissertation Committee for Michael David Ryan Certifies that this is the
approved version of the following dissertation:**

The Interaction of an Electrothermal Plasma with JA2 Solid Propellant

Committee:

Philip Varghese, Supervisor

Noel Clemens, Co-Supervisor

David Dolling

Laxminarayan Raja

John Howell

The Interaction of an Electrothermal Plasma with JA2 Solid Propellant

by

Michael David Ryan, B.S.

Dissertation

Presented to the Faculty of the Graduate School of

The University of Texas at Austin

in Partial Fulfillment

of the Requirements

for the Degree of

Doctor of Philosophy

The University of Texas at Austin

December, 2006

Acknowledgements

This dissertation would not have been possible without the support of the many people around me. I would first like to thank my advisors Philip Varghese and Noel Clemens for the chance to work on this project. Their insights and academic counsel throughout my six years here were invaluable. The knowledge I have learned from them will doubtless serve me well in my future career. I also am extremely grateful to all of my coworkers throughout my years here for all the fun times and great discussions we had at the lab. Specifically I would like to thank Pablo Bueno for being a true friend. I was lucky that he was the one grad student that was here during my entire stay in Texas. I extend my gratitude to Eddie Zihlman as well, for all his help at the lab.

I would like to thank my parents for their continuing love and support throughout my education. My mother's sound advice over the last six years was always appreciated, though I wish I had listened to her more. Most of all, I wish to thank my wife Devon for her unconditional love and patience during my time here. Without her companionship my years here would have been less rewarding. She was a steady force through all the ups and downs in my research, and was a constant reminder of my purpose here. Finally, I owe a special note of gratitude to my son Calvin, born 3 months ago, for providing the final impetus to finish this long journey.

The Interaction of an Electrothermal Plasma with JA2 Solid Propellant

Publication No. _____

Michael David Ryan, Ph. D.

The University of Texas at Austin, 2006

Supervisor: Philip Varghese

Co-Supervisor: Noel Clemens

Electrothermal plasmas are being studied as an ignition mechanism for solid propellants in large caliber guns. Benefits of electrothermal plasma ignition over conventional primer charge ignition include a reduction of ignition delay and delay jitter (bootstrapping) and compensation for the variable burn rate of propellants at different initial temperatures. When JA2 solid propellant is exposed to plasma radiation alone, significant decomposition results. This radiative interaction is a possible mechanism that causes the bootstrapping and temperature compensation. In addition, the effects of plasma radiation exposure have the potential to increase the propellant burn rate. To characterize this radiation interaction, PLIF imaging of NO, a JA2 decomposition product, was conducted at the propellant surface. Also, simultaneous high speed video of the propellant surface and scattering of ejected particles has been performed. During the radiation interaction scattering particles and NO appeared between 100 and 150 μs after the beginning of the discharge and propagated away from the propellant surface. This ejected material appeared in identifiable structures that are irregular in shape and

distribution. This suggests that the material was ejected at semi-discrete locations on the surface rather than diffused uniformly from the surface. During the plasma firing the propellant surface changed markedly by forming irregularly shaped decomposition structures that grew in size over the course of the discharge. No correlation was observed between the structure of the ejected material and the decomposition structures formed on the propellant surface during the discharge. After the plasma discharge, the propellant continued to react, with bubbles forming on the surface up to 9 ms after the discharge finished. These bubbles are probably the largest decomposition structures in images taken of the propellant surface minutes after radiation exposure. The delayed reaction of the propellant produced the majority of ejected particles after the plasma firing. This raises concerns that the potential burning rate increase by the effects of the radiation might not be completely realized in a plasma ignition event. Regions of the propellant exposed to plasma radiation could be consumed by the burning surface before all of the observed effects of the radiative interaction took place.

Table of Contents

List of Tables	ix
List of Figures	x
List of Figures	x
Chapter 1: Introduction	1
Motivation	1
Project Overview	3
Chapter 2: Literature Review	7
Electrothermal Plasmas	7
Solid Propellant Combustion	19
Solid Propellant Ignition	22
Plasma Propellant Interaction	25
Propellant Decomposition	40
Modeling of the plasma, propellant, and plasma propellant interaction	44
Chapter 3: Experimental Setup	49
Plasma production apparatus	49
Heat Flux Measurements	50
Plasma Radiation Chamber	52
Single Shot NO PLIF and PLMS Imaging	55
Simultaneous High Speed Propellant Imaging and PLMS	58
Chapter 4: Experimental Methodology and Background Theory	63
Current measurements using a Rogowski coil	63
Experiment Timing	66
Measuring Laser Sheet Width	70
Planar laser induced fluorescence Theory and Nitric Oxide Spectrum	73
Laser Calibration for NO PLIF	75
Camera Registration	77

JA2 Surface Scattering Spectra.....	82
Tracking Propellant Surface image changes.....	85
Cross-correlation of Propellant Surface and Laser scattering images	88
Chapter 5: Results and Discussion.....	91
Electrical characteristics of discharge circuit	91
Heat Flux Measurements	93
Plasma Radiation	97
Nitric Oxide PLIF	102
Laser Mie Scattering	106
Simultaneous Two Camera Imaging.....	109
Repeatability of Results over multiple firings	130
Chapter 6: Conclusions	137
Appendix A: Propellant Surface Temperature Measurements in Open Air Jet..	141
Experimental setup.....	141
Determination of Local Thermodynamic Equilibrium	143
Spectrometer Calibration	143
Results.....	147
Appendix B: Pressure Chamber Observations.....	152
Experimental Setup.....	152
Results.....	154
Appendix C: NO ₂ PLIF	161
References.....	163
Vita	172

List of Tables

Table A1: Copper emission lines used in temperature measurement.	142
Table B1: Changes made to create window of time where optical diagnostics was possible.	160

List of Figures

Figure 2.1: Principle features of quasi-steady plasma jet (Kim et al. 2002).....	8
Figure 2.2: Typical voltage and current traces for 5 kV initial capacitor charge (Kim et al. 2002).	9
Figure 2.3: Visible emission time history of plasma jet (Kohel et al. 1999).	10
Figure 2.4: Variation of the plasma temperature along the axis of the jet for several different time delays; the downstream coordinate is the axial position scaled by the Mach disk location (Kim et al. 2002).	17
Figure 3.1: Plasma jet firing assembly.....	50
Figure 3.2: Experimental diagram for heat flux measurements.....	52
Figure 3.3: Capillary enclosure and discharge chamber with window for plasma radiation.	54
Figure 3.4: NO PLIF laser setup.	56
Figure 3.5: Photograph of the NO PLIF and Nd:YAG PLMS experimental setup.	56
Figure 3.6: Experimental setup of the two camera simultaneous imaging experiment. ...	60
Figure 3.7: Close up view of two camera simultaneous imaging experiment.	61
Figure 3.8: Field of view geometry for both cameras a) Diagram of observer position for cross-plane plots b) Relationship of the camera fields of view for scattering and surface images.	62
Figure 4.1: Integrated voltage (\propto current) in Rogowski coil during plasma discharge with conductor inside coil, conductor outside coil, and the between the two.....	65
Figure 4.2: Calibrated current with and without error correction.	66
Figure 4.3: Experimental timing for a single trigger device.....	67
Figure 4.4: Experimental timing diagram for a 10 Hz laser experiment during a plasma firing.....	68
Figure 4.5: Experimental timing for 10 kHz laser.	70
Figure 4.6: Photodiode intensity as the knife edge is translated across the laser beam with error function fit and resulting Gaussian beam profile.	72
Figure 4.7: Laser beam profile from second razor translation using a higher spatial resolution.....	73
Figure 4.8: Diagram of a two level model for laser induced fluorescence.	74
Figure 4.9: Image of the two surface grid used for camera registration.	78
Figure 4.10: Image of the two surface grid by the laser scattering camera.	79
Figure 4.11: Image of the two surface grid through the mirror by the propellant surface camera.	79
Figure 4.12: Example of original camera images taken during a run. Top image: laser scattering. Bottom image: propellant surface.	81
Figure 4.13: Both camera images plotted onto single 3-D graph with laser swath and time delay marked.	82
Figure 4.14: Visible reflectance spectra of pristine and decomposed propellant.	84
Figure 4.15: Rescaled pristine reflectance spectrum rescaled to compare with the reacted reflectance spectrum.	84

Figure 4.16: Example images comparison technique: a) later image at 256 μ s b) earlier image at 236 μ s c) ratio image with threshold applied.	88
Figure 4.17: Diagram of method to produce vectors used in cross-correlation.....	90
Figure 5.1: Capillary current during the plasma discharge for two different setups.	92
Figure 5.2: Current, capillary voltage, and plasma energy deposition during the capacitor discharge with the radiation chamber setup.....	92
Figure 5.3: Time-dependent radiative heat flux measurements at several axial locations.	94
Figure 5.4: Time dependent conductive and convective heat flux calculated from radiative and total heat flux.....	95
Figure 5.5: Values of peak heat fluxes and time delay of heat fluxes with respect to downstream distance.....	96
Figure 5.6: Plasma radiation intensity measured by a fast response photodiode.....	98
Figure 5.7: Plasma emission spectra at a) 150 μ s b) 500 μ s	99
Figure 5.8: JA2 disc surface a) before, b) after plasma radiation exposure, and c) after open air plasma jet impingement	100
Figure 5.9: Semi-transparent JA2 propellant surface after exposure to plasma radiation during current study.	101
Figure 5.10: Geometry for camera field of view in NO PLIF and YAG PLMS experiments.	103
Figure 5.11: Time sequence of NO PLIF images created from separate firings. NO ejection structures are labeled.	104
Figure 5.12: Example image of tuning NO pump laser off absorption line at 500 μ s delay.	104
Figure 5.13: Time sequence of laser scattering composed of images from individual runs. Labels A and B mark smaller more common scattering structures and larger, brighter, less common scattering structures respectively.	109
Figure 5.14: Time series of propellant surface during the plasma discharge during 2 camera experiment. Delay times from the capacitor trigger are marked in the bottom left corner of each image. The label A marks a structure as it changes throughout the plasma discharge.	110
Figure 5.15: Example of difference image, with the two images used to calculate it. ...	113
Figure 5.16: Average intensity of propellant surface image using each window mask.	115
Figure 5.17: Average number of regions of change appearing over multiple runs.	116
Figure 5.18: Average percent of total image area covered by regions of change for each mask.	117
Figure 5.19: Average median size of regions of change over multiple runs.	118
Figure 5.20: Comparison between propellant surface images at a delay of a) 5 minutes after the plasma firing b) 836 μ s	120
Figure 5.21: Example time sequence of laser scattering images taken during the same run.	121
Figure 5.22: Example time series of propellant surface images and laser scattering images plotted together.	123

Figure 5.23: Example cross correlations between the propellant surface and laser scattering images.....	125
Figure 5.24: Example scattering image sequence after firing.....	127
Figure 5.25: Time sequence of close up view of bubble growing with corresponding propellant image. Bubble has been false colored light-blue and labeled “A”.....	129
Figure 5.26: A number of visible emission images of the plasma jet in open air taken at a delay of 150 μ s.....	131
Figure 5.27: Two emission spectra taken during separate firings of the plasma inside the radiation chamber at 150 μ s.....	132
Figure 5.28: Three NO PLIF images at 250 μ s delay.....	133
Figure 5.29: Two particle scattering images at 250 μ s delay.....	134
Figure 5.30: Average intensity per pixel of propellant surface images for individual runs.....	135
Figure 5.31: Number of regions of change on propellant surface for individual runs....	136
Fig. A1 Example false colored spectrometer image with corresponding integrated signal.....	144
Figure A2: Calibration curves of tungsten lamp intensity over a range from 350 to 730 nm.....	146
Figure A3: Plasma emission spectrum collected 3 mm from propellant surface at a delay of 60 μ s.....	148
Figure A4: Boltzmann plot of Cu emission lines at 60 μ s delay; inferred temperature 14,100 K.....	149
Figure A5: Variation of measured plasma temperature near propellant surface and absolute value of discharge current through capillary.....	150
Figure A6: Emission spectrum with 100 μ m fiber at a delay of 30 μ s.....	151
Figure B1: Closed combustion chamber with windows for viewing and laser access ...	152
Figure B2: Filler pieces assembled to fill the main chamber and the window recesses while providing laser and pressure transducer access.....	153
Figure B3: Visible-luminosity images during plasma-ignition of JA-2. The images were acquired at a framing rate of 13,500 frames per second.....	156
Figure B4: Pressure measurements inside the original chamber while plasma ignites the propellant.....	158
Figure B5: Example pressure traces during plasma ignition in 5 cm ³ chamber.....	159
Figure C1: Example NO ₂ PLIF image at 200 μ s.....	162

Chapter 1: Introduction

MOTIVATION

The army is currently researching gun applications that involve ignition of solid propellant by electrothermal (ET) plasmas instead of conventional primers. In a conventional tank gun cartridge the primer charge is ignited by a hammer blow. The burning primer propagates through a tube into a bed of stick propellant, which in turn is ignited and deflagrates, propelling the projectile down the bore. In electrothermal plasma ignition a plasma is created by discharging large capacitors through a plastic capillary. The resulting vaporized and ionized plastic then jets into and ignites the same propellant bed.

Such electrothermal-chemical (ETC) guns were originally seen as a compromise between electrothermal (ET) guns, which use plasma as the propellant, and conventional solid propellant guns. The higher temperature and lower molecular weight working fluid in an ET gun, having a higher speed of sound, drives the muzzle velocity higher than in a conventional gun. An ET launcher may approach velocities of 3 km/s while muzzle velocities with conventional ignition are about 1.6 km/s (Kaplan et al. 1993). However, the large amount of electrical energy required for ET designs is prohibitive because it necessitates the use of large banks of capacitors charged to high voltage. The rationale of the solid propellant ETC concept is that burning greater amounts of propellant by injecting plasma at key points in the process can lead to optimal ballistic acceleration. Enhancing the muzzle kinetic energy with an ETC design potentially translates into a velocity increase up to the low hypervelocity regime of 2-2.5 km/s (Kaplan et al. 1995).

The following summary of ideal gun performance is taken from White et al. (1997).

In a real gun situation, the maximum ideal performance of the gun is achieved when the propellant ignites and generates sufficient gas to immediately reach the maximum operating pressure. As the projectile moves down bore, the propellant mass generation rate is such that a constant pressure is maintained in the breech until the propellant is consumed. The projectile continues to move down bore to the muzzle exit, driven by an adiabatic isentropic expansion of the gases... Existing guns have been designed to perform in a nearly ideal fashion for a given mass of propellant- that is, the experimental velocities are within 90-95% of this ideal velocity. Thus, if significant performance improvement is to be realized, a substantial increase in energy input to the gun, combined with continued nearly ideal operation, must be obtained. Increasing the energy in the chamber can be achieved by (a) increasing the mass of propellant or loading density (which is the mass of propellant/chamber volume), (b) increasing the inherent chemical energy of the propellant, or (c) introducing electrical energy in the form of a plasma.

Using an Army Research Lab internal ballistics code modeling an M256 120-mm tank cannon White et al. (1997) show that increasing the loading density of the propellant requires an increase of the burn rate after maximum pressure is reached or else only a portion of the propellant will burn before the projectile exits the bore. The muzzle kinetic energy is reduced with increased loading density because less surface area is available to burn. Using the same internal ballistics code they conclude that if ET plasma ignition is assumed to be equivalent to sensible energy addition to the propellant, then a 50% increase in input energy (compared to the chemical energy in the initial propellant mass) is required to supply a 23% increase in muzzle energy. This translates into 20 MJ of electrical energy in an actual gun, which requires an impractical amount of capacitor storage space in a vehicle. Although increasing muzzle energy by using electrical energy input would be beneficial, increasing the propellant loading density must also be considered for energy enhancement to achieve increased performance. Conventional propellant burn rate, having the dependence $r = bP^n$ where r is the burn rate (usually cm/s), P is the pressure, and b and n are constants, must be modified by the plasma-

propellant interaction so that burning rate is increased after maximum bore pressure is reached.

Testing revealed other benefits of ETC guns including reduced ignition delay and jitter, and the ability to provide temperature compensation for the propellant. Taylor (2001) shows pressure curves taken from three different conventional ignition gun tests having ignition delays of approximately 250 ms, with up to 50 ms jitter. He also shows two pressure curves using plasma ignition, with both curves indistinguishable from each other, and the ignition delay less than 10 ms. The consistency provided by plasma ignition is clearly shown by the two ETC tests as compared with conventional tests of the same gun cartridge.

The dependence of the propellant burn rate on initial propellant temperature is illustrated in Oberle and White (1997). The propellant used in their example is JA2, a propellant used in an Abrams tank. The propellant burn rate for a sample initially at 65° C is 1.2-1.3 times that of a sample initially at -35° C. For conventional ignition, this results in different muzzle velocities for different starting temperatures. The same work shows the ability to match muzzle velocities for different initial propellant temperatures by tailoring the stored electrical energy of the igniting plasma, or simply the plasma energy. Both of these improvements result in increased gun accuracy.

PROJECT OVERVIEW

The objective of this work was to explore the mechanisms responsible for the observed benefits of ET gun ignition, as well as reveal more information on possible burn rate enhancement of the propellant. The propellant used in all the experiments was 2.5 mm thick sheet JA2. Originally, tests of an electrothermal plasma jet impinging on a propellant sample in open air were considered, with the intent to perform optical

diagnostics while the plasma ignited the propellant. Before the propellant was obtained, tests were conducted to characterize the plasma jet in open air. Copper planar laser-induced fluorescence (PLIF) was attempted as a flow marker during the plasma discharge. The plasma's high temperatures and pressures resulted in high background emissions at the copper line observed for fluorescence. A reliable method to subtract this background from the fluorescence images was not found. In addition, planar emission spectroscopy of two copper lines was attempted to estimate the plasma temperature throughout the flow field. However, the continuum emission at those wavelengths resulting from the interaction of free electrons was never reliably accounted for, and so the technique was set aside. The heat flux from the plasma jet to a surface it impinged upon was measured using a fast response heat flux gauge. The results of this experiment are described in this work.

After the propellant was obtained, it was discovered that the plasma jet did not ignite the propellant in open air. A pressure chamber was constructed to create the confinement necessary for the propellant to ignite. Optical access was designed into the pressure chamber to conduct the same optical diagnostics originally intended for the open air interaction. With the original design version of the chamber, the propellant did not ignite until about 50 ms, well after the plasma discharge. In addition, it was discovered that a condensed aerosol formed as the plasma cooled, probably from vaporized metal and carbon in the plasma. This aerosol made the chamber optically thick directly following the plasma discharge. Lasers were completely attenuated as they passed through the chamber. Many modifications were made to the design to find some time period during the discharge during which laser diagnostics might be conducted, but they were not successful. The pressure chamber design and the information obtained from experiments using it are described in Appendix B.

The studies of the interaction of JA2 propellant with plasma radiation alone were motivated by the importance of this interaction in the plasma ignition process. It was desired to conduct real-time measurements during the plasma propellant interaction. In these plasma radiation interaction experiments the propellant surface is separated from the plasma by a fused silica window and the plasma never touches the propellant. Broadband plasma radiation propagates through the window and causes decomposition reactions in the propellant, but the propellant does not ignite. Letting only the plasma radiation affect the propellant eliminated the problems with large background plasma luminosity and attenuation of laser interrogation beams and signal due to condensation. This enabled optical diagnostics which are the only practical means to obtain real-time measurements during the interaction. Further, the observed decrease in ignition delay and ignition delay jitter described earlier and for the desired increased burning rate in the propellant during a gun firing could be caused by the effects of plasma radiation on the propellant. Thus, the study of the plasma radiation interaction with solid propellant is very important to understanding and optimizing the benefits of the ETC gun.

Plasma radiation has been shown to cause blisters and subsurface voids throughout transparent JA2 samples 4 mm thick (Kappen and Beyer 2003), presumably due to gas generation from propellant decomposition. In the semi-transparent JA2 used for these experiments, with 0.05% graphite, blisters have been observed only at a depth less than 0.5 mm. In addition to the surface effects, significant gasification has been observed in plasma radiation-propellant interactions. Increased initial gasification during plasma ignition of propellant has been proposed as a cause for the decreased ignition delay and delay jitter (Beyer, Pesce-Rodriguez, 2004). Also, modeling shows that the increased surface area due to subsurface void formation increases propellant burning rate (Koleczko et al. 2001).

The experiments described here were designed to create time and spatially resolved observations of the plasma radiation-propellant interaction (PRPI) over the course of the plasma firing. Both radiative and conductive heat flux to a surface mimicking propellant were measured in an open air plasma jet. This gave some idea of the energy transport to the propellant surface in the PRPI studied later. In the PRPI experiments the plasma jet was confined to a chamber, separated from a disk of propellant by a fused silica window. Transport of decomposition products from the propellant surface was observed to give some information on the reactions taking place at the surface of the propellant as well as fluid flow at the propellant surface during a precursor step to radiative ignition. An intensified CCD camera was used to image nitric oxide (NO) by planar laser induced fluorescence and particulates by planar laser Mie scattering (PLMS). In addition, high speed video of the propellant surface was taken during the radiation-propellant interaction simultaneously with PLMS imaging away from the surface. This was designed to observe the propellant surface as it decomposed as well as correlate reaction products with what was observed on the propellant surface. In addition to this work, results from studies of plasma ignition of propellant in a pressure chamber, and temperature measurement at the propellant surface in an open air plasma jet are included in the appendices.

Chapter 2 covers a review of the literature on the interaction of electrothermal plasmas with propellants, as well as double base propellant ignition and burning. Chapter 3 describes the apparatus used for the experiments. Chapter 4 covers some of the experimental methods employed to collect and analyze the data. The results and conclusions are discussed in Chapters 5 and 6, respectively.

Chapter 2: Literature Review

ELECTROTHERMAL PLASMAS

In experiments over the last 15 years electrothermal plasmas have been used to ignite, control and augment the burn process of solid propellants for potential use in large caliber guns. These plasmas tend to be weakly nonideal (Bourham et al. 1997); electron densities, temperatures, and pressures are typically $10^{25} - 10^{27} m^{-3}$, 10,000-50,000 K (~1-5 eV), and 1-7 kbar (100-700 MPa), respectively (Edwards et al. 1995). Such plasmas are generated by large capacitors (hundreds of μF), either alone or many in parallel, charged to several kV and discharged over timescales from 100 μs to a few ms, resulting in total plasma energies from 1 kJ to 2 MJ. Usually, a fuse wire is placed inside a polyethylene or polycarbonate capillary connecting a plug anode to an annular cathode. At the onset of the discharge, the fuse wire explodes and begins to ablate the capillary wall. Continued energy input from the capacitor discharge further ablates and ionizes material from the wall, which sustains the plasma. The annular cathode also serves as a nozzle for plasma to vent. The remainder of the test setup depends on whether the test is of the plasma itself, a simplified plasma-propellant interaction, or a scale gun firing. Experimental studies typically involve a plasma jet issuing into open air or a large chamber, and measurements of temperature, electron density, composition, and heat flux. The plasma jet into open air takes the form of a dynamic, highly underexpanded, supersonic jet, the features of which can be seen in Fig. 2.1, along with a visible emission image (Kim et al. 2002). A precursor shock forms from the energy deposition inside the capillary at the beginning of the discharge and travels in front of the plasma jet. A contact surface forms where plasma meets room air. Brightest at the jet exit, the plasma expands into a barrel shock and recompresses at the Mach disk.

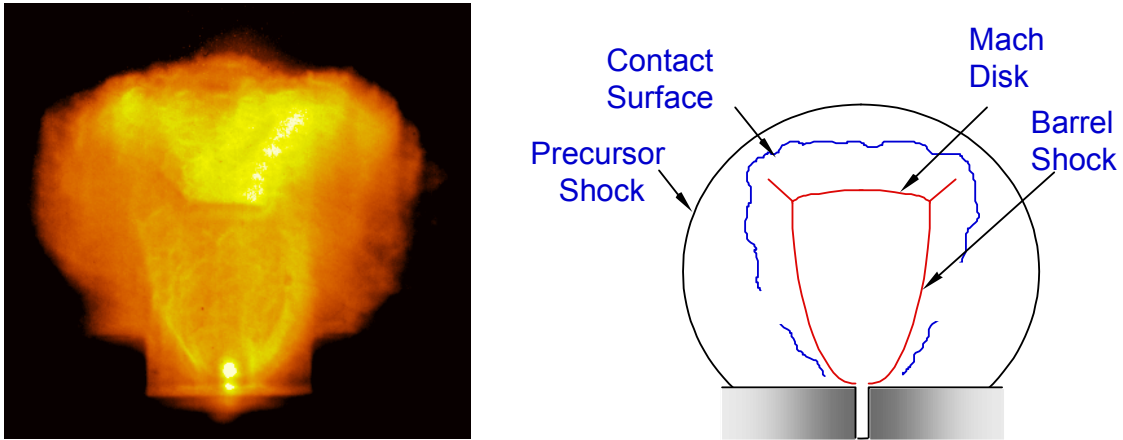


Figure 2.1: Principle features of quasi-steady plasma jet (Kim et al. 2002).

The process by which Kim et al.'s plasma forms is typical of most electrothermal plasmas. In their experiment a 251 μF capacitor charged to 5 kV is discharged over 500 μs through a polycarbonate capillary. Typical voltages and current traces from this setup can be seen in Fig. 2.2. The current is representative of an underdamped LRC circuit with only one oscillation. Each time the current nears zero, material stops ablating from the capillary wall. After the second current zero, there is not enough plasma to sustain the discharge. The capacitor discharge stops and charge remains on the capacitor. All other experiments reviewed that have described their discharge circuit keep current from oscillating either by designing an overdamped circuit or through use of diodes.

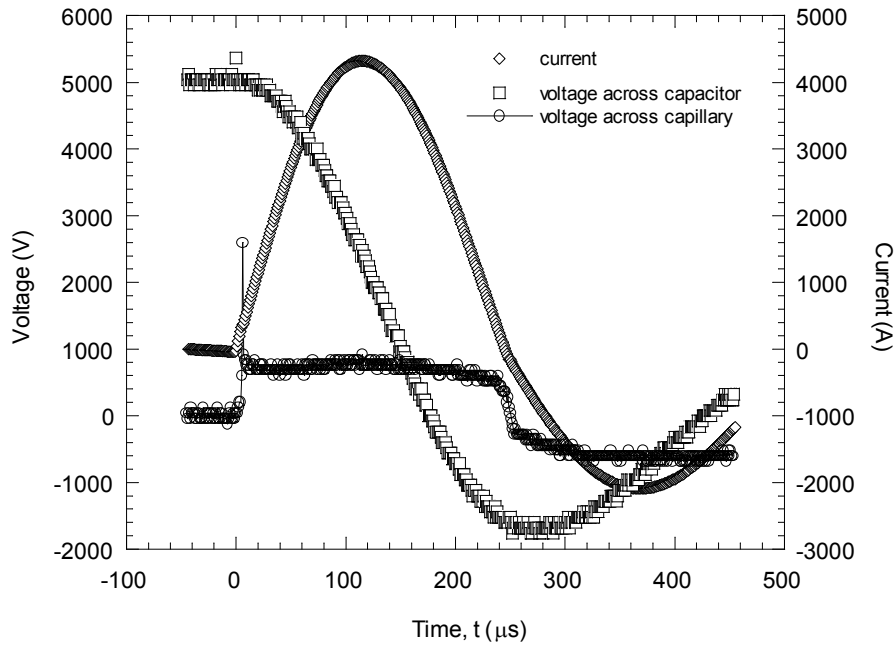


Figure 2.2: Typical voltage and current traces for 5 kV initial capacitor charge (Kim et al. 2002).

The maximum stored electrical energy for this plasma is 3.1 kJ, while other experiments have ranged from 100 J for open air electrothermal plasmas to 2 MJ for full scale gun tests. A representative visible emission imaging time history using this open air plasma jet production setup, taken from multiple runs, can be seen in the Fig. 2.3 (Kohel et al. 1999). An underexpanded jet is seen approximately 20 μs after the capacitor begins to discharge, at which point it continuously grows until the current maximizes around 120 μs . After this, the jet seems to weaken as the current declines, evidenced by the less obvious recompression shock. By the time the current reaches zero at about 250 μs there is no visible jet, only a bright plasma mass.

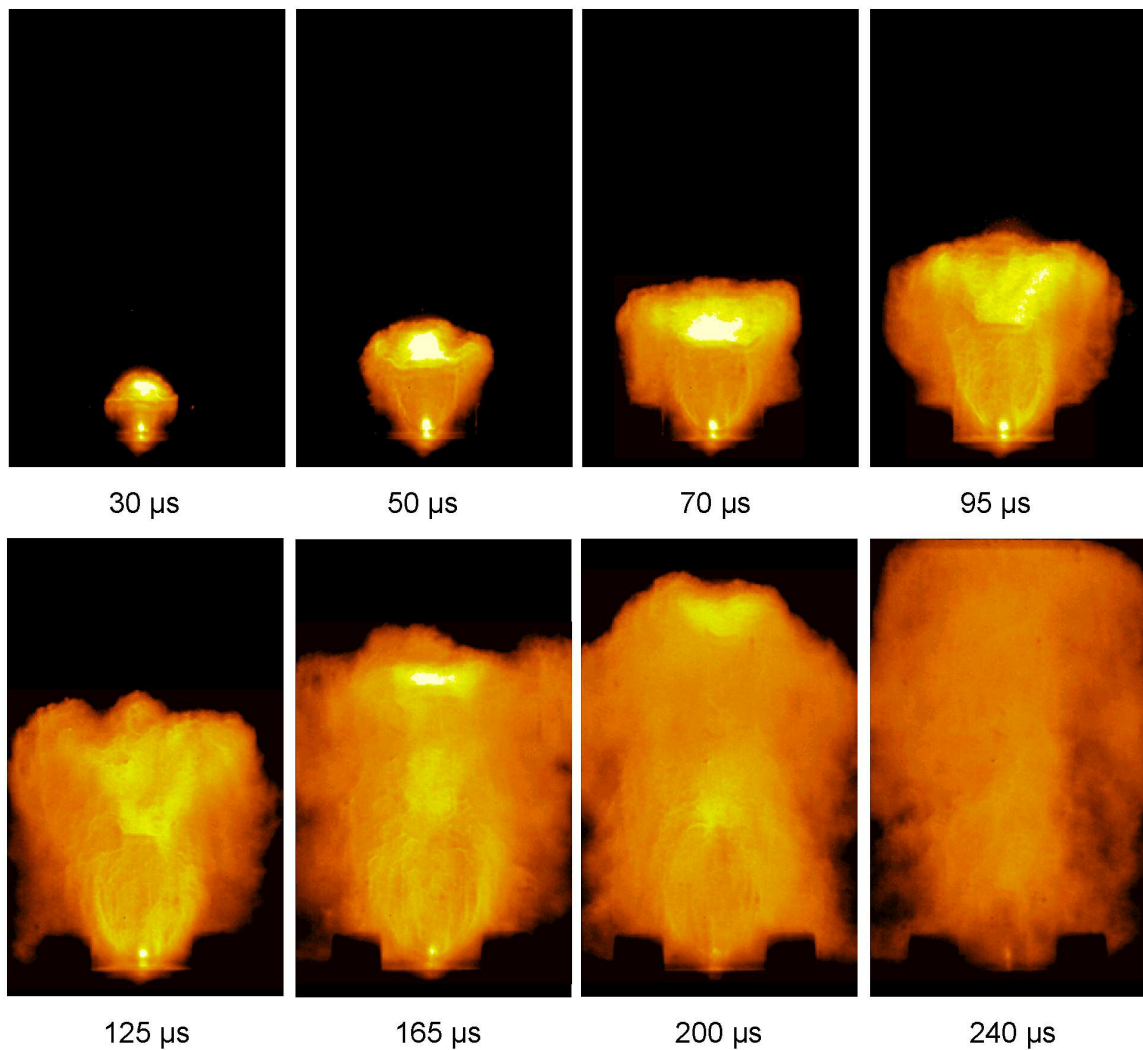


Figure 2.3: Visible emission time history of plasma jet (Kohel et al. 1999).

The majority of studies on electrothermal plasmas employ spectroscopic techniques to gather information. Non-intrusive techniques are well suited for this environment, because intrusive probes are damaged by the high temperatures, large velocities, and particle deposition that occurs during the plasma jet. Emission and absorption measurements integrate information along the entire line of sight through the plasma jet, while in a fluorescence measurement the pump source (usually a laser) must

propagate through the entire jet. The signal must also propagate through a portion of the plasma as well. Regions of these plasma jets can be optically thick, raising concern for the accuracy of optical techniques. Issues that arise from optically thick flows include self absorption for emission measurements, scattering for absorption measurements, and pump beam attenuation for fluorescence measurements.

The plasma inside the capillary (region of highest density) seems to be at least a graybody if not a blackbody radiator during most of the discharge. Emission spectroscopy of the jet exit or inside the capillary show that above a threshold plasma energy (different for each experimental setup) emission is broadband with less discernable line peaks and significant self-absorption (Ashkenazy et al. 1991, Hankins and Mann 1995, Kohel et al. 1999, Kukhlevsky et al. 2000, Kim et al. 2002). This is characteristic of an optically thick medium. Also, a large number of models of the steady state plasma inside a capillary assume a graybody radiator (Stephan Boltzmann's Law) for energy transfer to the walls (Loeb and Kaplan 1989, Gilligan and Mohanti 1990, Mohanti et al. 1991, Powell and Zielinski 1992, Hewkin and Figura 1993, Hurley et al. 1995). In addition, Kappen and Bauder (1999, 2001) use a model assuming local thermodynamic equilibrium and steady state with the plasma surroundings. While this does not necessarily result in blackbody emission, by Kirchoff's Law it does enable them to relate absorption and emission coefficients in the plasma like those of a blackbody.

Outside the capillary, optical depth is not well known. Because it is dependent on wavelength, density, and plasma composition, only a complicated numerical model can estimate radiation absorption in these plasmas. Tracing a ray through a plasma, optical depth is defined by:

$$\tau = \int_l^s \kappa'_o ds$$

where the integration is performed along ray \mathbf{S} from origin l to observation point s . The total effective absorption coefficient κ'_ω , a function of frequency, is defined as (Griem 1997):

$$\kappa'_\omega = \kappa'_l + \kappa'_c + \kappa_{Th} + \kappa_R.$$

The first two terms describe the net effect of line and continuum absorption, respectively, where the prime denotes accounting for induced emission processes. The last two terms account for scattering on free and bound electrons. Line absorption is the absorption resulting from an atom or molecule changing its internal quantum state, and is referred to as a bound-bound transition. In electrothermal plasmas bound-bound transitions are mostly electronic transitions in atoms. The coefficient κ'_l takes into account the line broadening caused by Doppler shifts associated with the absorbing atoms and molecules, and, more importantly, pressure broadening. The two types of pressure broadening result when electric fields caused by nearby ions or electrons perturb the absorber (Stark broadening), or neutral species perturb the absorber through long range van der Waals forces or dipole-dipole interactions. The continuum absorption coefficient accounts for photoionization (bound-free transitions) and inverse bremsstrahlung (free-free transitions), the result of inelastic collisions between free electrons and ions or atoms.

For the case $\tau \ll 1$, the radiation seen by the observer suffers negligible self-absorption in its passage through the medium. The observer sees essentially the contribution from each individual volume element along the ray, and the medium is said to be optically transparent to the radiation. When $\tau \gg 1$, the intensity is a direct measure of the ratio of emission to absorption. The medium is considered opaque to the radiation. If the medium is in thermal equilibrium, it is said to emit as a blackbody. When $\tau \sim 1$ the medium is said to be semitransparent (Bekefi 1966).

Modeling studies that would be able to estimate optical depth do not explicitly do so because they are only interested in radiation heat transfer. Kappen and Bauder (1999, 2001), Sakthivel et al. (1999, 2001), Peterson and Moses (1983), and Tsakiris et al.(1987) all use complex models accounting for bound-bound, bound-free, and free-free particle interactions to calculate absorption coefficients as a function of wavelength in a dense plasma. The results of their computations are expressed as frequency integrated Rosseland mean opacities, and are used to calculate radiative heat transfer by the method of Zel'dovich et al. (1966).

Only a few emission spectroscopic studies discuss optical thickness. For example, Kim et al. (2002) measured the attenuation of a dye laser beam tuned to an atomic copper ground state transition through a plasma jet into open air. Atomic copper is a trace species in most electrothermal plasmas arising from the fuse wire or ablation of copper-tungsten alloy electrodes. They found negligible absorption inside the barrel shock, a relatively low density area of the flow, but found that 40% of the incident energy was absorbed just downstream of the Mach disk. Through more calculations they show that only 15% of excited state transition emissions from the center of the Mach disk are absorbed as they propagate through the plasma. They conclude that the effects of self-absorption on emission temperature measurements are within experimental uncertainty limits.

The fact that a trace species in the plasma can attenuate an incoming laser beam by up to 40% when it is tuned to resonance shows that lines associated with a more populous species might be even more optically thick inside the Mach disk or a bow shock resulting from normal impingement on a surface. Laser beam attenuation has significant consequences in fluorescence experiments. When the fluorescence signal is of the same order as background plasma luminosity, a potential 40% attenuation of that signal

through the plasma increases the difficulty in separating fluorescence signal from background luminosity. In addition, fluorescence images would have to account for decreased signal along the path length of the pump beam.

A large majority of electrothermal plasma jet studies use emission spectroscopy to measure electron density and temperature. These studies will be discussed in detail below. The most common temperature measurement technique fits Lorentzian line shapes to copper emission lines in order to infer the line intensities. A Boltzmann plot of the relative intensities can then be used to infer temperature. In order to infer a temperature from the electromagnetic spectrum, local thermodynamic equilibrium (LTE) must be assumed. For the interpretation of spectra, we are mostly concerned with the accuracy of the Saha and Boltzmann relations for level populations in situations where not all constituents of the system are in thermodynamic equilibrium at a common temperature. In many plasmas, aside from the usual underpopulation of photons with respect to the blackbody, atom and ion velocity distributions are frequently not Maxwellian. This is a consequence of ineffective transfer of translational energy from electrons to heavier particles due to the small mass ratio. The basic assumption of LTE is that the free electrons have Maxwellian distributions. In addition, complete LTE for populations of all levels, including the ground state, necessitates that electron-collisional rates for a given transition exceed the corresponding radiative rate by about an order of magnitude (Griem 1997).

The electrons and ions/atoms are at different temperatures in a nonequilibrium plasma. Even in this case, van der Mullen et al. (1994) show that the relationship between populations of highly excited atomic levels and the ground state of the next ion are completely dependent on electron temperature and density. This situation is known as partial local thermodynamic equilibrium (PLTE). There have been many attempts to

define the range of levels where PLTE is valid. Griem (1997) provides a good review. Most models use simplifications to hydrogen or hydrogenlike ions to ensure that collisional cross sections and level distributions are more easily calculated. In plasma with large temporal and spatial variations in temperature and density, deviations in LTE also occur due to relaxation effects. Griem states that for the establishment of complete LTE during plasma production, excitation from the ground state to the upper level of the strongest resonance line tends to be the rate-limiting process.

Most of the literature simply assumes LTE for the purposes of fitting relative line intensities to a Boltzmann plot. While studying a laser produced carbon plasma with similar temperatures and electron densities to our open air plasma Harilal et al. (1997) posit that their plasma is in LTE because their electron densities are an order of magnitude larger than a necessary though not sufficient LTE criterion suggested by Bekefi. (1976) The Bekefi formula gives a necessary electron density greater than $7 \times 10^{15} \text{ cm}^{-3}$ with a plasma temperature of 10,000 K for the ground state of atomic copper to be in LTE. Using electron densities inside an electrothermal plasma measured from the H line and temperatures measured from atomic iron lines, Caillard et al.(2003) show that the two closely follow a relation derived assuming a singly ionized plasma in LTE. No studies of LTE in an electrothermal plasma were found aside from the references mentioned. From the evidence, it seems that if an electrothermal plasma jet is not in LTE, it is probably close. Even when LTE is not certain, a definition of temperature based on atomic transitions is useful because in an optically thin plasma a large amount of radiation heat transfer results from bound-bound transitions.

A large majority of the temperature measurements made by spectroscopic means used line of sight relative intensities of copper lines in polyethylene or polycarbonate plasmas, similar in their chemical makeup. The total electrical energies generally range

from 1-5 kJ in studies of the plasma jet outside the capillary. Some copper emission temperature measurements that are spatially and temporally resolved (Kohel et al. 1999, Kim et al. 2002, Sandolache et al. 2001) generally agree that the low temperatures are around $14,000 \pm 2000$ K and the high temperatures are around $22,000 \pm 2000$ K. In a few studies, (Hankins et al. 1993, 1995) optical fibers were placed at different positions inside a barrel down which the plasma propagated and along an open jet as it impinged on propellant (Hankins et al. 1997). They integrated emissions over the entire plasma firing and obtained temperatures that ranged from 9,000-14,000 K. Two time resolved spectroscopic studies at the nozzle exit (Caillard et al. 2003, Li and Li 2001) measured temperatures about 9,000-10,000 K. These seemingly low temperatures might be the result of self absorption because the jet exit can be optically thick, or they might be seeing light a small distance along the axis away from the jet exit where the plasma has expanded and cooled from the capillary conditions. In a few studies an optical fiber was placed in the capillary (Sueda et al. 1997, Bussiere et al. 2004). Temperature measurements could only be made early in the discharge because the plasma density increases as the discharge progresses, and self absorption affects the spectrum. These studies measured temperatures from 7,000-20,000 K.

While these temperature values have a large range due to the differences in data acquisition and plasma generation, one can get a general idea of the plasma temperature ranging from around 12,000 K after it has expanded out of the nozzle, to above 22,000 K where it has either gone through a recompression shock in open air, or a bow shock as it impinges on a surface. Another general trend seems to be the increase in temperature with plasma energy. Fig. 2.4 is from Kim et al. (2002), who have the most complete study of plasma temperature along a jet into open air. It best exemplifies the temperature along a plasma jet axis. Their measurements may be presumed more accurate because

they correct an error in the state degeneracy of one of the copper lines used in a few previous spectroscopic temperature measurements.

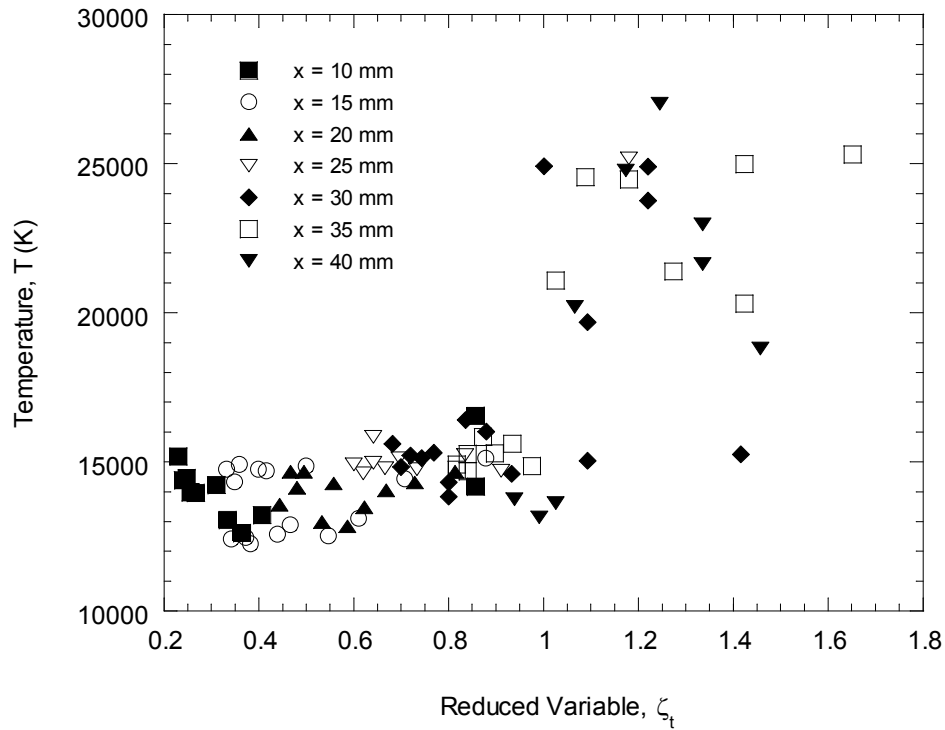


Figure 2.4: Variation of the plasma temperature along the axis of the jet for several different time delays; the downstream coordinate is the axial position scaled by the Mach disk location (Kim et al. 2002).

They scaled downstream distance by the position of the Mach disk so temperature measurements at different times during the discharge are plotted on the same graph. Temperatures range between 10,500 K and 14,500 K downstream of the jet exit

expansion and upstream of the Mach disk. At the Mach disk temperature jumps up above 20,000 K, although there is a large spread in values.

In addition to temperature measurements using copper lines, there have been a few other techniques used to estimate temperatures inside an ET plasma. Levin et al. (2003) used the intensity of an optically thick CIII line to estimate the blackbody temperature inside the capillary. Two groups (Hankins et al. 1993, Bussiere 2004) used conductivity measurements inside the capillary matched to an equilibrium composition model to estimate temperature. Neither method of measuring temperature inside the capillary could be compared to copper line emission measurements because self absorption makes emission measurements inside the capillary inaccurate or impossible. As expected, temperature values inside the capillary were generally higher than the maximum temperatures outside the capillary inferred from copper line emission. Hankins et al. (1995, 1997) used C₂ emission spectra matched to spectra predicted by a temperature dependent model. These agree reasonably well with copper line temperature measurements made by the same group. Caillard et al. (2003) used relative intensities of iron lines (one of their electrodes was steel) which resulted in temperatures between 5,000-12,000 K. They only made temperatures late in the discharge to avoid self-absorption, which might account for the relatively low temperatures. Taylor (2001) fits blackbody curves to measured emission spectra to estimate temperature. His measured temperatures are generally lower than 10,000 K. However, his spectra were acquired outside the capillary, where the assumption that the plasma is a blackbody may not be appropriate. For example, his published data show the blackbody line fits do not follow the measured spectra very closely (Taylor 2002, 2001).

A large number of plasma emission spectroscopic studies also measured electron number density from the Stark broadening of atomic transitions. Stark broadening is a

form of pressure broadening caused by the electric fields from ions and electrons near the emitting or absorbing particle. It is the dominant cause of line broadening in electrothermal plasmas. The majority of studies used broadening of the H line which is not very sensitive to plasma temperature or composition (Gigosos 1996), and is usually more discernable from the background spectrum than the H line. Additionally, Stark broadening density measurements do not require an assumption of LTE.

The range of electron densities seen in the literature is 10^{17} - 10^{19} cm^{-3} . It is difficult to compare a lot of the work because some measurements are not time resolved, and there is a wide range of spatial resolutions and plasma energies. Both Ashkenazy et al. (1991) and Hankins and Mann (1995) made a series of measurements outside the jet exit integrated over the entire firing. With plasma energies ranging from 50 J to 5 kJ, they clearly show that time-averaged electron density increases with energy. Kim et al. (2002) took both time and spatially resolved electron density measurements of a plasma jet in open air. They show that outside of the jet exit expansion and upstream of the Mach disk number densities range from 1.7×10^{17} – 5.5×10^{17} cm^{-3} and downstream of the Mach disk they range from 10^{18} – 2.5×10^{18} cm^{-3} .

SOLID PROPELLANT COMBUSTION

Most recent experiments involving plasma propellant interaction have used either JA2 propellant, or M30 propellant, and so these will be emphasized in the following discussion. Most burning and ignition work (including plasma ignition) uses propellant in stick form, as opposed to sheet form. Burn rate, usually measured in cm/s, is easy to deduce when one end of a cylinder is burning in the axial direction. Propellant is packed into gun cartridges as bundles of sticks, so when trying to create an experiment most like a real gun, stick propellant is used. Sheet propellant is usually used in smaller scale tests where plasma energies are low.

In general, solid propellants consist of several chemical ingredients such as oxidizer, fuel, binder, plasticizer, stabilizer, curing agent, crosslinking agent, bonding agent, burning rate catalyst, antiaging agent, opacifier, flame suppressant, and combustion instability suppressant (Kubota 1984). Both JA2 and M30 are double base propellants with nitrocellulose fiber (NC) as a binder and nitroglycerin as a plasticizer. JA2 has diethylene glycol dinitrate (DEGDN) as an added plasticizer, while M30 has nitroguanidine (NQ) as a high energy additive. Nitrocellulose is nitrated cellulose, a long chain molecule with nitrate esters as side chains, while the other three ingredients are nitrate esters of smaller backbone molecules. Nitration provides an oxidizer inside the material, which significantly increases the burn rate. JA2 is a homogenous propellant, with oxidizer and fuel linked chemically in its structure. M30 is considered to be a composite, because NQ crystals do not bind with the other materials in the propellant. The ingredients not specified in JA2 and M30 make up a relatively small percentage of the composition.

The various reaction zones observed with steady state burning of double base propellants are described by Fifer (1984) and Lengelle et al. (2000) The following description is a combination of their statements. The reaction begins in the subsurface preheat zone, approximately 100 μm thick at 1 atm and decreasing to approximately 20 μm at 20 atm. At the regressing surface (“foam zone”), the temperature becomes high enough for molecular degradation and gasification to take place, initiated by the rupture of the C-O-//NO₂ bond. Simultaneous recombination occurs, so that a mixture of NO₂, aldehydes such as formaldehyde (HCHO) and glyoxal (CHOCHO) are evolved. NO also emerges from the surface causing the net energy balance of the degradation to be exothermic. It is probable that some of the NO₂ reacts within the solid phase and that significant amounts of CO, CO₂, H₂O, etc., are also produced there. The surface

temperature is typically about 300°C and increases slowly with increasing pressure. At pressures under about 100 atm, a clearly separated primary flame (fizz zone) and secondary flame (luminous flame) are observed. In the fizz zone, the NO₂ is partially reduced to NO by reactions with the aldehydes to produce significant amounts of final-product-type molecules (CO, CO₂, H₂O, H₂). The fizz zone is ~200 μm thick at 1 atm, and ~100 μm at 20 atm. At the downstream edge of the fizz zone the temperature is roughly 800-1700°C, depending on propellant energy and pressure. An induction zone (dark zone), either thermal or kinetic in nature, extends beyond the fizz zone. Within the dark zone the temperature, and presumably the concentrations of the major species, remain almost constant. The standoff of the secondary flame defines the dark zone length, which is about 1 cm at 15 atm. When the secondary flame is fully developed the less reactive NO is reduced to N₂, even at pressures for which it does not yet influence the burning, with some leftover formaldehyde perhaps playing a role in initiating the reaction. The products are highly underoxidized (high CO, H₂), and if burning takes place in air, considerably more energy is released in the flame reaction. Final temperatures reached are around 2100-3100 K, depending on the heat of reaction. Under 100 atm the secondary flame is too far away to have any effect on the surface or even to induce a temperature gradient into the primary flame. The burning rate is then entirely under the influence of the primary flame. As the pressure increases beyond 100 atm, the secondary flame enhances the primary flame (through heat transfer) and then merges into it.

For the purposes of potential optical diagnostic applications during a plasma-propellant interaction, it would be useful to know the species present when double base propellant decomposes. As noted before, many condensed-phase reactions occur between the initial dissociation reaction and the appearance of gaseous species in the decomposition of double base solid propellant. Thus, even when thin films (5 μm) of NC

are decomposed slowly in a vacuum, the observed gaseous products consist mostly of final-product type molecules: CO, CO₂, and H₂O plus smaller amounts of H₂ and N₂. In addition, large amounts of nitric oxide are usually observed, along with lesser amounts of N₂O, HCN, HCHO, (CHO)₂, plus trace amounts of various hydrocarbon and CHO species. There appears to be little question that NO₂ is produced in large amounts during decomposition of NC, but the amount observed is very sensitive to experimental conditions. Decomposition in a stream of cold inert gas seems to be more effective than vacuum techniques in preventing secondary reactions (Fifer 1984).

Double-base propellants contain, in addition to NC, nitroglycerin plasticizer and various stabilizers. NG seems to vaporize from NC before decomposition in most thermal decomposition experiments, and there is no information available concerning what effect, if any, NG might have on the kinetics or mechanism of nitrocellulose decomposition. Information on thermal decomposition of specific propellants, like JA2 or M30, was not found.

SOLID PROPELLANT IGNITION

Ignition of solid propellants is the process occurring between the initial application of some energetic stimulus to a piece of propellant and the full-scale combustion of the propellant. Ignition of the propellant is thus a transient process with a definite point of initiation but an endpoint that depends on its definition. The total ignition process of propellants involves a transition from a nonreactive to reactive state via some thermochemical “runaway,” followed by a nearly equally rapid transition to full-scale combustion (Hermance 1984). In the works cited throughout this chapter, propellant ignition by a plasma only occurs when the interaction is confined. Most ignition studies are conducted in a closed chamber with no optical access, so ignition is usually defined by when the pressure begins to rise after the initial pressure peak created

by the plasma firing. The pressure history depends on the chamber geometry, plasma energy, and amount of propellant, and sometimes there is no pressure drop between the initial pressure rise due to plasma propagation out of the capillary and the pressure rise associated with propellant combustion. In addition, it is possible that self-sustained burning is occurring while the pressure drops after the initial peak because the plasma cools so quickly.

A lot of work on propellant ignition has focused on using radiant energy as the stimulus for ignition. The basic reason is the ability to select the heat flux applied to the propellant independently of all other environmental parameters: namely pressure, initial temperature, and chemical composition of the gas phase surrounding the propellant surface. While the absence of a hot gas adjacent to the igniting propellant surface separates this ignition technique from most real world applications, the introduction of interior as well as surface heating of translucent propellants from a radiant source can be similar to hot plasma radiation effects on a propellant. In his summary of radiation ignition experiments Hermance (1984) states that composite and double-base propellants can be ignited by radiant energy fluxes over a wide range of flux levels, pressures, and environmental atmospheric composition. Environmental gaseous composition has a small effect on the magnitude of the ignition delay for both double base and composite propellants. The results indicate a coupling exists between solid-phase exothermic decomposition in a very narrow region of the solid adjacent to the surface and the development of the final-stage gas-phase reaction. The size of the first-stage, solid-phase reaction zone is governed by the transmissivity of the solid phase and therefore the presence and importance of this stage may be magnified by ignition with radiant energy sources.

There have been a number of experiments involving radiative ignition of solid propellants. The majority of them use a much lower energy flux than produced by an electrothermal plasma. However, some trends observed are applicable to plasma ignition. Ohlemiller and Summerfield (1968) noted two main differences between radiative ignition and conventional hot gas ignition: some portion of the radiation is reflected from the propellant surface, and the radiation is absorbed in depth. Potentially disruptive factors that follow from in-depth absorption of the radiation include photochemically induced reactions that alter the dissociation mechanism of the binder and “bubbling” of the partially degraded binder at the propellant surface.

Deluca et al.(1976: pt. 1 and 2) conducted a series of experiments igniting double-base propellants with radiation from an arc image furnace and a CO₂ laser. Both light sources have continuously variable intensity. The spectral characteristics of the arc image were broadband with a peak near 550 nm while the CO₂ laser was a narrowband laser at a wavelength of 10.6 μm. In testing a propellant subjected to a fixed radiative flux they obtained a range of results depending on when the energy source was removed; they called this the ignition corridor. At short times, the rise in surface temperature was insufficient to induce a reaction. If the flux was continued the surface temperature reached a level at which reactions leading to propellant gasification began abruptly. With additional irradiation the gas evolved began to undergo further exothermic reaction. Eventually, irradiation lead to a point at which removal of the radiant input did not stop the reaction. This was termed the self-sustained ignition point. With some propellants the flame extinguished if the radiation flux was removed after a steady burning condition was reached. The flame could not survive the disturbance induced by the abrupt termination of the radiation. As the radiation energy increased, all the times discussed decreased. Deluca et al. also explored the effect of varying the amount of carbon a double base

propellant contained. They surmised that adding carbon decreased the times of the ignition corridor while making the propellant more responsive to changes in incident flux.

Radiation from an ET plasma alone has not been observed to ignite double base propellants. However, it does have significant effects on the propellant surface structure and chemistry. The one attempt to ignite a propellant by only conductive and convective heat transfer from an electrothermal plasma involved an open air plasma jet onto a propellant covered in aluminum foil (Katulka et al. 1999). At a plasma energy of 34 kJ (higher than most open air jet experiments), JA2 ignited when covered with aluminum foil (convective/conductive heating), and did not ignite when covered with mylar (radiative heating). This seems to indicate that while radiation might have a significant influence on propellant ignition during the plasma-propellant interaction and propellant burning afterwards, conduction and convection from the plasma is the dominant ignition mechanism.

PLASMA PROPELLANT INTERACTION

The plasma-propellant interaction (PPI) during gun firing is much more complicated than most laboratory ignition studies, or even conventional gun ignition, because it involves much higher temperatures, a significant contribution to heat flux by conductive, convective, and radiative heat transport, larger temperature and density gradients, and large populations of free radicals. Because of the difficult measurement environment most studies have measured global system properties such as muzzle kinetic energy or pressure rise during the interaction. Alternatively, the propellant surface and analysis of the gases evolved from the propellant have been studied after the PPI trying to infer information about processes occurring during the interaction. There have been a few studies of heat flux to the propellant and time integrated copper line temperature

measurements during the interaction, but there is very little detailed information of temperature, density, and species concentrations, all relevant quantities for chemistry and fluid dynamics.

Experiments involving plasma propellant interactions have used a number of different geometries. The plasma has: 1) ignited propellants in scale tests representing real gun geometries; 2) impinged normally and parallel to flat propellant surfaces at different distances downstream from a nozzle; 3) been created inside or traveled through a cylinder made of propellant; and 4) radiated through a clear plastic capillary onto propellant. The plasma is always produced with either a polyethylene or polycarbonate capillary. While there is evidence that plasma made from materials with different chemical compositions can reach significantly different temperatures and pressures (Fifer et al. 2003), polyethylene and polycarbonate are similar enough that, while having different equilibrium compositions at plasma temperatures, the temperatures and pressures reached in their plasmas are close enough to ignore which plasma composition is used. Without high plasma energies (~30 kJ), the interaction must be confined in a pressure vessel in order for JA2 or M30 to ignite. Ignition, like burning rate, is dependent on pressure. It is probable that the pressure dependence arises from the higher heat flux to the propellant surface in a denser fluid. A further explanation for the need for confinement is that heat transfer takes place over longer time in this situation, enabling the propellant to achieve a self-sustaining deflagration.

Early tests with ETC scale guns showed improvement in muzzle kinetic energies over conventional ignition. While plasma injection into the bore was considered to increase pressure at the projectile base, only tests with breech plasma injection were conducted for simplicity. The electrical pulse was tailored such that electrical power increased after maximum breech pressure was reached. This was an attempt to emulate

idealized constant pressure time histories as described by White et al. (1997). In a 60 mm gun system, Kaplan et al. (1993) showed that despite a 10% decrease in propellant loading (probably due to maximum pressure concerns) muzzle energy was increased 3.5% with a 735 kJ ignition pulse and a 600 kJ pulse at maximum pressure. In later tests with a 105 mm gun, Kaplan et al. (1993) showed a repeatable 5-6% increase in muzzle energy with plasma energies between 1600 and 1900 kJ. Data published by White et al. (1995) show a 20% increase in muzzle velocity inside a 30 mm scale model of a 120 mm gun with a 40 kJ plasma input. However, the conventional ignition was probably not optimized in this situation. Kaplan et al. (1993) also noted that the initial rate of pressure rise in the breech would increase with the increase of plasma energy. While they categorize it as an increase in burning rate, later studies seem to show that increased pressurization during the plasma firing is only from an increase in gas generation rate from the propellant, and not a result of self-sustained burning of the propellant. This will be discussed later.

In addition to showing proof of concept of increased muzzle velocities, these scale gun tests, along with the paper by Grieg et al. (1993) noted the reduced ignition delay times and reduced delay jitter over conventional ignition, the highly repeatable pressure and velocity data produced, and the potential for temperature compensation of the propellant. In their discussion of solutions to the problem of propellant temperature dependence Oberle and White (1997) show data that clearly indicate the ability to use ETC concepts to eliminate the propelling charge temperature sensitivity. The data were taken by United Defense, Limited Partnership on a series of firings using 120-mm tactical rounds in the M256 cannon (JA2 propellant). They showed that by increasing the igniting plasma energy up to 700 kJ they could match the muzzle velocity created by conventional ignition with a propellant temperature of 45° C with propellant temperatures of 0° and 21°

C. IBHVG2 (Anderson and Fickie 1987) is an Army Research Lab (ARL) interior ballistics model that models plasma ignition as a thermal energy source only and predicts quantities such as pressure traces and muzzle velocity. Using IBHVG2 Oberle and White predicted that in order to match the muzzle velocity of a conventional firing with propellant at 45° C, a 1.13 MJ plasma would be needed for propellant at 21° C, and 2.45 MJ would be needed for 0° C. In the tests, only ~600 and ~700 kJ were needed to match muzzle velocities.

This indicated that other interactions between the plasma and propellant were occurring, which resulted in the increase in the mass generation rate. They stated that possible mechanisms are burn rate augmentation, erosive burning, or radiative heating of the propellant by the plasma (resulting in higher propellant temperature and hence higher burn rate as in Oberle and White (1997)). The mass of the plasma is ignored in IBHVG2 because normally it is negligible compared to the mass of the propellant. It is now known that the plasma causes a significant initial pressure rise while it interacts with the propellant before the propellant deflagration is self sustained (Beyer and Pesce-Rodriguez 2004). This does not occur in conventional ignition, and would cause gun chamber pressure to reach maximum much more quickly. In addition to this, there is evidence that the plasma does radiatively heat translucent and transparent propellants, as well as increase the burn rate of the propellant (Kappen and Beyer 2003), although the literature is not clear on the latter.

A large number of studies has been conducted with the primary goal of discovering whether or not an electrothermal plasma increases propellant burn rates. Burn rates are measured a few different ways. The most common way is to calculate burn rate in cm/s with BRLCB (Oberle and Kooker 1993), a computer program designed at ARL that takes the input of propellant type and dimensions, chamber volume, and pressure

history, then calculates the burn rate inside the chamber. It also accounts for plasma solely as a thermal energy source. Considering the previously mentioned initial pressure rise due to the plasma propellant interaction without self sustained burning, it is not clear whether BRLCB is an accurate measure of burn rate, since a required input is the correct surface area of the propellant at all times, and hence the correct burn rate history from the beginning of the firing.

All the studies using BRLCB that tested burn rate of double base propellants after ignition by an ET plasma jet concluded that there is no burning rate enhancement after the plasma firing (Oberle and Wren. 1995, Birk et al. 2000, Kaste et al. 2001, and Lieb et al. 2001). Oberle and Wren (1995) tested M43 propellant in a 30 mm scale gun with a 41 kJ plasma, and tested M5 in a closed chamber with a 15 kJ plasma. Birk et al. (2000), Kaste et al. (2001), and Lieb et al. (2001) used the same facility, injecting between 15-30 kJ into bundles of M30 and JA2 sticks, similar to a gun geometry but in a closed chamber. The chamber had a rupture disk into vacuum so that at specified pressures, the reaction would be quenched. This was done in order to study the surface effects on the propellant from the interaction. By matching pressure curves of similar runs (same electrical input, propellant mass etc.) that were quenched at different pressures, they could compare actual differences in propellant dimensions with that predicted by pressure traces input into BRLCB after the plasma discharge. They determined that the burn rate inferred from BRLCB for M30 after the plasma was erroneous while the JA2 burn rate was accurate, and that JA2 showed no increase in burn rate (Birk et al. 2000). They verified the burn rate inferred from BRLCB for JA2 by showing that the vivacity curve behaves as expected, having a positive slope. Vivacity is the instantaneous time derivative of the experimental pressure, divided by that pressure $\frac{1}{P} \frac{dP}{dt}$. It is a measure of the burning surface area.

Lieb et al. (2001) also concluded that there was a significant burn rate enhancement (40% - 120%) over conventional ignition during the plasma pulse. They show an initial pressure rise from the plasma much greater than that from conventional ignition. Their plasma discharge was variable, but lasted about 1.5 ms. The rapid pressure increase during the plasma is followed by a transition to conventional burning. The problem with interpreting a burning rate from these data is that significant outgassing can occur during the PPI without ignition, and so it is not clear when exactly ignition is occurring. Also, they do not compare measured and predicted propellant diameters for burn rates during the plasma interaction, so the accuracy of the BRLCB burn rate during the plasma discharge is not tested.

Bourham's group has done some work injecting plasma onto JA2 sheet propellant inside a vacuum chamber (Edwards et al. 1995, Bourham et al. 1997). The reaction is quenched by the vacuum as soon as the plasma discharge terminates. The plasma energies range from 1-5 kJ, much smaller than work done at ARL. They get a single burn rate per run by measuring the mass lost by the propellant during the firing and calculating the rate in cm/s knowing the propellant surface area and discharge time. They plot these burn rates with respect to average pressure at the surface of the propellant during the discharge, varying plasma energy and angle of the sheet with respect to the jet axis. They too conclude that burn rate is increased during the plasma discharge over conventional ignition, between 20% and 40% when the sheet is parallel to the jet, and up to three times higher for normal impingement. Once again, it is not clear if the propellant is actually burning or gases being produced cause the mass loss.

Woodley and Fuller (1996) report on tests conducted by jetting plasma with an energy of 30 kJ onto a number of different propellants inside a closed chamber. They used BRLCB to determine propellant burn rates. They also saw increased pressurization

over conventional ignition during the plasma discharge, which they term “enhanced gas generation rate.” The one double base propellant they tested did not show an increased burning rate beyond the plasma discharge. However, a few of the propellants that contained nitramines (RDX, HMX) .did show enhanced burning rates after the plasma.

Li et al. (2004) also conducted experiments injecting a 2.4 kJ plasma into different propellants in a chamber. They measured chamber pressure during ignition of normal JA2, along with the opaque composite propellants XM39 and M43. With the two opaque propellants they noticed an initial pressure peak during the plasma discharge followed by a second peak tens of milliseconds after the plasma. They used the term “two-stage burning behavior” to describe the pressure traces. They also noticed a much less distinct two-stage behavior with the JA2 where there is only a decrease in the rate of pressure rise as the plasma finishes discharging followed by a global maximum in pressure 700 μ s after the plasma jet. They attributed this difference to JA2 being easier to ignite than composite propellants. They noted that with all three propellants the gas generation rate was very fast during the plasma pulse and much lower after the plasma pulse. Also, they observed gas generation rates were largely independent of the propellant type during the plasma pulse. In subsequent tests varying the energy of the plasma (Li et al. 2005) while igniting JA2 they found that lowering the plasma energy to 1.56 kJ and below produces a clearer two peak pressure trace.

Two studies involved the plasma propellant interaction after the propellant was already ignited. Del Guercio et al. (1996) injected 10-30 kJ plasmas into burning JA2 7-perf propellant inside a closed chamber at 2 and 10 ms delays. The 7-perf propellant grain was in stick form, with 7 cylindrical holes in an array down the length of the stick. They measured the burn rate using BRLCB. The burn rate is probably accurate because propellant is definitely burning during the interaction, and the mass of fluid in the

chamber when the plasma is injected is much larger than the plasma mass (pressure is not affected very much by the plasma itself). The results were not consistent between runs. They attribute the differences to effects of injecting plasma at different delays. For a couple runs with a 30 kJ plasma they observed an increase in burn rate of 17% and 8%. With an 11 kJ plasma, they saw an increase of 2.5% in one run, and a decrease as high as 16.5% in another. From these results it appears that higher plasma energies could increase the burn rate of JA2 propellant.

Proud and Bourne (1997) conducted plasma propellant interaction tests with very low plasma energy (70 J) inside a very small chamber (4 cm³). They ignited a cylinder of nitroglycerin based propellant (probably double base) with a heated wire inside the bore and then created plasma by exploding wires inside or outside of the propellant cylinder at specified pressures. They measured burning rate as a function of chamber pressure, and compared runs with plasma to those without. They showed that when plasma is created away from the burning interface, similar to a plasma jet interaction, burning rate returns to normal after the plasma is gone. However, when a wire is exploded inside a cylinder of propellant, it increases the burn rate by approximately 60% for the rest of the burn. It is not clear exactly how an exploded wire plasma would differ from an ablated capillary plasma in this situation. From evidence that increased burn rate is caused by in depth changes in the propellant, it seems that a wire exploding near the surface of propellant either produces more radiation flux or the shock wave associated with it is stronger than a wire exploding away from the surface, and the resulting plasma propagating onto it.

In a similar experiment to Proud and Bourne, Koleczko et al. (2001) exploded wires near the surface of 3 mm JA2 sheet formed into a cylinder around the wire. They used two different kinds of JA2, the normal kind with graphite, and a transparent kind without graphite. In a closed bomb they ignited both kinds of propellant with a 2 kJ

discharge. The burn time of plasma treated propellant is lower than that of conventionally ignited propellant, and the burn time of transparent JA2 is lower than that of what they call black JA2. The JA2 is black because of graphite added to the propellant. It has been said that black German JA2 is darker than the normal translucent JA2 found in the USA, which would cause less in depth radiation effects in the German JA2. They measured pressure during runs with 1, 2, and 6 kJ discharges into transparent JA2 propellant, and showed that burning rate increased with increasing plasma energy, although the difference between 1 and 2 kJ is much more pronounced than the difference between 2 and 6 kJ. They then pretreated the propellants with 0.8 or 1.5 kJ plasmas using the same experiment geometry in open air. Interestingly, the black JA2 ignited and burned under these conditions, but the transparent JA2 did not. The transparent JA2 showed effects of fragmentation in the interior which were lens shaped crazes with a diameter of 2 mm or less. They burned this pretreated transparent JA2 in a chamber with optical access, where they directly measured the burn rate. They found that the burning rate was higher than that of non-treated JA2. They concluded that this increased burning rate is caused by radiation effects inside the propellant, increasing the surface area by creating voids inside the propellant. Radiation penetrates completely into the transparent propellant, hence the larger increase in burn rate over normal JA2, and the dependence of burn rate on plasma energy. In addition, the black JA2 ignited in open air when transparent JA2 did not. Presumably this is due to the increased heat flux to the propellant surface caused by improved radiation absorption, resulting in a higher temperature.

In light of evidence of possible burn rate enhancement of gun propellants by plasma ignition, there have been a number of studies of the surface of propellant (chemical and physical structure) after plasma interaction in order to elucidate possible burn rate enhancement mechanisms. Generally, these fall into two categories, one where

propellant is ignited by plasma in a closed chamber then quenched by rapid depressurization, and the other where sheet propellant is exposed to plasma through polyethylene to isolate radiative effects on the propellant.

Lieb and Gillich (1994) made a micrograph study of JA2 propellant extinguished in a 30 mm scale gun setup. Because the propellant burned for a time after ignition, they found very little difference between the conventional ignition and plasma ignition cases. For the plasma case, they did find evidence of erosive burning, due to the higher speeds and temperatures of the plasma, and evidence of combustion occurring beneath the surface. Kaste et al. (1999, 2001) made surface studies of extinguished JA2 and M30 ignited by plasma in a closed bomb. They used a number of techniques (high pressure liquid chromatography, Fourier transform infrared spectroscopy, photoacoustic spectroscopy, micro-reflectance spectroscopy, x-ray fluorescence spectroscopy, desorption – gas chromatography – mass spectroscopy, scanning electron microscopy) to determine the difference between plasma ignited and conventionally ignited propellant. Neither study showed much difference between the two cases. They observed color differences between the primer ignited and plasma ignited JA2, which might indicate different decomposition mechanisms in the two cases. They also noticed metals on the surface of the propellants for the ETC case from the plasma production equipment. The problem with these studies is the propellants burned for some time before being extinguished, so any surface effects from the plasma propellant interaction probably burned off before flame extinction.

Pesce-Rodriguez et al. (2001) measured plasticizer and NO levels in M30 and JA2 exposed to a plasma jet with gas chromatography – mass spectroscopy. They also observed exposed propellant surfaces through a scanning electron microscope (SEM). The SEM images show different responses for each propellant. The M30 surface is

characterized by pits, gouges, chasms, and cracks, while the JA2 is characterized by blisters and subsurface voids. They do note that for both propellants, surface area is increased, which would increase the burning rate. For M30, NO was increased to a depth of about 0.5 mm when the propellant was exposed to plasma, while it remained about the same for conventional ignition. NO was increased for JA2 sheet to a depth of about 0.75 mm when exposed to plasma. They also show that JA2 grains exposed to plasma have reduced NO at the surface, also to about 0.75 mm. NO is one of the first decomposition products of nitrates in double base propellants, and so is a good marker of where the propellant has been affected by plasma.

While continuing this work Beyer and Pesce-Rodriguez (2000) included pressure data when igniting propellant in a closed chamber. They used lower plasma energies than those used for results discussed by Kaste et al. (2001). The propellant is not ignited until after the plasma discharge finished, and the pressure dips before rising again from the burning. They note that even though JA2 shows such significant surface erosion and surface area generation, it does not match the M30 in pressure generation during the plasma. Also, the JA2 transitions to ignition much more rapidly than M30. Interpreting these results they conclude M30 has a sufficiently strong optical absorption in a relatively thin surface layer that material is ablated without heat transfer to the remaining solid. Also, JA2 absorption deposits energy over a larger volume.

Li et al. (2005) conducted two unique measurements involving an unconfined plasma jet into JA2 propellant. They analyzed surface composition after the exposure using an energy dispersive spectrometer (EDS) in a scanning electron microscope (SEM) as well as measuring propellant decomposition products during the exposure with a triple quadrupole mass spectrometer (TQMS). With the SEM they found evidence of melting, blisters, pits, as well as deposition of metallic particles. After the firing tungsten and

copper were found on the surface using the EDS as well as a marked decrease in carbon. This raised the possibility that the major decomposition products were species containing carbon. Using the TQMS they observed increases in the amount of H₂O, CO₂, CO, H₂CO, and NO and observed the appearance of small amounts of HNO and NO₂. The presence of H₂O and CO₂ in the combustion products indicates complete combustion of some part of the propellant during the PPI. The other species are common double base propellant decomposition products. The authors were surprised to observe any NO₂ because usually it does not survive the decomposition process.

Because ET plasma radiation seems to have a significant effect on propellants, there have been a number of studies that isolated the radiation effects from the conductive and convective effects of the plasma. They generally have the same geometries. A plasma is produced inside, or propagates into a polyethylene or polycarbonate tube. JA2 sheet samples are placed outside these tubes. Both polyethylene and polycarbonate have small absorbance down to about 350 nm, so the ultraviolet plasma radiation, which does not reach the propellant, may be significant. White et al. (1997) noticed the translucent JA2 became opaque where the plasma radiation had affected the propellant, and voids were formed up to a depth of 1 mm into the propellant. Their results support the idea that in depth voids and subsurface blisters are caused by plasma radiation as opposed to conductive or convective effects.

Kaste et al. (1998) measured NG and DEGDN levels inside a propellant surface exposed to radiation from a 17 kJ plasma by desorption – gas chromatography – mass spectroscopy. They found that while the amount of NG was unchanged, DEGDN weight percent was reduced from 25% to between 15-20%. They also exposed JA2 covered by a Mylar sheet to a plasma expanding into open air. They found the JA2 did not react in the

open air case, and since Mylar transmits more radiation than polyethylene, concluded that radiation intensity is much higher in the confined configuration.

Kappen and Beyer (2003) did a number of experiments varying the energy and discharge time of an exploding wire plasma inside a polycarbonate tube, through which JA2 sheet was exposed to plasma radiation. They concluded that peak discharge power is a more significant parameter than total pulse energy although discharge time also slightly affects the level of interaction. Since plasma radiation seems to be causing these effects, total radiative energy might be a better measure, but most published data included peak electrical power, and not radiative power. They also state that the in-depth effects in the propellant mentioned by White et al. (1997) are caused by plasma radiation. Surface and cross section images of the JA2 after exposure to plasma radiation clearly show surface blisters and subsurface voids.

Beyer and Pesce-Rodriguez (2004) used the same setup as Kappen and Beyer to expose propellant to plasma radiation. However, they used both transparent and normal JA2 sheet along with M30, and placed the propellant inside sealed vials. They measured gaseous species produced from the interaction by Fourier transform infrared spectroscopy. Both kinds of JA2 produced the same species: CH_4 , CO_2 , and CO . The transparent samples seemed to produce more of each species, indicating the graphite in standard JA2 does not change the extent of reaction from the plasma radiation but merely serves to shield the inner portion of the sample from the light energy. No oxides of nitrogen were detected which was unexpected considering they are a primary decomposition product. CO_2 , N_2O , CO , and H_2O were detected with M30. The absorbance values were lower for M30 than for JA2, which is consistent with the observation that M30 response to the plasma radiation is a strong interaction limited to a thin layer at the surface.

To complete a summary of measurements made on the PPI, two studies of heat flux from an unconfined plasma jet have produced similar results despite very different measurement techniques. Williams and White (2001) measured temperature on the back of propellant disks with an infrared camera after normal impingement in open air of a 4.5 kJ plasma jet. The disks were situated 25 mm from the jet exit. Once the temperature reached a steady state, they could calculate the energy transferred to the propellant during the PPI, ignoring heat loss while the temperature equilibrated and possible evaporation during the PPI. From the energy transfer value, they calculated an average heat flux to the propellant. They measured a heat flux of 4100 W/cm^2 for a copper disk. For JA2 disks, the average heat flux measured in two different runs was 3800 and 4800 W/cm^2 , while they measured a heat flux of 1800 W/cm^2 for an M30 disk. They explained this lower flux for M30 by postulating lower radiation absorption. However, because previous experiments show that more mass gasifies from M30 during the PPI a large portion of this discrepancy can probably be accounted for by their neglect of gas evolution.

Das et al. (2005) used thin platinum films sputtered on a polyimide substrate blocked by fused silica windows to measure radiative heat flux from an electrothermal plasma jet. At a distance of 75 mm from the jet exit on the axis they measured peak heat fluxes of 400 W/cm^2 for a 0.6 kJ plasma and 800 W/cm^2 for a 0.86 kJ plasma. At a distance of 50 mm they measured a peak flux of 1400 W/cm^2 for a 0.6 kJ plasma. At this distance they also observed a reduction in peak flux by 20% as the gauge is moved 3 capillary diameters off axis.

To summarize, the results of a plasma propellant interaction seem to depend largely on the effect of plasma radiation on the propellant. This does not mean that radiation ignites the propellant because conductive and convective heat transfer seem to account for more of the energy transfer. However, the ignition and burning of propellant

can be modified depending on where radiant energy from the plasma is deposited in the propellant, and what effect that deposition has on the propellant. In the case of M30 radiation is absorbed in a thin layer at the surface, and a large portion of the heat transfer goes into vaporizing that material. Depending on the pressure at the surface and the plasma energy, the propellant might or might not ignite before the plasma discharge is finished. The radiation does not seem to affect M30 in depth, and so the burning rate after the plasma discharge is not affected.

For JA2, radiation penetrates into the propellant depending on the amount of graphite in the mixture. For transparent JA2 with no graphite, radiation penetrates in depth and causes voids inside the propellant where material has gasified. Once the propellant ignites these voids add area to the burning surface which potentially increases the burning rate of propellant. It has not been determined whether the altered chemistry in these voids due to gasification reactions also affects burning rate. Normal JA2 with graphite absorbs radiation in a thinner layer at the surface (depending on the amount of graphite). The same gasification reactions occur, but only in this thinner layer. There is not enough data to thoroughly compare plasma ignition of graphite-free JA2 with that of normal JA2. There is potentially greater initial pressurization with transparent JA2 because of the larger volume affected, and a higher temperature at the surface of normal JA2 because absorption of the same amount of energy occurs in a smaller propellant volume. Both surface temperature and pressure would affect ignition, so it is not clear which type ignites quicker. In a real gun situation, ignition timing might not be as important because ignition occurs before the plasma discharge finishes with normal JA2, but it might affect the amount of energy required to ignite the propellant.

PROPELLANT DECOMPOSITION

There is a large body of work involved with the specifics of propellant decomposition. Usually the impetus of this work is for stability of propellants in long term storage, and so the energy source used for decomposition is much lower than that needed for ignition. However, the basic decomposition reactions observed apply to the PPI (especially in cases absent ignition) because the decomposition is a similar process over a much shorter time scale.

Propellant decomposition by plasma begins with two different possible reactions: photolysis and thermolysis. Photolysis is the breaking of chemical bonds by the absorption of light and thermolysis is the breaking of chemical bonds by heat. In a decomposition reaction it is difficult to separate the two because the absorption of light is heat absorption if the photons are not of high enough energy to break the bonds. An electrothermal plasma is a broadband light source that emits strongly in the ultraviolet, and both photolysis and thermolysis inevitably occur. In addition to the basic chemical dissociation occurring in propellant decomposition, there are also larger scale effects due to gasification and inhomogeneities in the propellant. Because JA2 is a mixture of three nitrate ester bases along with a number of other species, the knowledge of its decomposition is by no means complete. Its decomposition involves many different chemical reactions beginning in the solid phase and ending in the gas phase. However dominant reactions, products, and trends have been observed in double base propellants and individual nitrate esters, and that will be discussed here.

Clark and Stephenson (1983) conducted x-ray photoelectron spectroscopy of propellants exposed to a 3 mW/cm^2 energy flux from a 500 W Hanovia UV lamp over a period of up to 120 minutes. The lamp produced a series of spectral lines with the most intense at 366, 546, 436, 405, and 303 nm. They noted that typical quantum yields of the

photolysis of simple nitrate esters are at least an order of magnitude larger than those in chain scission of cellulose or cellulose nitrate. They showed that nitrocellulose loses nitrogen much quicker than oxygen or carbon as a result of this photolysis.

Yang et al. (1996) irradiated NC samples with a laser over a range of wavelengths and detected the decomposition products with an ion trap mass spectrometer. The second, third and fourth harmonic of an Nd:YAG (532, 355, 266 nm) at 33 mW/cm² (3.3 Hz) irradiated the sample. No products were detected at 532 nm but with 355 and 266 nm light NO was a strong peak that increased with lower wavelength irradiation. Even at the lower wavelengths no carbon containing species were observed. Using a tunable dye laser the wavelength dependence of denitration in the 310-330 nm range was measured and was found to be linear with increasing denitration for decreasing wavelength.

Oyumi and Brill (1986) flash pyrolyzed a number of nitrate ester propellants by rapidly heating a nichrome filament attached to a sample of propellant. They measured decomposed species through FTIR a few mm from the propellant surface. They observed the decomposition products were a result of competitive degradation processes and found three classes of nitrate ester defined by the relative concentrations of the products:

- 1) dominance of side-chain products
- 2) mixture of side-chain and backbone products
- 3) dominance of backbone products

They noted that decomposition of the nitrate ester group to NO₂ probably dominates in all cases but the products are strongly influenced by the secondary reactions taking place. They conclude two factors contribute to the category in which the nitrate ester belongs. There is a tendency for compounds with lower percent carbon and higher percent nitrogen and oxygen to fall under class 1, while the opposite case falls under class 3. Also, the condensed phase chemistry contributes increasingly from class 1 to 3. They

observed a strong pressure effect on propellant decomposition products as well. At low pressures (below 10 psi) NO_2 and CH_2O dominate for class 1 propellants while NO_2 decreases from class 1 to class 3. At low and mid pressures (10 – 100 psi) CO and NO dominate the products from class 2 and 3 and above 100 psi CO, CO_2 , and H_2O dominate the products while no nitrogen containing products are detected. Oyumi and Brill posit that reactions in the heterogeneous phase are more important for class 2 than class 1. By composition both NC and DEGDN fall under class 2 while NG falls under class 3. Therefore at room pressure CO and NO would be expected as easily observable decomposition products.

Roos and Brill (2002) conducted a high pressure (5 atm) thermal decomposition experiment with a number of energetic materials. This study, with the same setup as the previous one by Oyumi and Brill, varied the temperature of the heater as opposed to the pressure, and used a slightly different set of propellants. They found that NO, and CO concentrations for NG dissociation decrease with increasing temperature while CO_2 increases. However, changing the pressure has a much more pronounced effect. They noted that when more oxygen is present in the nitrate ester, more of the carbon and hydrogen is converted to CO_2 and H_2O . Also, the amount of NO, CO_2 , and H_2O increases while CO decreases as the oxygen balance in the propellant increases. They detected very small amounts of NO_2 and CH_2O that correlate with the amount of those species in the propellant chain, and noted that these two species are more prevalent in nitramine decomposition. They surmised that in nitrate ester propellant decomposition the reactions that produce NO and CO are dominant.

Kimura (1989) studied the chemiluminescence of NC during thermal decomposition. He found a large difference between decomposition in pure nitrogen and air and concluded oxidative reactions occur in the condensed phase during thermal

decomposition. He proposed the following kinetic scheme to produce the observed chemiluminescence:

- 1) Nitrate esters initially decompose by rupture of one of the RO-NO₂ bonds to form NO₂ and alkoxy radicals (RO·).
- 2) The generated NO₂ oxidizes the RO· to form peroxy radicals (ROO·) and NO
- 3) A termination reaction occurs by the recombination of the peroxy radicals.
- 4) Decomposition of hydroperoxides (ROOH) is a possible step since they can be formed through reactions of peroxy radicals and nitrate esters.

Here R represents alkyl groups.

The breaking of the RO-NO₂ bond to produce RO and NO₂ seems to be the dominant first step in both photolysis and thermolysis of nitrate ester propellants. NO, a result of NO₂ reacting with the parent alkoxy radical, was the only species detected during a photolytic decomposition experiment. It is one of the most prevalent species observed in thermal decomposition. With thermal decomposition the propellant decomposes to a much greater degree, and species like CO, CO₂, and H₂O appear at higher concentration, depending on the ambient pressure and temperature. Only small amounts of NO₂ and CH₂O are likely to appear, as they seem to react in the solid phase before escaping the propellant. The experiments conducted for this work are meant to provide information on the major mechanism of decomposition in an electrothermal plasma/JA2 solid propellant interaction.

MODELING OF THE PLASMA, PROPELLANT, AND PLASMA PROPELLANT INTERACTION

Numerous physical processes must be simulated in a plasma propellant ignition model. Comprehensive models of an electrothermal plasma jet or combustion of a double base propellant are themselves extremely complicated and incomplete. Therefore, the interaction of the plasma with the propellant, and the ignition of the propellant is even more difficult to model. The working fluids of the plasma and propellant combustion gases are compressible, viscous and have a large range of temperatures.

The plasma jet is usually supersonic, with a large amount of heat transfer through radiation and convection to the confining surfaces, mostly the solid propellant. Because of the high temperature in an electrothermal plasma, a large number of species and reactions must be accounted for. The high temperatures cause most species to emit large amounts of radiation. The plasma is not a blackbody, and so the emissions must be simulated as a function of wavelength. As a result the absorption in the surfaces surrounding the plasma must be accounted for as a function of wavelength.

The combustion of a double base propellant involves reactions in both the solid and gas phase, with the possible presence of a liquid phase as well. All real world double base propellants include at least two and often three or more main energetic ingredients, and also include a number of stabilizers and catalysts in small amounts that affect the combustion. The main energetic ingredients are large nitrate esters of organic molecules. Individually, the combustion of these species and conversion from the solid or liquid phase to gas is not well understood. A very complicated system results when these ingredients are combined with small quantities of catalysts and stabilizers to form a mixture that is homogenous on the macro scale but heterogeneous on the micro scale. There is a marked lack of knowledge of reactions taking place in the solid phase during

propellant combustion because experimental techniques to study the solid phase during decomposition and combustion are rudimentary at best. As a result of the severe complications in a full physical description of the plasma propellant interaction, all simulations include assumptions and simplifications to make the problem tractable.

The most current models of propellant combustion that attempt to predict burn rate completely model the gas phase, and make some assumptions for the solid phase and the transition between solid to gas. They all assume a one dimensional flame. There is very little modeling of nitrate ester propellants compared to nitramines and AP. However, many models (Prasad, Yetter and Smooke, 1997, Davidson and Beckstead, 1997) take similar approaches to that of Miller and Anderson (2004, 2000) who concentrate on nitrate ester propellants. Miller and Anderson (2004) attempted to model multi-ingredient nitrate ester propellants. They tried to determine total starting-material enthalpy by accounting for the enthalpy of solution and mixing. They treated two domains – the condensed phase and the gas phase, and neglected in-depth reactions and diffusion. They assumed a distribution of gas phase species evolved from the condensed phase independent of pressure, and solved the energy equation for this distribution. They also used a semi-empirical pyrolysis law to calculate the relationship between the mass flux and the surface temperature. They then used a complicated version of the PREMIX code (59 chemical species and 365 reversible reactions) which uses detailed kinetics to solve gas phase equations for multiple reactions. This enabled the calculation of flame profiles and steady burning rates in their simulation. Their calculated burning rates were within a factor of two of measured burning rates.

Eisenreich et al. (2002) took a semi-empirical approach by deriving governing energy equations for burning propellant and solving for constants using experimental burning rates. Their goal was to extend the empirical Vieille's law ($r = bP^n$) to situations

where the propellant was being heated rapidly (ETC gun and laser ignition) and the propellant was porous or foamed. They assumed a one dimensional flame as well, but did not account for detailed kinetics in the gas phase. This work was not intended for prediction, but to explain the possible physical mechanisms encountered in transient energy deposition during ignition for different propellant geometries.

Modeling of the plasma jet usually includes geometry considerations beyond a 1-D flame. Wilson et al. (1999) modeled an axisymmetric plasma jet with no body forces or chemical reactions. They conducted two analyses, a point blast wave approximation for the flow outside the barrel shock and Mach disk, and an inviscid, adiabatic flow inside the barrel shock. The isentropic model did not predict the shock structure, and so they matched the two approaches with a semi-empirical approach. They predicted the position of the Mach disk of a jet into air well, but the calculated temperature distribution inside the jet did not match experimental data.

Zaghloul et al. (2001) created a model to predict the formation of the plasma inside the capillary. They modeled the circuit as an RLC circuit with the plasma being the load. They used experimentally measured Ohmic heating as the term to drive their simulation. They included corrections to the Gibbs free energy to account for non-ideal effects in the plasma. The model was one dimensional (axial) and time dependent. The heating was assumed to be uniform in the cross section. The plasma was assumed to be in LTE and so they could calculate the detailed plasma composition by a set of Saha equations. They then used conservation equations for a fluid to calculate the flow field as it changed over time.

Nusca et al. (2001) created a more complete model for a plasma jet in an ETC igniter. They simulated the high-temperature, non-ideal, chemically reacting gas flow field within the capillary and jet using CFD. The NSRG2 code they used solved the 2D or

axisymmetric, unsteady, real-gas Navier-Stokes equations including chemical reactions, species diffusion, variable specific heats, viscosity, and thermal conductivity. They solved for 57 reactions and 39 species. In contrast to a combustion kinetics code the species considered were mostly atoms and ions created by the high temperatures in the plasma. They neglected electrical currents as well as radiation transport in their model. Their model successfully calculated the precursor shock, barrel shock, and the Mach disk in the plasma jet. They compared calculated pressure with pressure measured in a chamber of the same geometry and conclude that the timing of the pressure peaks were well predicted but the pressure levels were too low.

There have been a few attempts to simulate the plasma inside a gun chamber, with or without propellant, using varying degrees of complexity to predict phenomena occurring inside an ETC gun. The internal ballistics codes used are empirical in nature, and do not simulate burning rates from first principles. Katulka et al. (1997) attempted a linkage of three established models, IBHVG2 for interior ballistic calculations, a pulse-power code to determine energy input into the plasma, and a plasma cartridge code to determine plasma characteristics. The plasma is only an energy input into the ballistics code. The current they calculated matched well with experiment, but they did not make any predictions for burning rate or pressure inside the gun.

Wren et al. (1999) created a thermodynamic model of radiation distribution in the combustion chamber of an ETC plasma. They used a one dimensional model of the plasma with conservation of mass and energy, assuming a blackbody radiator to calculate radiation transfer to the walls and propellant inside a gun. They also assumed uniform absorption by transparent JA2. They calculated a possible burn rate increase of 3% to 8% by grain heating alone. They concluded that ignition is dominated by convection while grain temperature is driven by radiative heating.

Woodley and Billett (2001) calculated pressure time histories during an ETC gun firing using an internal ballistics code. They empirically modified the burn rate law to account for the rise in pressure due to enhanced gas generation. They showed that accounting for the plasma as an energy source as well as a pressure source predicted pressure curves inside ETC guns better than older ballistics codes for both one and two dimensional geometries.

Sun et al. (2005) attempted to couple a 1-D unsteady flow model of the plasma with an internal ballistics code for the propellant. They calculated a muzzle velocity increase of 47%, which is much higher than anything else observed in the literature.

No ETC gun simulations found in the literature were near the complexity of individual plasma and propellant burning models. Even the individual models neglected key aspects of the plasma propellant interaction. The lack of surface structure accounting in predictive propellant modeling neglects most phenomena discovered in this work. In addition, the most complex plasma model in terms of chemistry and flowfield neglected radiation transport. However, there are relatively comprehensive plasma radiation models cited here. This field is still new and complex enough that all the physical processes and reactions involved are not known. Thus, it is difficult to compare simulations with results from experiments on the interaction of plasma radiation with propellant.

Chapter 3: Experimental Setup

PLASMA PRODUCTION APPARATUS

The plasma produced in these experiments is almost exactly the same as that of Kohel et al. (1999) and Kim et al. (2002). The capillary housing has been redesigned for ease of use. In the setup used for the current work, a 251 μF capacitor charged between 2 and 5 kV connects to the discharging circuit via an ignitron mercury vapor switch. The current switches on in a few microseconds and conducts from a fully charged capacitor to a 25 μH inductor along coaxial cables, lengthening the capacitor discharge and the plasma jet duration to about 500 μs . Traveling from the inductor and through a copper-tungsten alloy nipple inserted in the bottom of the polycarbonate capillary, the current explodes a 0.051 mm copper fuse wire running the length of the capillary bore. Electrical current exits through an annular electrode at the top of the capillary serving as a nozzle for the plasma jet and is conducted to the other half of the capacitor via the metal capillary enclosure and the same coaxial cables described above. After the fuse wire explodes, material from the inside wall of the capillary ablates and ionizes by deposition of energy from the discharge. The plasma escapes through the annular electrode and forms an underexpanded supersonic jet in open air. The open air plasma jet assembly can be seen in Fig. 3.1. The figure does not include the capacitor or the inductor. Current propagates through a steel rod inside the Lexan insulator and through the capillary bore, then out of the cap through a flat copper rod mounted on the side.

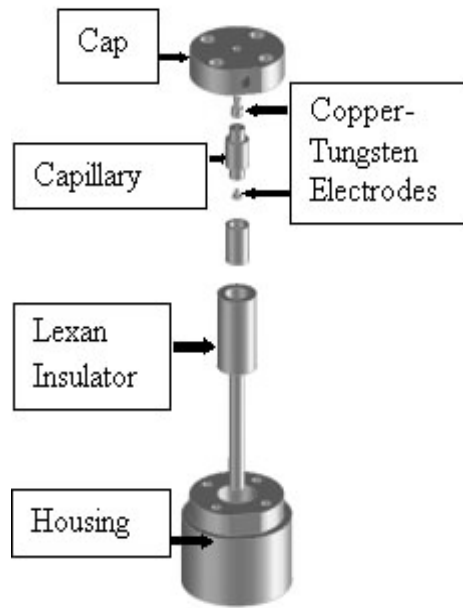


Figure 3.1: Plasma jet firing assembly.

HEAT FLUX MEASUREMENTS

Propellant ignition and decomposition depends on the heat flux to the surface. In these experiments the heat flux from a freely-expanding plasma jet was measured along its axis of symmetry. The measurements were made by using a Vatell heat flux microsensor. This gauge has a resistance temperature sensor for calibration purposes as well as a differential thermopile sensor for heat flux measurement. Output voltages from each sensor were recorded by a Tektronix TDS 520C digital oscilloscope. The gauge was calibrated at the factory and heat flux was calculated by a simple expression using the resistance measurement from the temperature sensor and the voltage measurement from the differential thermopile. The gauge was coated with colloidal graphite to increase

the absorptivity of radiation. Unfortunately this coating increased the response time of the gauge to 300 μ s. However, these measurements give a general indication of the heat flux experienced by a surface exposed to an electrothermal plasma. There have been very few studies of plasma heat flux in the literature so the data serve as confirmation that the order of magnitude of the heat flux measured is the same as previous studies as well as showing trends for the heat flux variation with position.

The sensor was mounted at the end of a rod, as shown in Fig. 3.2, and was positioned at several standoff distances (x_s) from the capillary bore exit. Purely radiative heat flux measurements were taken by placing a 3.2 mm thick fused silica flat in front of the sensor. In addition, total heat flux was measured at different points along the axis of the jet by removing the fused silica covering. Radiative heat flux measurements were repeatable enough that radiative heat flux could be subtracted from total heat flux to get a measure of the conductive and convective (cc) heat flux alone. The capacitor was charged to 5 kV in all firings. The timing of all experiments is discussed in Chapter 4.

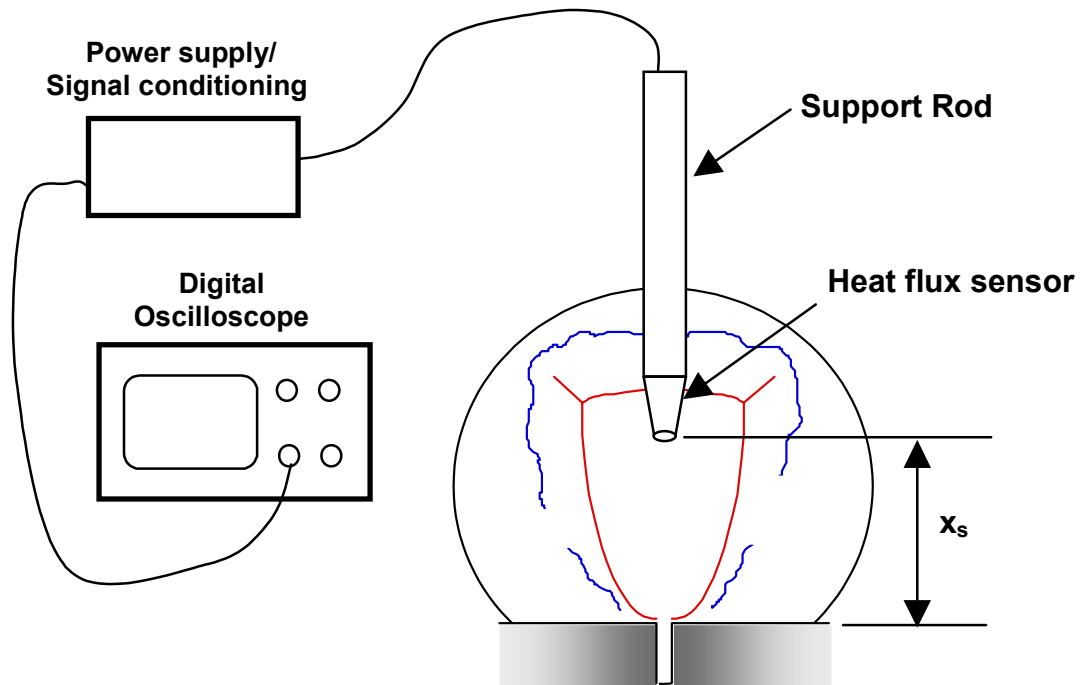


Figure 3.2: Experimental diagram for heat flux measurements.

PLASMA RADIATION CHAMBER

In all the experiments in this study the capacitor was charged fully to 5 kV. The plasma did not make direct contact with the propellant surface in these experiments; only radiation from the plasma reached the propellant surface. A chamber was bolted onto the plasma producing device to capture the plasma jet. This increased the residence time and density of the plasma in front of the propellant over that of an open air firing. Both of these effects would cause an increase of radiative energy transferred to the surface of the propellant. In order to minimize the metal deposition inside the chamber and capillary, the plasma exhausted during the firing through a 3 mm diameter vent in the side of the

chamber. The plasma was not completely confined, and the capacitor discharge lasted up to 100 μ s longer than in an open air discharge.

Figure 3.3 shows the setup of the capillary enclosure along with the plasma chamber for a typical laser diagnostics experiment for a plasma radiation-propellant interaction. A 1.27 cm diameter disk of JA2 propellant (0.05% graphite by weight) punched from a 2.54 mm thick sheet was fastened by a coating of Vaseline to the bottom of a steel rod above the chamber window before each firing. The side surface facing the camera was coated with a lamp black solution to minimize the luminosity from the propellant and to improve visibility of the signal just above the surface. The bottom surface of the propellant was 2.70 cm from the bottom edge of the plasma chamber window during the initial NO PLIF and particle scattering experiments. In the simultaneous high speed imaging experiment the propellant was moved to 3.14 cm offset from the plasma chamber to enable a view of the propellant surface.

The plasma was produced inside the capillary, propagated through the nozzle, and then expanded into the chamber (5.8 cm^3). The plasma was completely isolated from the propellant by a 1.27 cm thick fused silica window on the top of the chamber. This window was protected by a 1.59 mm thick disposable clear acrylic sheet for the initial imaging experiments. Both the acrylic sheet and a fused silica flat of the same thickness were used to protect the window during the two camera high speed imaging experiment. This enabled an observation of the effect of added ultraviolet radiation to the broadband visible radiation that decomposes the propellant when using the acrylic mask. A blackened aluminum foil screen was attached to the chamber wall to block the camera's view of the plasma exhaust so no background luminosity from the plasma was observed.

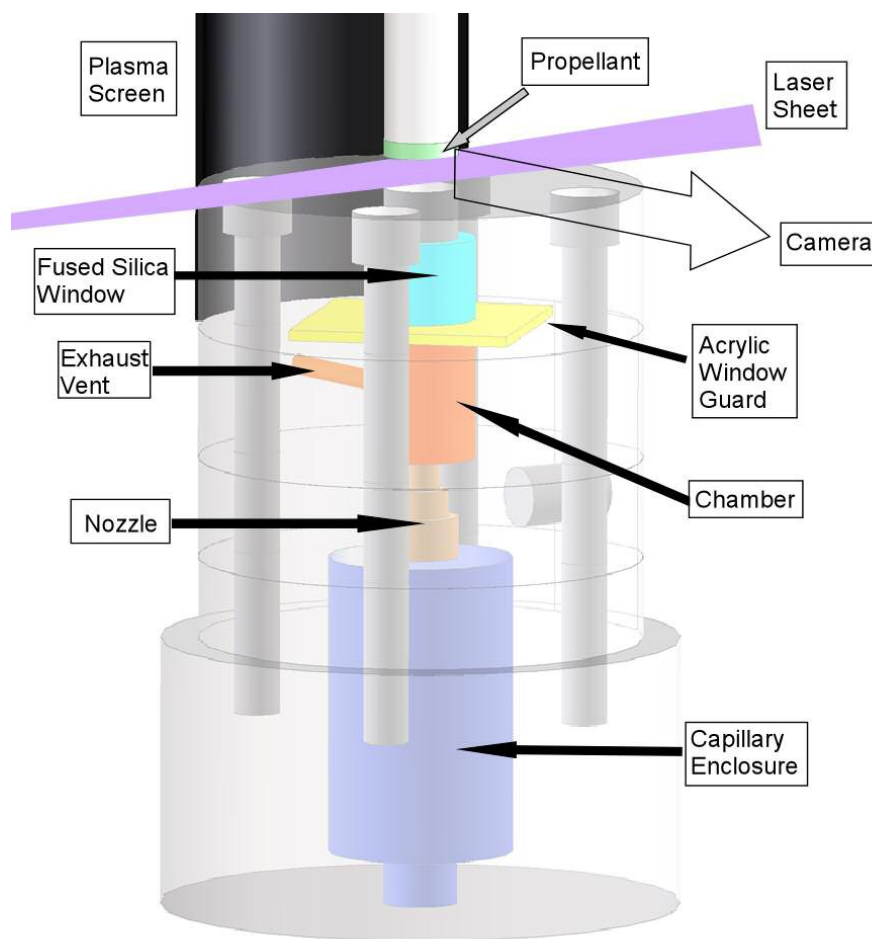


Figure 3.3: Capillary enclosure and discharge chamber with window for plasma radiation.

Two data sets were taken to characterize the plasma radiation through the chamber window. The radiation intensity time history during a firing was measured using a fast response photodiode put in place of the propellant with an ND 200 filter attenuating the light. Also, the emission spectrum was measured at two different times during the discharge with an acrylic window guard. A fused silica lens focused plasma light onto a 100 μm fiber optic, spectrally resolved by a Spex 1681 spectrograph with a 50 μm slit width and recorded on a Roper Scientific PI-Max intensified CCD camera. The camera was gated to 1 μs and only one spectrum was taken per firing because image acquisition

time was much greater than 600 μ s. However, the spectra were repeatable enough that multiple spectra taken over different spectral ranges at a given delay could be spliced together to form an emission curve.

SINGLE SHOT NO PLIF AND PLMS IMAGING

Figure 3.4 shows the laser setup for the NO PLIF experiment. Several steps were needed to create the 226 nm light needed to pump NO. A frequency doubled Nd:YAG (Spectra Physics GCR 150) laser pulsed at 10 Hz and operated at 532 nm was used to pump a Lumonics HyperDye-300 laser. The dye laser, with a 2×10^{-4} molar concentration of Pyromethene 597 dissolved in ethanol was tuned to output a 574 nm beam. The 574 nm beam was then frequency doubled with a KDP crystal inside an Inrad Autotracker II. The resulting 287 nm light is combined with the residual 1064 nm light from the Nd:YAG that has been time delayed to coincide with the dye beam by lengthening the laser path across the table. The combined beams were then mixed in a KDP crystal inside a second Inrad Autotracker II to create the 226 nm beam. This beam was separated from the residual 1064 nm and doubled dye beams with a fused silica Pellin Broca prism which also steered it to the plasma chamber. The ~ 1 mJ laser pulse was focused with a 1 m focal length fused silica lens and then expanded into a sheet using a 25.4 mm focal length cylindrical lens. The cylindrical lens was placed only 7-8 cm from the propellant because the field of view was only 5 mm tall. A photograph of the camera and plasma chamber geometry is shown in Fig. 3.5.

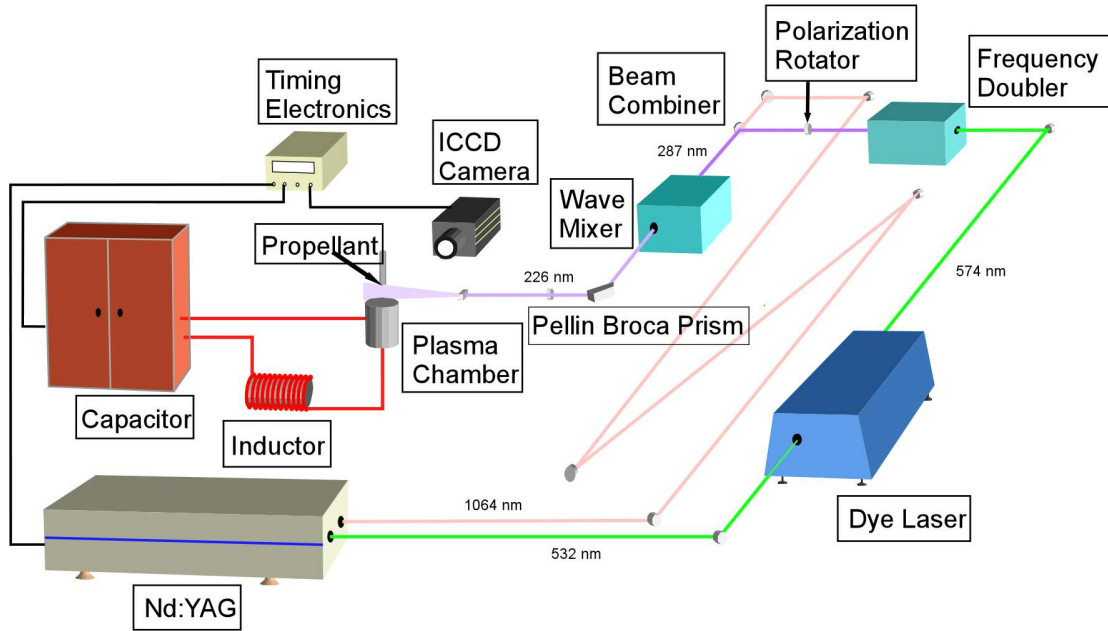


Figure 3.4: NO PLIF laser setup.

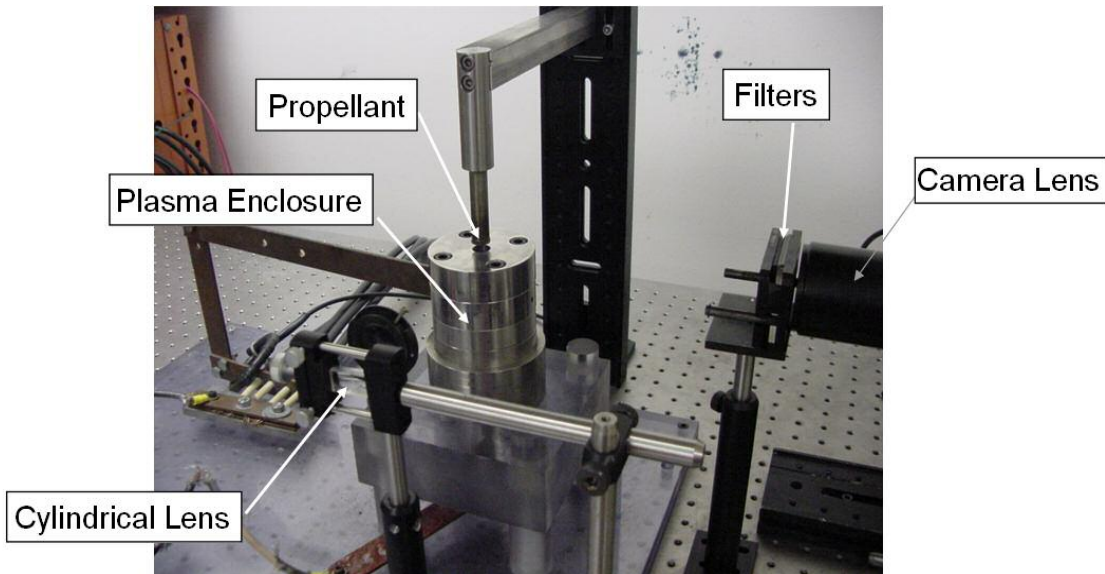


Figure 3.5: Photograph of the NO PLIF and Nd:YAG PLMS experimental setup.

The first excited electronic transition of NO, $A^2\Sigma^+(v'=0) \leftarrow X^2\Pi(v''=0)$ was employed for fluorescence imaging. General PLIF theory is discussed in Chapter 4. The dye laser wavelength was calibrated by an excitation scan. The laser was scanned across the rovibronic absorption lines of NO at a rate of 0.0004 nm/s and the broadband fluorescence signal was collected through a UG5 filter onto a Hamamatsu PMT. A Stanford Research Systems 250 Boxcar Averager/Gated Integrator was used to collect the fluorescence signal synchronous with the laser pulses. The fluorescence signal was averaged over 30 pulses and the averaged signal was collected by a Tektronix TDS 520C digital oscilloscope as the laser was scanned. This measured absorption spectrum was compared to a calculated spectrum (Seitzman 1985-1990). The $Q_{21}+R_{11}(9.5)$ transition pair at 225.9802 nm was chosen as the pump for PLIF because it produced a relatively large signal. There was no estimate of the temperature of the NO exiting from the propellant. However, the heat flux gauge temperature only increased tens of degrees during plasma impingement. Therefore it was thought that the absorption line that produced high signals at room temperature was thought to be adequate for pumping during the plasma radiation-propellant interaction.

Fluorescence imaging was conducted using a Roper Scientific PI-Max 512 intensified CCD camera. A UG-5 UV filter was placed in front of the Nikkor Nikon UV lens to attenuate laser light scattered onto the CCD. The field of view geometry is shown in Fig. 3.5. The diameter of the propellant disk at the top of the image was 12.7 mm wide. The propellant was located 5 mm from the top surface of the plasma chamber, which was cropped from the bottom of the image. During the firings the propellant surface was never exactly flat and changed over time during the interaction as material was lost from the surface. Because the laser pulse period and camera readout time was much longer than the plasma discharge time of 600 μ s, only one image was taken per firing. A series

of NO fluorescence images were taken from 100 μs delay from the plasma trigger (when NO first began to appear) to 600 μs (when the capacitor finished discharging) at 50 μs time intervals. Usually two to three images were taken at each time delay. Although NO was present after 600 μs , we were not interested in the conditions after the plasma discharge.

While conducting the fluorescence experiments, a small amount of scattering off large particles was seen throughout the flow. This warranted further study and a scattering experiment using the frequency doubled Nd:YAG was conducted. The same intensified CCD camera was used, this time looking through OG 515 and BG 38 filters to attenuate luminosity from the propellant surface. The ~ 20 mJ/pulse laser was apertured to 5 mm high and formed into a sheet by a 225 mm convex cylindrical lens. This was different than the NO experiment because the laser power was much higher and the original beam was much larger as well.

SIMULTANEOUS HIGH SPEED PROPELLANT IMAGING AND PLMS

Figure 3.6 is a photograph of the experimental setup for the two camera simultaneous high speed video of the propellant surface and laser scattering by ejected particulates. This experiment employed the same plasma radiation chamber as in the single shot NO PLIF and PLMS experiments. The propellant was raised to 3.14 cm above the plasma chamber to enable viewing of the propellant surface. A Coherent Evolution 90 Nd:YLF laser pulsed at 10 kHz was used as the light source. The laser was run at full power during the scattering experiment (nominally 90 W, 9 mJ per pulse). The beam from the laser seen in the bottom left of the image was steered towards the propellant by two 45° mirrors. The beam was apertured on the top by a beam stop before being formed into a sheet by a 250 mm focal length cylindrical lens. The aperture was to keep the laser from igniting the propellant.

Two Photron Fastcam Ultima APX cameras were used to conduct high speed imaging. The propellant surface camera was run at a frame rate of 50 kHz while the laser scattering camera was run at 10 kHz. Their timing is described in further detail in the Chapter 4. At these high speeds, the detector size was 256×64 and 256×128 pixels, respectively. There were problems with the capacitor discharge interfering with the readout for the 10 kHz camera, and so the detector size was reduced from the maximum the camera could handle at that frame rate.

A close-up photograph of the camera setup is shown in Fig. 3.7. The scattering camera was in the same position as the ICCD camera in the previous experiments. It viewed laser scattering through a bandpass filter that attenuated scattering of the broadband plasma emissions. The surface camera was mounted at an angle looking down towards the top surface of the plasma chamber. A broadband visible mirror was placed on top of the plasma chamber so that the camera viewed the bottom surface of the propellant disk. Because the camera was at an angle, the lens was mounted on a Scheimpflug mount, and had lens extension tubes to enable a smaller field of view. The Scheimpflug mount tilts the lens with respect to the detector plane so that the plane of focus is at an angle with respect to the detector plane. The lens was set to $f/16$ so the entire propellant surface was in focus, and a neutral density (OD 2) and a colored glass filter (OG 550) were used with this camera. The attenuation provided by the neutral density filter enabled viewing of the propellant surface during the plasma firing (the surface was illuminated only by the plasma), and the OG 570 further attenuated the UV light scattered by the propellant when the fused silica mask was in use. Five images of laser scattering were recorded during the plasma discharge, with 100 successive images recorded for the run. About 40 successive images of the propellant surface were visible using the specified propellant surface camera setup. The shutter time for both cameras was set to $4 \mu\text{s}$. The cameras were run

slightly out of sync to avoid laser scattering appearing in the propellant surface images. The cameras were registered by the method described in Chapter 4 in order to correlate events on the surface with particles appearing below the propellant.

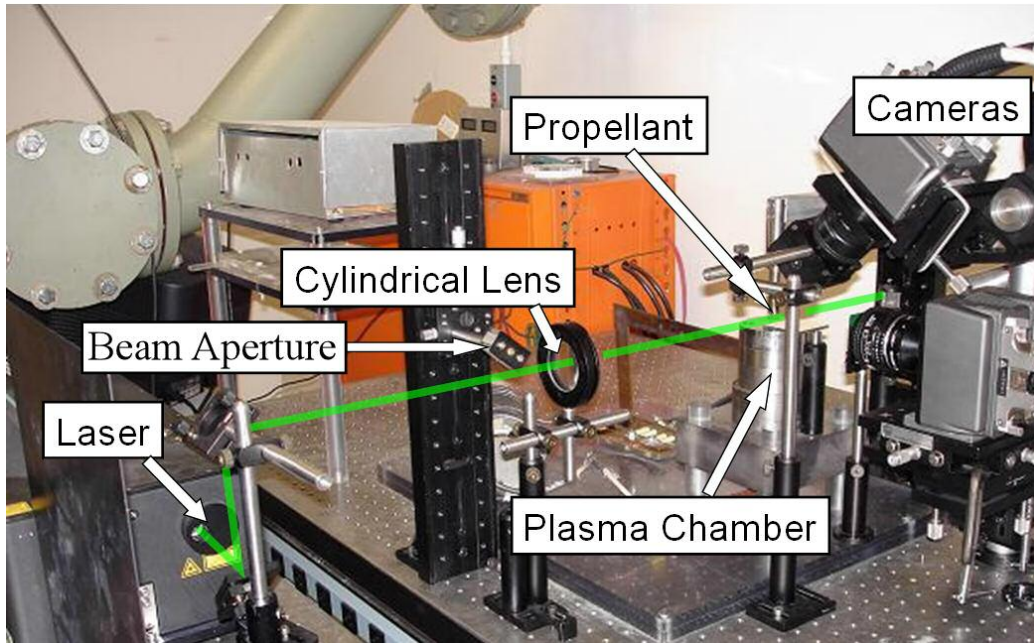


Figure 3.6: Experimental setup of the two camera simultaneous imaging experiment.

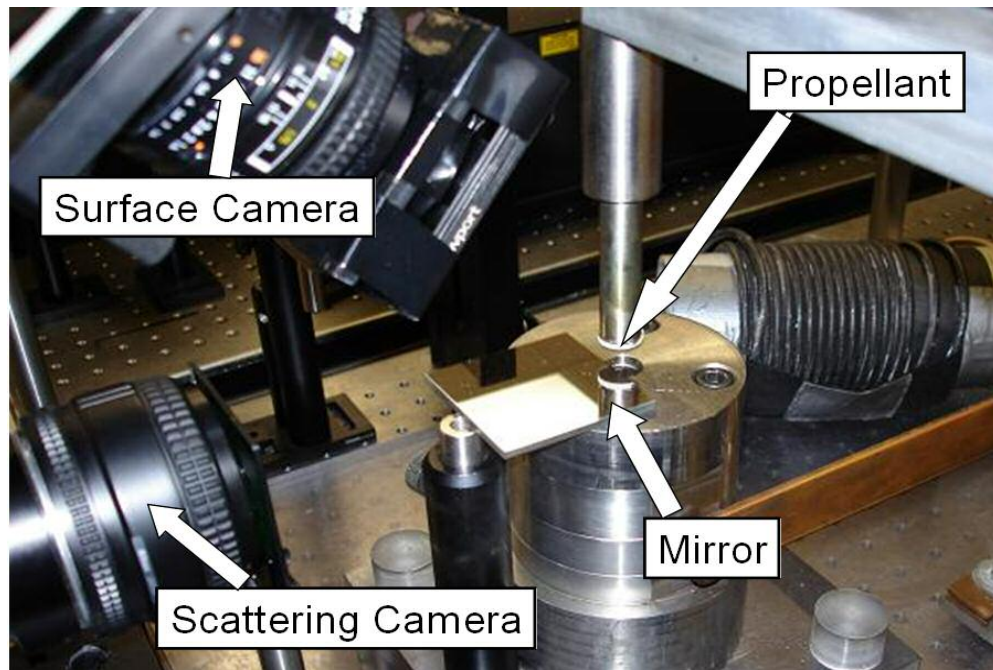


Figure 3.7: Close up view of two camera simultaneous imaging experiment.

Figure 3.8 shows the size and geometric relation of the fields of view for both cameras. The method of viewing simultaneous images of two different planes on the same plot is explained. Part a) shows the point of view of the observer for all the cross-plane plots in this work. Part b) shows an example plot in relation to the two surfaces with fields of view dimensioned. The laser sheet is perpendicular to the propellant surface and translates across the middle of the propellant surface camera field of view. Both surfaces are marked in the figure. The field of view for the cameras was only 10.3 mm wide, smaller than the 12.7 mm propellant disk diameter, and the width of the patch of propellant surface viewed by the camera is 3.2 mm. The laser scattering camera views the area 5.1 mm below the propellant surface.

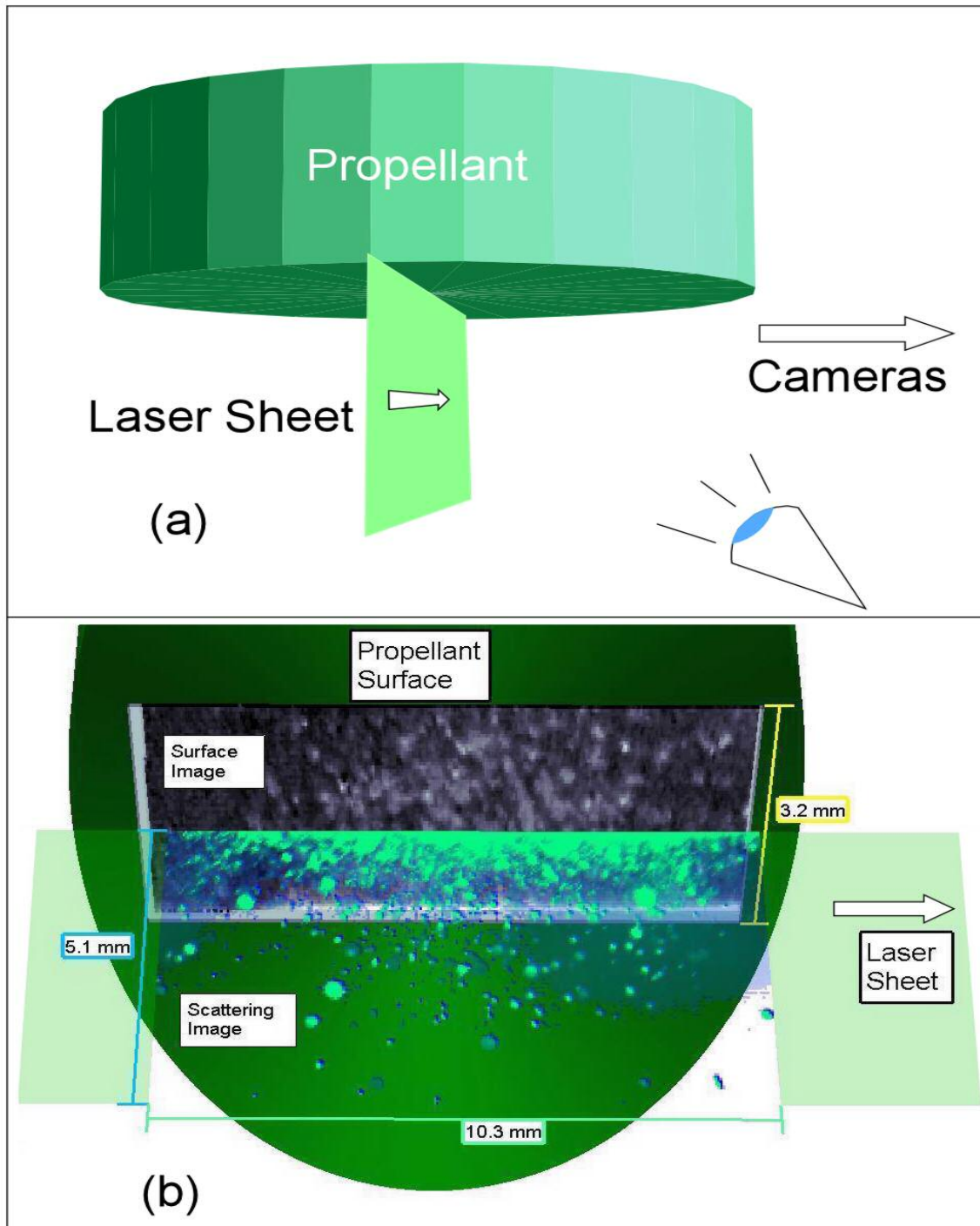


Figure 3.8: Field of view geometry for both cameras a) Diagram of observer position for cross-plane plots b) Relationship of the camera fields of view for scattering and surface images.

Chapter 4: Experimental Methodology and Background Theory

CURRENT MEASUREMENTS USING A ROGOWSKI COIL

All current measurements taken during the plasma firing were produced using a Rogowski coil. Rogowski coils operate on a simple principle. An ‘air-cored’ coil is placed in a toroidal fashion around the conductor from which the current is to be measured and the magnetic field produced by the current induces a voltage in the coil. The following analysis is summarized from Ward and Exon (1993).

If a line is drawn in a loop that totally encircles the current to be measured then, according to Ampere’s Law, the line integral of the magnetic field around that loop is equal to the net current enclosed by it no matter what path the loop takes. This is expressed as

$$\oint H \cos \alpha dl = i ,$$

where dl is a differential length along the loop, H is the magnetic field and α is the angle between the direction of the field and the direction of the element. The example Ward and Exon (1993) use is a long, thin helical coil, with n turns per meter and cross-sectional area A which surrounds a conductor carrying a current i . In a section of length dl the number of turns is ndl and the magnetic flux across the section is

$$d\Phi = \mu_0 H A n dl \cos \alpha ,$$

where H is the magnetic field, and α is the angle between H and the axis of the coil. Integrating the flux along the coil using Ampere’s Law to evaluate the integral gives

$$\Phi = \int d\Phi = \mu_0 n A \oint H \cos \alpha dl = \mu_0 n A i .$$

From Faraday’s Law the voltage in the coil is:

$$v_{coil} = -\frac{d\Phi}{dt} = -\mu_0 n A \frac{di}{dt} .$$

Current is then found from the time integral of the voltage across the coil:

$$i_t = \frac{-1}{\mu_0 n A} \int_{t=0}^t v_{coil} dt .$$

The coil is made according to a method described by Nalty et al. (1984) The coil has 95 turns wound around a BNC coaxial cable and is covered with heat shrink tubing for protection. The two leads of the coil are connected to the BNC cable which is directly connected to a Tectronix digital oscilloscope.

The total charge in the capacitor before the firing is known, so current data can be calibrated by measuring capacitor voltage and noting when the capacitor voltage reaches zero. The total charge Q on the capacitor is

$$Q = C \cdot V_0 ,$$

where C is the capacitance and V_0 is the initial voltage. Integrating the current over time produces the charge drained from the capacitor

$$a \int_0^{t(v=0)} i dt = Q = C \cdot V_0 ,$$

where i is the arbitrary current, a is the calibration constant, and the quantity ai is the actual current.

Sources of measurement error include displacement current, magnetic induction around the main loop, and possible leakage through the coil insulation. Displacement current is an effect of the changing electrical field in the area surrounded by the coil. In order to account for these errors, voltage is measured in the coil during a plasma firing when the coil is not around the discharge conductor but oriented in the same direction as when it is around the conductor. In addition, Tian et al. (1999) suggest taking measurements with the Rogowski coil without the plasma firing to measure possible errors due to initial circuit loading. This was done and the effect was found to be negligible. Figure 4.1 shows voltage measurements made (a) with the Rogowski coil around the conductor and (b) adjacent to the conductor. The main contribution to the

displacement current is the voltage across the capillary, and the major source of induction and leakage is the copper rod the coil is resting on. Thus, the voltage contribution in the coil from these error sources should be accurately measured because the coil is situated nearly the same with respect to both entities. The error voltage trace has nearly the same shape as the normally measured voltage trace with a magnitude around 10% of the nominal value. Thus the corrected trace is a slightly scaled down version of the original trace.

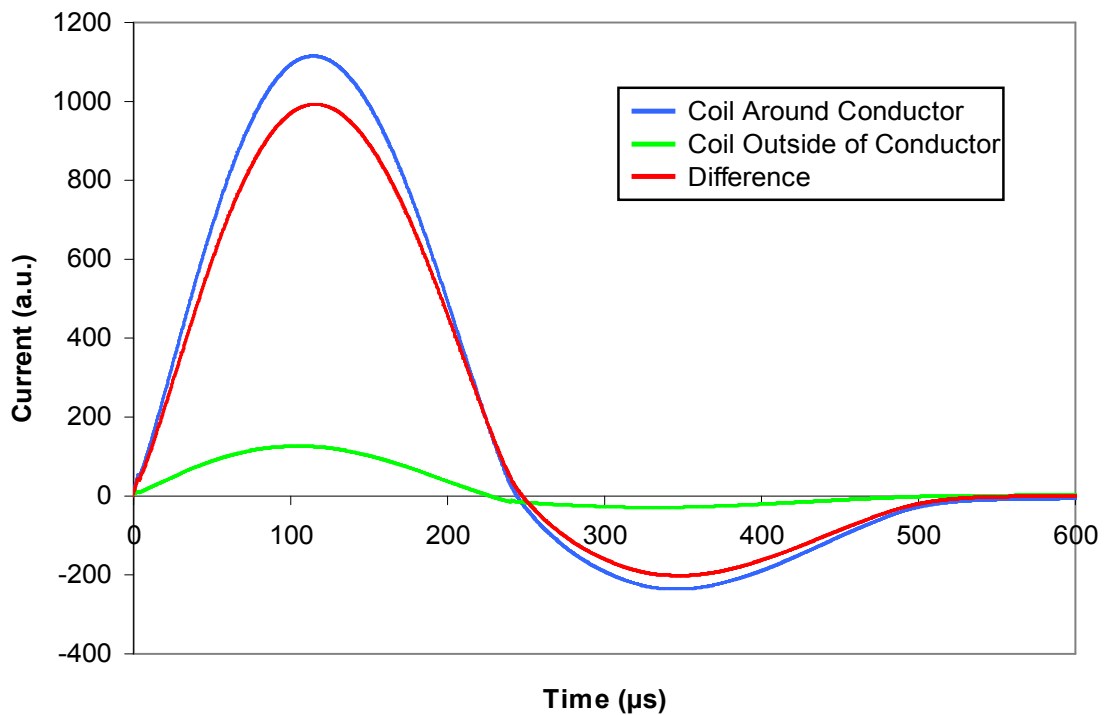
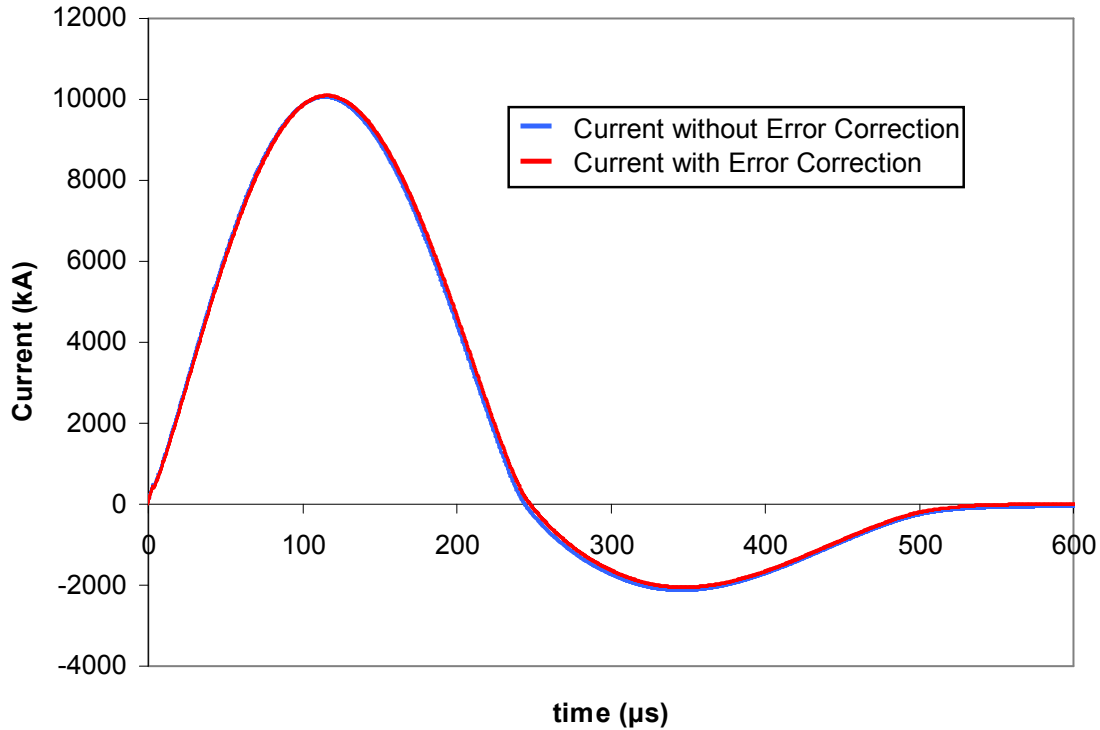


Figure 4.1: Integrated voltage (\propto current) in Rogowski coil during plasma discharge with conductor inside coil, conductor outside coil, and the between the two.

Figure 4.2 shows an example of calibrated current using the normally measured voltage data and the corrected voltage data. Because of the scaling of the calibration

method the calibrated current traces are virtually identical because the shapes of the two



voltage curves are nearly the same.

Figure 4.2: Calibrated current with and without error correction.

EXPERIMENT TIMING

All experiment timings rely on an in-house built timing circuit. This device receives a repetitive TTL signal as input, and when a button is pressed, outputs a single TTL pulse from the “short delay” output that rises in time with the next TTL input pulse, and falls at a user set delay time. The falling edge triggers an output of -20 V, which in turn triggers the ignitron switch that discharges the capacitor.

For plasma experiments that need one trigger signal such as emission spectroscopy, pressure transducer measurements, and photodiode readings a pulse generator (Berkeley Nucleonics Inc., Model 500) supplies a 10 Hz signal to the timing circuit. The short delay output is input into a delay generator (Stanford Research Systems DG535), which then triggers the experimental device. This can be seen in Fig. 4.3.

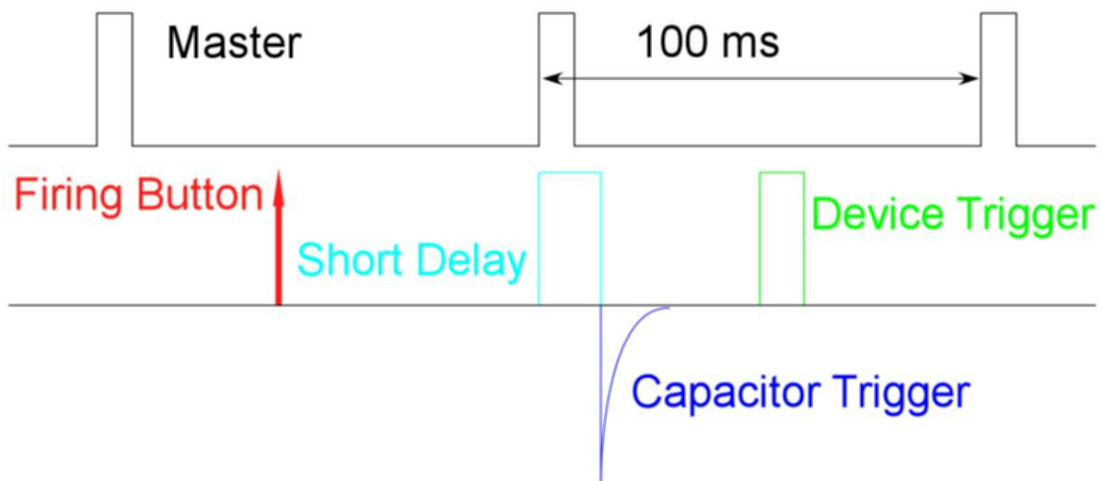


Figure. 4.3: Experimental timing for a single trigger device

For other experiments, the exposure of a camera must be synchronized with a laser, at a specific delay from the plasma trigger. Two lasers have been used with specific cameras for each type. The 10 Hz Nd:YAG laser, used for PLIF and scattering experiments, is captured by Roper Scientific PI-Max intensified CCD camera. The 10 kHz Nd:YLF laser, used for high repetition rate scattering imaging, is captured by a Photron Fastcam Ultima APX high speed camera. For the 10 Hz laser experiments, only one laser pulse occurs during the plasma discharge, so only one image is captured per firing. With the 10 kHz laser, 6 laser pulses occur during the 600 μ s plasma discharge.

For the 10 Hz experiments the master timer was the pulse generator. It was found to be more accurate between consecutive pulses than the laser Q-switch. A diagram of the 10 Hz experiment timing is shown in Fig. 4.4. The laser Q-switch and the timing circuit were triggered by the pulse generator. The camera was triggered by the short delay output on the timing circuit delayed by a Stanford Research Systems DG535 delay generator. The delays between the master timer and the timing circuit trigger and the short delay output to the camera trigger were determined by the desired timing of the laser pulse with respect to the discharge initiation. Figure 4.4 shows an example delay of 300 μs from the beginning of the capacitor discharge. The figure is not to scale.

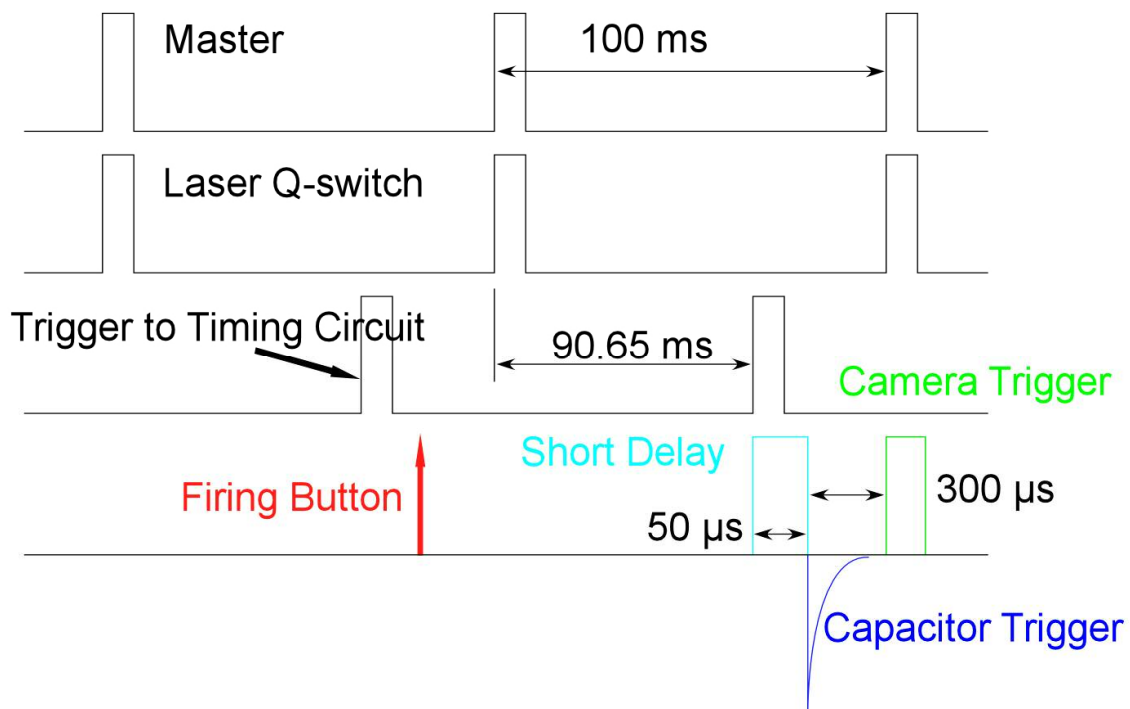


Figure 4.4: Experimental timing diagram for a 10 Hz laser experiment during a plasma firing.

A diagram of the 10 kHz laser experiment is shown in Fig. 4.5. For this experiment the master timer was the laser Q-switch. Before the firing the APX camera

was running continuously in synchronization with the laser. The 10 kHz signal was frequency divided to 100 Hz before being input into the timing circuit. The short delay output was used to trigger the recording of the camera. The camera was set to “center recording mode”, which means half of what the camera records happens before the record trigger, and half happens after. In experiments where a second APX camera was running at 50 kHz, it was not synced to the laser. Because of EM interference from the capacitor discharge, timing had to be run from the Nd:YLF Q-switch. The trigger to the second camera was the same trigger as the first. However, the second camera’s timing was internally controlled. When two cameras were used, both cameras were run on random-reset mode with 100 images taken for each trigger. This ensured image timing was slightly offset and the propellant surface camera did not capture laser scattering. The in camera exposure timing was recorded on a Tektronix TDS 520C digital oscilloscope by recording the exposure sync signal. This provided exact information on when individual images from two different cameras occurred.

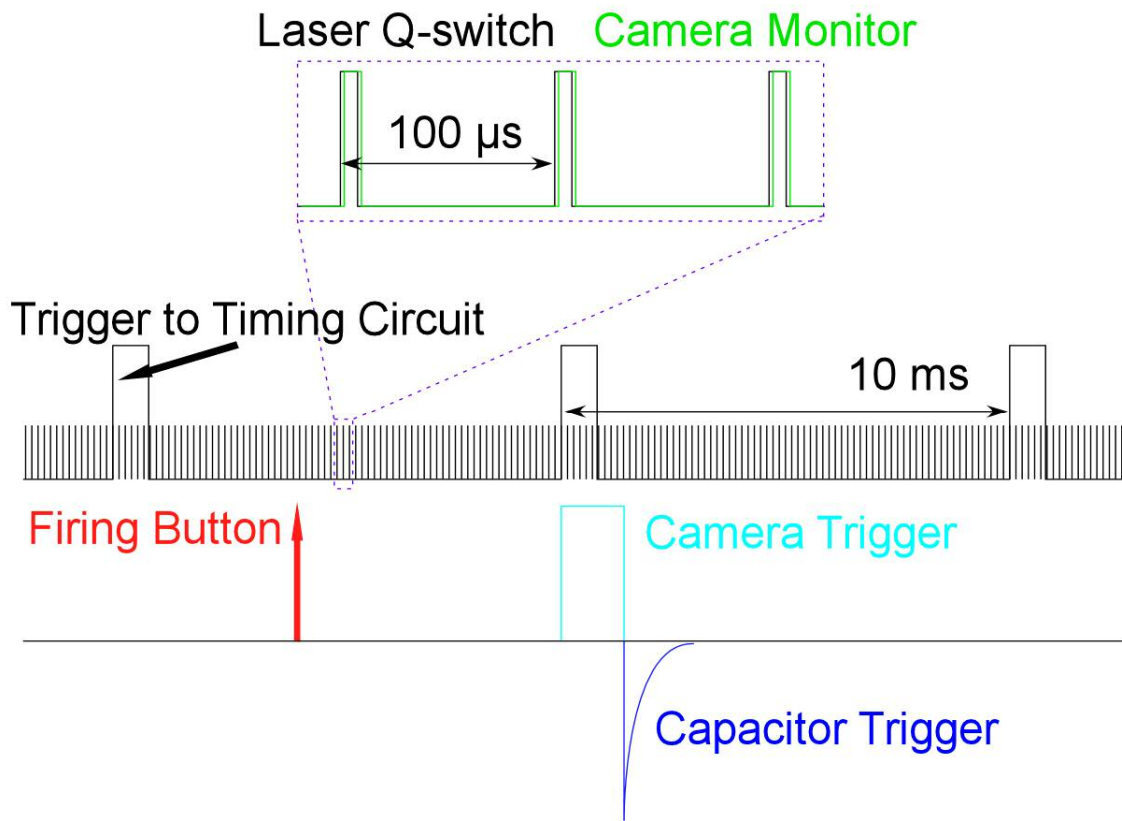


Figure. 4.5: Experimental timing for 10 kHz laser.

MEASURING LASER SHEET WIDTH

In the simultaneous two camera laser scattering and propellant surface imaging experiment it is useful to know the volume irradiated by the laser passing under the propellant. The sheet width was measured using the method described by Mauck (1979). The full power Evolution 90 Nd:YLF laser sheet (nominally 90 W) was created by the same method as in the two camera experiment. The sheet was then directed onto a beam dump. A photodiode observed the beam dump where the laser hit it from about 5 cm distance. A razor blade was translated horizontally across the laser sheet by a translation stage accurate to 25 μm and intensities were measured at regular intervals. In this way the

photodiode measured maximum intensity when the razor was completely out of the beam and negligible intensity when the laser completely blocked the beam. To minimize inaccuracies resulting from thermal expansion of the razor and to avoid melting the razor blade the translation was conducted as quickly as possible.

Figure 4.6 shows the normalized measured intensity from the photodiode as a function of razor blade position. The beam profile is assumed to be Gaussian. In order to find the beam width the intensity data compiled by translating the knife-edge across the beam is fit to the complimentary error function

$$I(x) = 1 - \frac{1}{\sigma} \sqrt{\frac{2}{\pi}} \int_{-\infty}^x \exp\left(-\frac{(t-x_0)^2}{2 \cdot \sigma^2}\right) dt .$$

Here I is the normalized laser fluence, x is the position, x_0 is the peak position is the standard deviation and t is a dummy variable. The full width at half maximum of the beam is defined as $2.355 \cdot \sigma$. The photodiode signal was read every $127 \mu\text{m}$ for this run. A second run was conducted with better spatial resolution (every $50.8 \mu\text{m}$) and the beam profile and intensity fit can be seen in Fig. 4.7. The halfwidth calculated from each of the fit curves is 0.449 and 0.459 mm respectively. Using an average of the two seems reasonable and so the halfwidth of the Nd:YLF laser sheet is 0.454 mm.

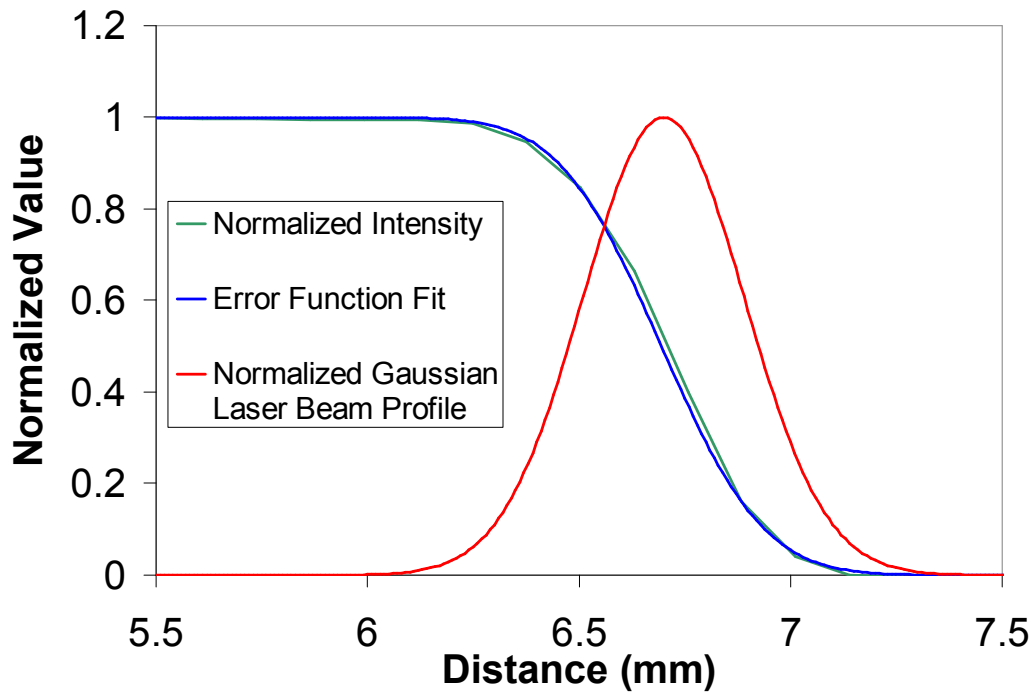


Figure 4.6: Photodiode intensity as the knife edge is translated across the laser beam with error function fit and resulting Gaussian beam profile.

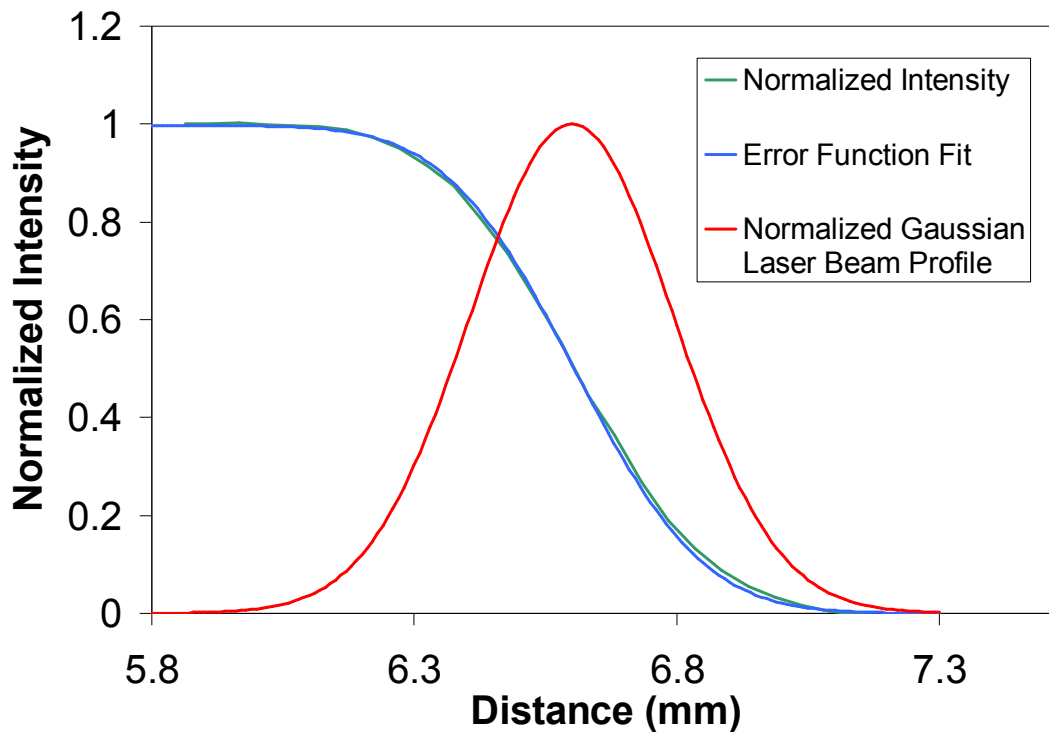


Figure 4.7: Laser beam profile from second razor translation using a higher spatial resolution.

PLANAR LASER INDUCED FLUORESCENCE THEORY AND NITRIC OXIDE SPECTRUM

Planar laser-induced fluorescence is a very powerful measurement technique that has been used to measure temperature, species concentration, pressure, and velocity in fluid flows (Hanson et al. 1990). The majority of fluorescence measurements depend on pumping electronic transitions of a single species with a laser tuned to resonance, and comparing the resulting emissions. Multiple lines can also be pumped using multiple lasers at the same time, or if flow conditions allow it, using a single laser and comparing average fluorescence signals from multiple transitions to produce an average quantity.

In fluorescence of a diatomic molecule like NO, the electronic, vibrational, and rotational quantum energy states are important. Consider a two quantum state model of a

number of molecules like that of Fig. 4.8. A transition from the lower quantum energy state E_1 to the higher energy state E_2 is stimulated by the incident laser light (the energy of the photon being the same as the transition energy). The molecules can return to the lower energy state over time through the processes of spontaneous emission and stimulated emission of photons, and transfer of energy through collision with other molecules. W_{12} and W_{21} denote stimulated absorption and emission rates respectively, A_{21} is the spontaneous emission rate, and Q_{21} is the collisional deexcitation rate. In general the spontaneous and stimulated emissions that produce fluorescence signal are competing with collisional quenching to reduce molecules in the upper energy state to the lower energy state.

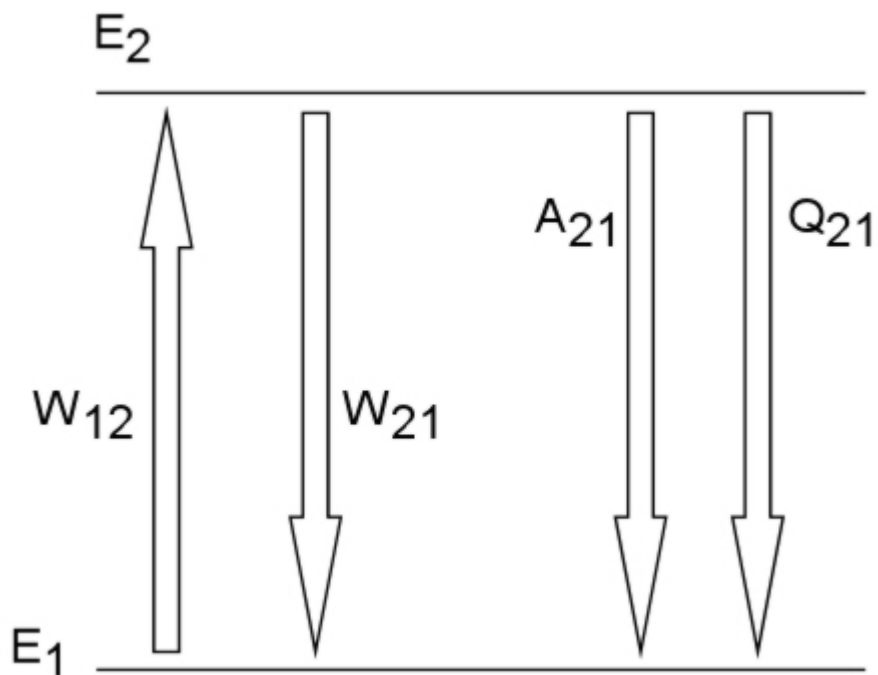


Figure 4.8: Diagram of a two level model for laser induced fluorescence.

A complete NO energy state description, even when dealing with only two states in the pump transition, includes many other possible electronic, vibrational, and rotational states as options for relaxation transitions. The electronic transition pumped for this work is from the ground state 2 to the first excited electronic state $^2+$. The vibrational quantum numbers for any transition are denoted by v' and v'' for the lower and upper states respectively. For the pump transition $v'=0$, and $v''=0$. The rotational quantum number is denoted by J . All rotational transitions are denoted by $Y_{ij}(J'')$ where $Y=\{P,Q,R\}$ corresponds to the allowed transition such that $J=J'-J''=\{-1,0,1\}$. The subscripts i and j refer to the spin coupling of the upper and lower rotational levels, respectively. The full description of the pumped transition is $A^2+(v'=0)\cdot X^2(v''=0)$, using the rotational transition pair $Q_{21}+R_{11}(9.5)$ at 225.9802 nm. Because maximum fluorescence signal is desired, light from a spectral band between 230-280 nm is imaged, cutting out possible elastic scattering from the pump beam but observing light from all lower energy photons resulting from the same electronic transition but different vibrational and rotational transitions.

LASER CALIBRATION FOR NO PLIF

The dye laser used in the current study (Lumonics, Hyperdye 300) was calibrated for wavelength by creating an NO excitation scan. The technique is to scan the dye laser continuously across a range of wavelengths while detecting fluorescence produced by passing the laser through a test cell containing NO. The resulting absorption spectrum is compared to a calculated absorption spectrum and each laser wavelength setting is thereby calibrated to actual wavelength. For this experiment the wavelength desired is produced by the apparatus shown in Fig. 3.3. The frequency doubler and wave mixer are both Inrad Autotracker II's and can automatically position the doubling and mixing crystals for optimum laser energy as the laser is scanned. The sealed test cell was filled

with 25 ppm NO in N₂ at atmospheric pressure. The test cell has fused silica windows on three sides, two to pass the laser and the third to view fluorescence. The detector is a Hamamatsu photomultiplier tube (PMT) powered at -500 V with a UG 5 filter to attenuate the laser scattering. Because the laser and resulting fluorescence signal are pulsed, the PMT signal is input into a Stanford Research Systems gated boxcar averager. The boxcar averager gates the PMT signal so that only the fluorescence is recorded. The averager, set to 30 pulses, then averages that number of sequential pulses to average out individual variation in laser pulse energy. The laser is scanned at a rate of 0.0005 nm/s, and the averager output is recorded on a digital oscilloscope (Tektronix TDS 520 C).

The wavelength corresponding to the laser controller setting is calculated using the formula:

$$wavelength = \frac{1}{\frac{2}{laser_setting} + \frac{1}{1064}}.$$

The calculated absorption spectrum was produced using the software “Lines” and “Spectra” (Seitzman ©1985-1990). A calibration constant is added to the experimental curve to match the two spectra. The experimental absorption spectrum did not match up exactly with the calculated spectrum. There are a few probable reasons for this. The fluorescence signal measured by the PMT was very low, possibly due to the low concentration of NO in the test chamber and low laser energy. The power curve of the pyromethene dye used in the dye laser creates the rise in intensity seen as the wavelength decreases. Also, it is possible the dye laser bandwidth was not narrower than the absorption peaks of NO. In any case, matching the peaks between the experimental and calculated spectra is the best way to calibrate the laser, and nowhere else on the calibrated spectrum do the two sets of peaks match.

CAMERA REGISTRATION

In order to correlate the particles leaving the propellant with the objects seen forming on the propellant surface in the simultaneous two camera experiments, the two cameras must be registered to determine the laser beam location relative to the propellant surface. Two surface grids were created as shown in Fig. 4.9. The grids, printed on paper, were created using Microsoft Excel, placing + signs at even spacing. One fiducial mark was placed in each grid so that the placement of each grid in relation to the other was known. The surface grid corresponding to the laser sheet was fastened to the side of an aluminum plate 9.5 mm thick with double sided tape. The propellant surface grid was fastened to a sheet of polycarbonate and then fastened to the orthogonal side of the same aluminum plate. Once the device was placed on the plasma chamber, the propellant grid surface was the same distance from the chamber as the propellant would be. The grids were aligned such that the fiducial marks were on gridlines that met at the vertex of the two surfaces. The horizontal spacing of the grid points was 0.90 mm while the vertical spacing was 0.81 mm.

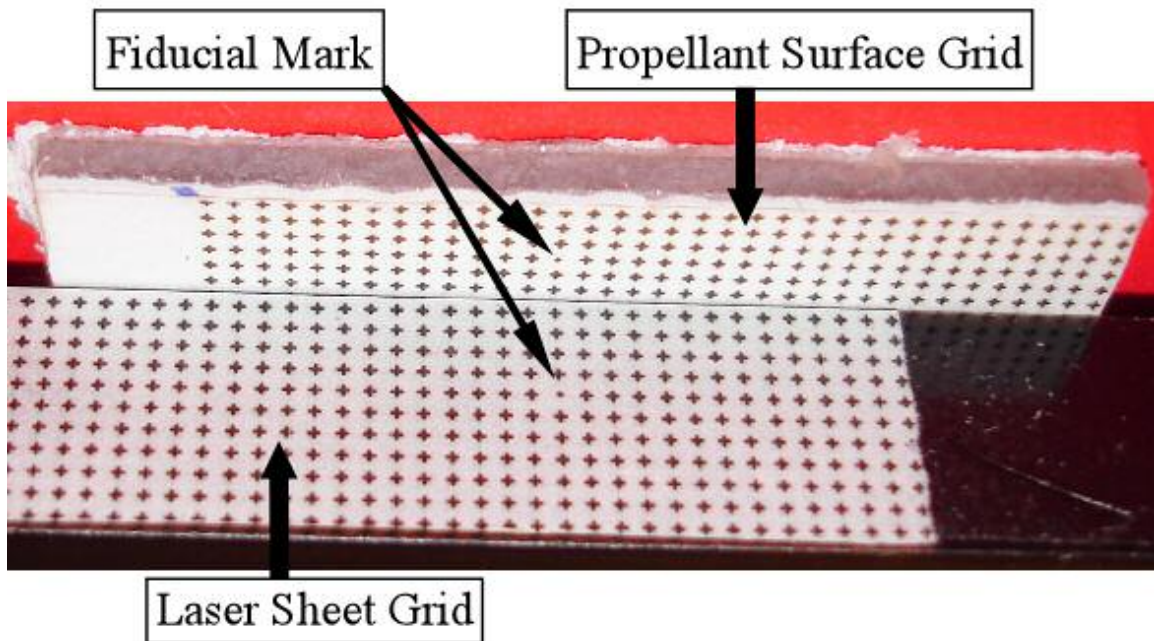


Figure 4.9: Image of the two surface grid used for camera registration.

The grid device was placed on top of the plasma chamber and carefully aligned with the laser sheet. Images were taken by each camera using larger CCD areas than during the experiment so that the resulting camera transformations would be more accurate. Figure 4.10 is a sample image of the laser surface grid by the laser camera. Figure 4.11 is a sample image of the propellant surface grid by the propellant camera. The propellant surface is upside down and distorted because of the mirror used and the angle of the camera. The registration was done in Matlab by graphically choosing the fiducial mark and the four grid points at the corners of each surface and recording their spatial position through calculation using the known grid spacing. The position of the vertex between surfaces was recorded in each grid image. Care was taken when building the grid device and positioning the laser camera so that neither the laser grid nor the camera were at an angle with respect to the propellant grid surface. Therefore the laser camera images did not need to be transformed.

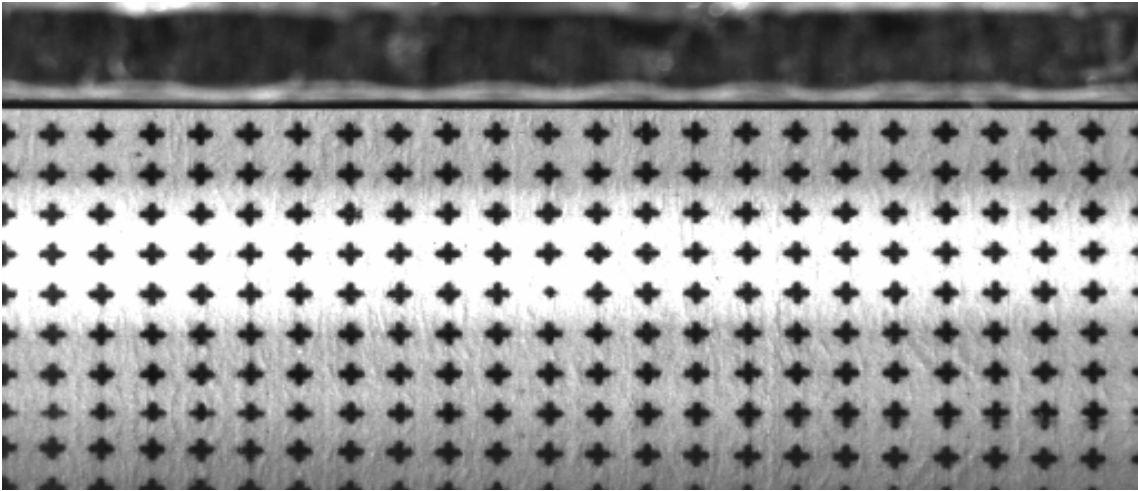


Figure 4.10: Image of the two surface grid by the laser scattering camera.

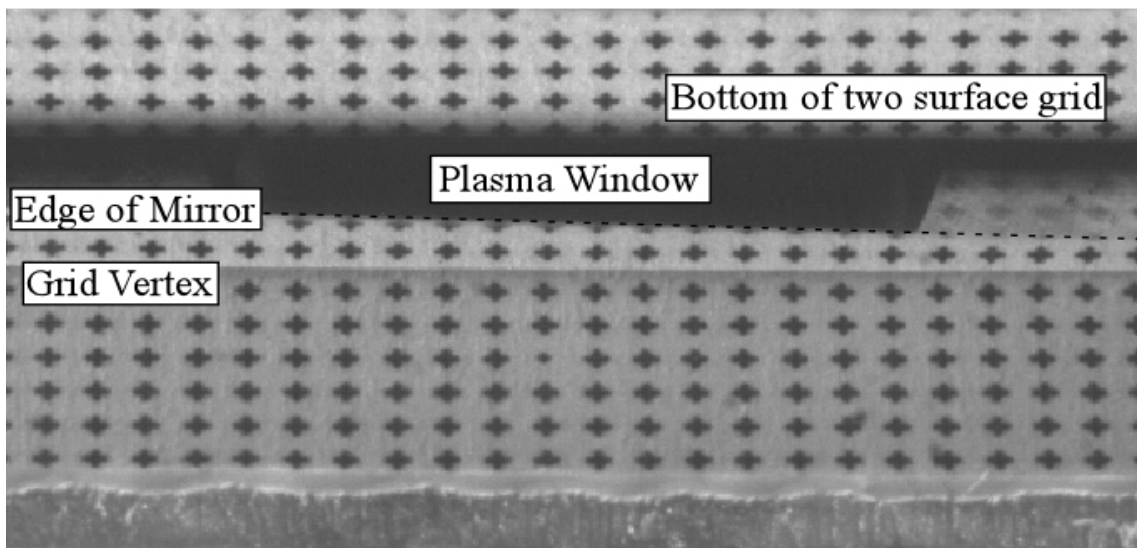


Figure 4.11: Image of the two surface grid through the mirror by the propellant surface camera.

A projective transform was created in Matlab for the propellant surface camera images using the pixel positions of each recorded gridpoint, and the actual positions in real space. Because of the geometry of the grid device only the bottom half of the propellant surface grid image contained measurable grid. The top half began with the

edge of the laser grid surface and also contained parts of the plasma chamber and an unreflected view of the grid device because the mirror did not fill the entire field of view. The transform assumed straight lines remained straight, but parallel lines converged toward vanishing points not in the image, which is consistent with a plane surface viewed at an angle. When transformed, the intensity was bilinearly interpolated. Once the cameras were registered in real space, the images could be plotted as 3-dimensional objects in Matlab. This enabled the original camera images shown in Fig. 4.12 to be visualized as in Fig. 4.13.

Figure 4.13 has both camera images plotted as if the observer is viewing them from below the propellant surface and some distance from the laser towards the cameras. The laser scattering image has been false colored to distinguish it from the propellant surface. Also, the image transparency is variable with the most transparent parts being the lowest intensity. The propellant surface image intensity has been scaled to better visualize the structures forming. In addition the halfwidth of the laser is marked on the propellant surface. This plotting system is used in Chapter 5 to visualize results and enabled qualitative analysis of the relationship between the propellant surface changes and the particles seen by scattered laser light.

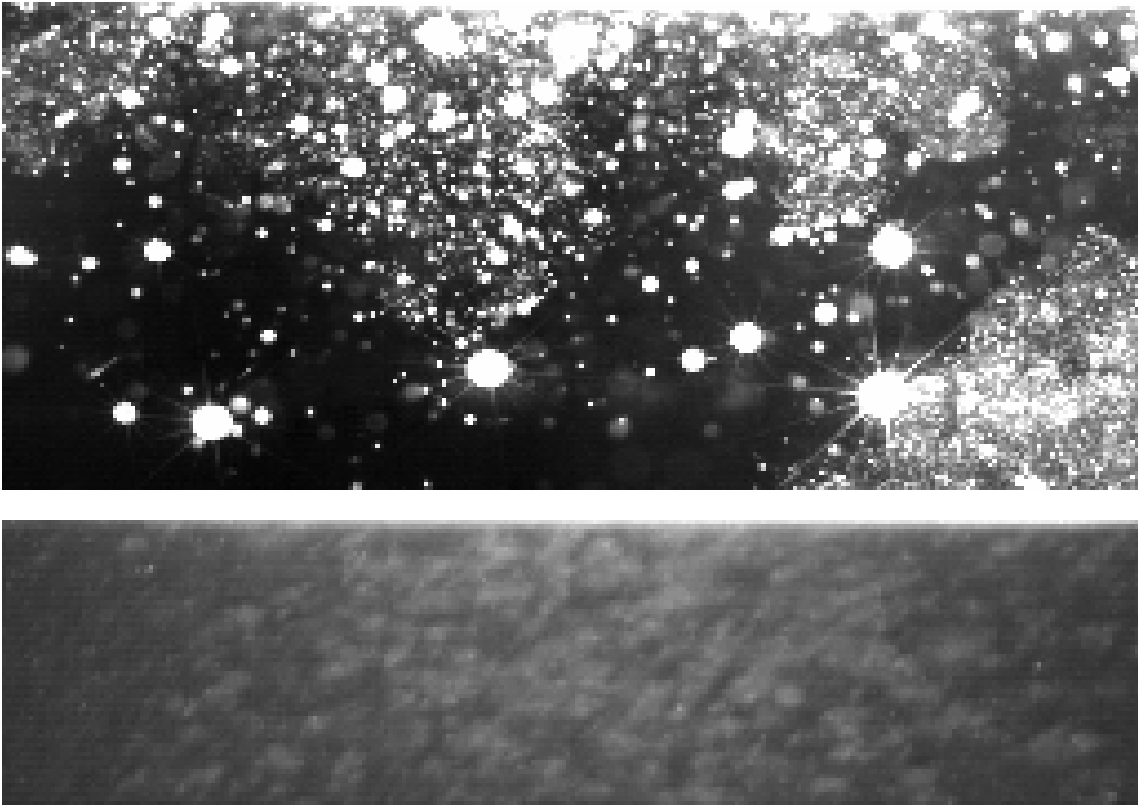


Figure 4.12: Example of original camera images taken during a run. Top image: laser scattering. Bottom image: propellant surface.

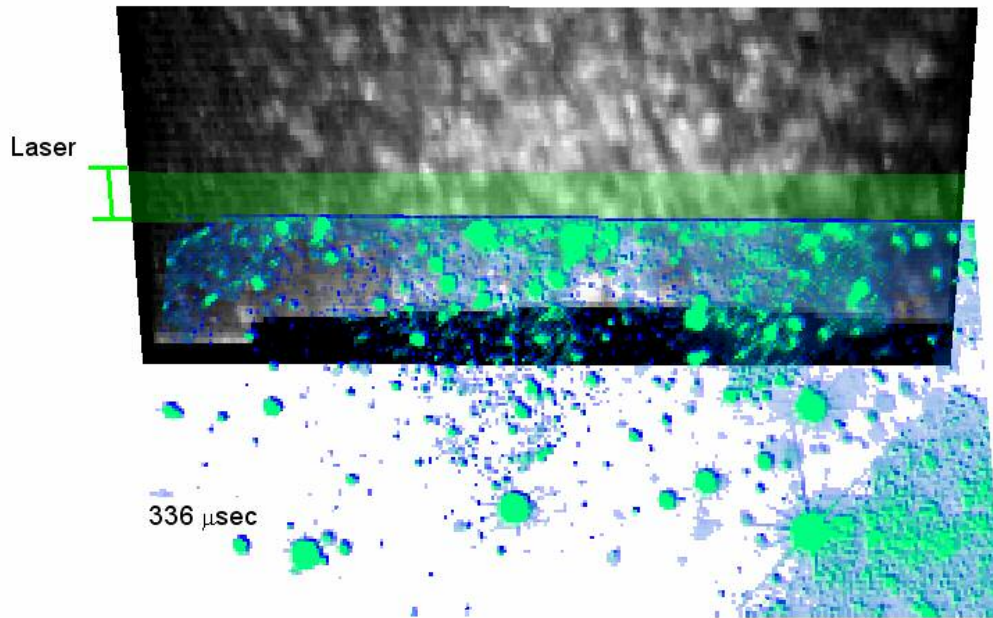


Figure 4.13: Both camera images plotted onto single 3-D graph with laser swath and time delay marked.

JA2 SURFACE SCATTERING SPECTRA

The Ultima APX camera imaging the propellant surface was a monochrome imager. To the eye pristine JA2 propellant is green, and JA2 that has reacted due to plasma radiation is yellow to white. Without color imaging, there were difficulties distinguishing between reacted surface and pristine surface. By studying the surface scattering spectra of both pristine and reacted regions of the propellant surface, it was hoped a filter might be found to help distinguish between the two. A white incandescent lamp illuminated the surface of a propellant sample. Light scattering from a 400 μm spot on the propellant surface was focused onto a 400 μm fiber optic cable. This cable was

connected to an Oriel MS260i imaging spectrograph (257 mm focal length, 1200 l/mm grating) equipped with an Newport 78105 CCD linear array detector. The instrument had a spectral range of about 42 nm. The scattering spectra were measured across the entire visible range by varying the center wavelength of the spectrograph. Ten 0.5 s exposures at each wavelength setting were averaged to increase signal to noise. The resulting spectra have been calibrated for wavelength response but not calibrated for pixel position response. Figure 4.14 shows reflection spectra from both the pristine and reacted surface across the entire visible range. Both types of surface scatter light across the entire visible spectrum. On average the partially decomposed surface reflects around four times more light than the pristine surface. In order to compare the shape of the two spectra the pristine surface spectrum was rescaled in Fig. 4.15 so the magnitude matched the reacted surface spectrum. The shapes of the spectra are generally the same, with the pristine surface possibly having a slightly higher reflectance below 600 nm compared to the reacted surface. While an OG 570 color glass filter was used to take advantage of this (in addition to blocking out UV light), it probably had negligible effect because the reflectance of the reacted surface is so much greater across the entire spectrum.

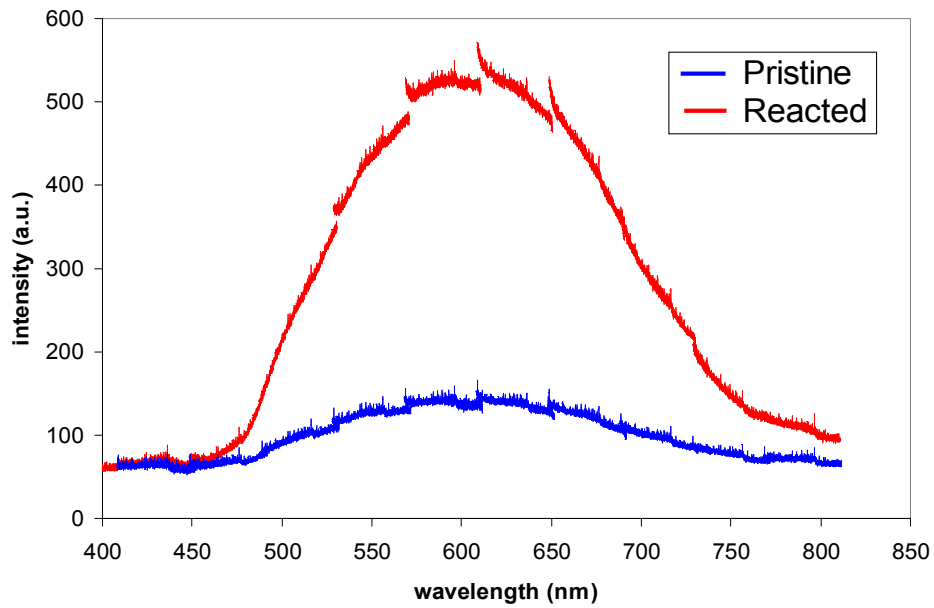


Figure 4.14: Visible reflectance spectra of pristine and decomposed propellant.

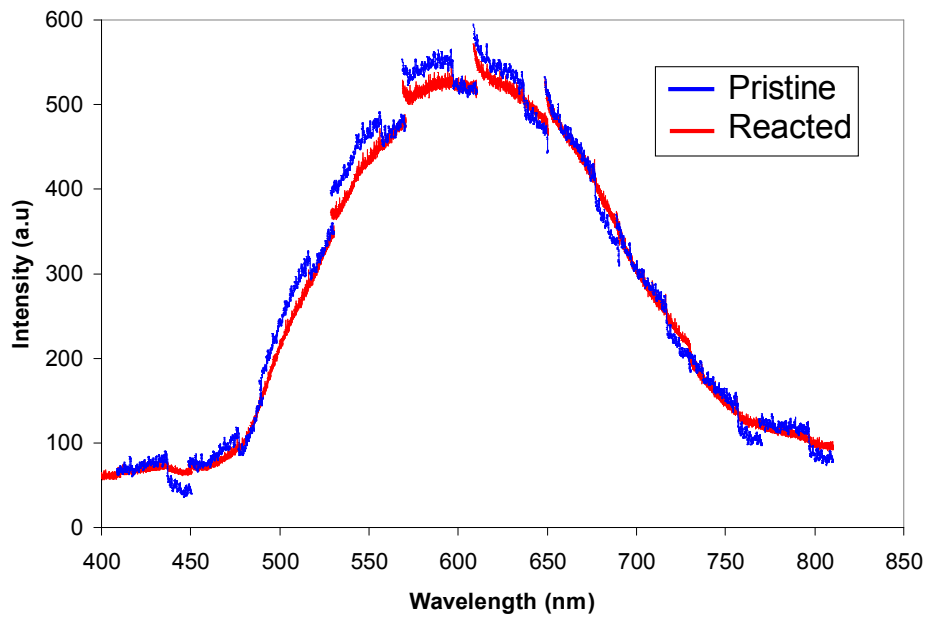


Figure 4.15: Rescaled pristine reflectance spectrum rescaled to compare with the reacted reflectance spectrum.

TRACKING PROPELLANT SURFACE IMAGE CHANGES

Because of the complex geometry of the structures observed on the propellant surface, an image processing technique was sought to help understand how the propellant surface responded to the plasma radiation. Computer analysis helped ensure that the technique was thorough and consistent, and exact within the parameters of the algorithm. Differencing is the most basic image processing technique to track moving objects in a video image. By subtracting one image from another the changes between the two images appear as brighter or darker regions than the rest of the image, depending on whether the object moved to or from the region. Variations of this technique were explored to track how the structures on the propellant surface formed and grew as the plasma discharge progressed. Comparing one image in the sequence with the previous image would enable observation of which regions were changing.

Because the camera was a monochrome imager, the only information to distinguish between pristine propellant surface and decomposed propellant was intensity. A method of defining the edges of the reacted structures according to intensity and then determining how those edges changed was explored. However, the following problems ultimately led to using a different technique. A close look at propellant surface images shows that there is not a dramatic dropoff in intensity to pristine propellant at the edges of the affected structures. A threshold would have to be defined to distinguish between reacted and unreacted propellant. There were spatial and temporal variations in illumination that made a single threshold inaccurate over all the images in the sequence. Color imaging would be most useful in this situation because the variable illumination would not change the relative color intensities. In addition to the variable illumination, most of the observed changes in the images was not due to new regions being affected,

but of previously affected regions becoming relatively brighter. This increase in relative brightness was assumed to be an increase in the level of decomposition in the propellant.

In order to account for changes in brightness in both unaffected and previously affected regions of the propellant and to be able to handle variable illumination, a method using division of consecutive images was created. The following assumptions had to be made to relate what the changes recorded by the camera to the physical changes occurring on the propellant. First, it was assumed that

$$\text{camera signal} \propto \text{plasma light intensity} \times \text{reflectance}.$$

Also, it was assumed that the reflectance was proportional to the level of reaction in the propellant. The first assumption ignores dark charge and camera noise. The dark charge is assumed to be negligible because of the high frame rate, and the shot noise was ignored. Noise only caused problems in the relatively low light at the end of the discharge. While the reflectance might not vary linearly with respect to the level of reaction, the basic assumption of reflectance increasing with increasing reaction is probably sound.

This method used to determine image changes is not unique, nor has it been optimized. It was arrived at through trial and error on variations of both image subtraction and division. It was used because it did an acceptable job of finding where the propellant was changing (as observed by eye). Raw propellant surface images were compared by the formula

$$\frac{R_2}{R_1} = \frac{S_2 / L_2}{S_1 / L_1}.$$

Here R is level of reaction, S is camera signal, L is plasma illumination intensity, and the subscripts 1 and 2 denote the first and second image. An area where decomposition is occurring is brighter than the rest of the image using this formula. The illumination

intensity L was estimated by averaging an area of 15×15 pixels surrounding the pixel in question. The resulting ratio image was high pass filtered to keep only the decomposition structures and noise was reduced by the same method as the propellant surface images in Fig. 5.13. A threshold was chosen by trial and error to separate structure growth from unchanged regions.

Particles offset from the propellant surface illuminated by the plasma light sometimes appear in the propellant images. They appear as regions of change in the ratio images. Regions of change that appear in one image and disappear in the next can be removed by comparing consecutive ratio images.

An example image and the corresponding input images can be seen in Fig. 4.16. Looking at the two input images side by side, it is difficult to see the s. However, viewing them one on top of the other shows that the method is fairly accurate. There are situations where the method is unreliable. For example, the method has trouble on the edges of the image where there is a large gradient in illumination. This can produce large connected regions of change that are not real. Also, the method is biased towards fast large changes in the surface. Slight changes will not be separated from the rest of the image by the threshold. Finally, this method is probably inaccurate when the propellant illumination is changing rapidly at the beginning of the plasma discharge.

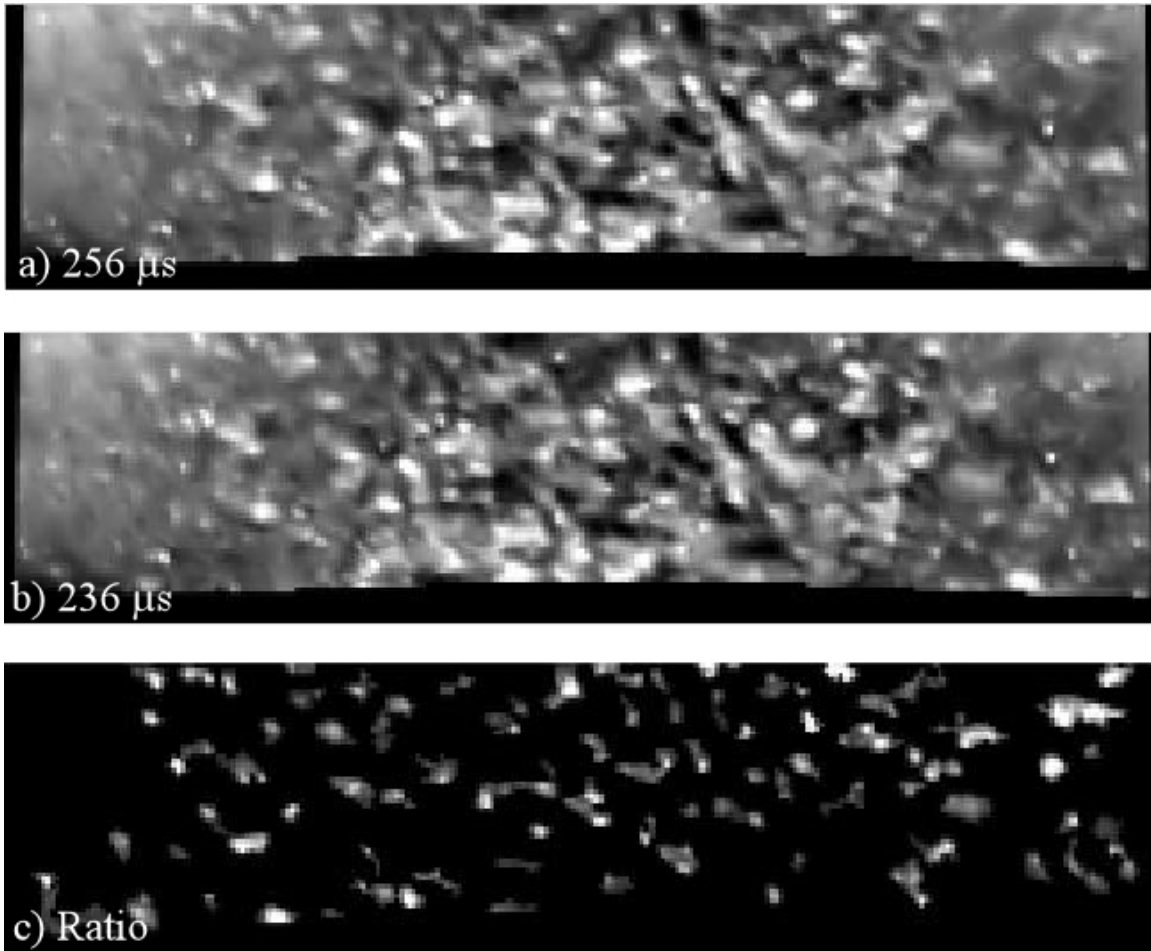


Figure 4.16: Example images comparison technique: a) later image at 256 μs b) earlier image at 236 μs c) ratio image with threshold applied.

CROSS-CORRELATION OF PROPELLANT SURFACE AND LASER SCATTERING IMAGES

A method to compare the changes on the surface above the laser sheet and the scattering particles observed in the laser sheet was devised. The process to create the cross-correlations is diagramed in Fig. 4.17. It was hoped that the particles produced would directly correspond with structures forming on the propellant surface. The scattering images were divided into horizontal strips ten pixels wide which were integrated across their width. The strip of propellant surface image corresponding to the

position of the laser halfwidth was also integrated across its width. The resulting data series, with one data point for each column of image, was transformed by bilinear interpolation to directly correspond to the position of the data series from the scattering image strip. The strips from each camera were cross-correlated using the Matlab function `xcorr`. This function computes an unbiased estimate of the cross-correlation function $\hat{R}_{xy}(m)$ in a length $2*N-1$ vector, where x and y are length N vectors.

$$\hat{R}_{xy}(m) = \begin{cases} \sum_{n=0}^{N-m-1} x_{n+m} y_n^* & m \geq 0 \\ \hat{R}_{yx}^*(-m) & m < 0 \end{cases} .$$

Using the formula

$$R_{xy,unbiased}(m) = \frac{1}{N-|m|} \hat{R}_{xy}(m)$$

corrected for the larger number of data pairs at the smaller separation distances. Implementing this, x and y were the two data series resulting from integration of two camera strips, N was 256, and $\hat{R}_{xy}(m)$ was cropped so that the resulting vector was of length N .

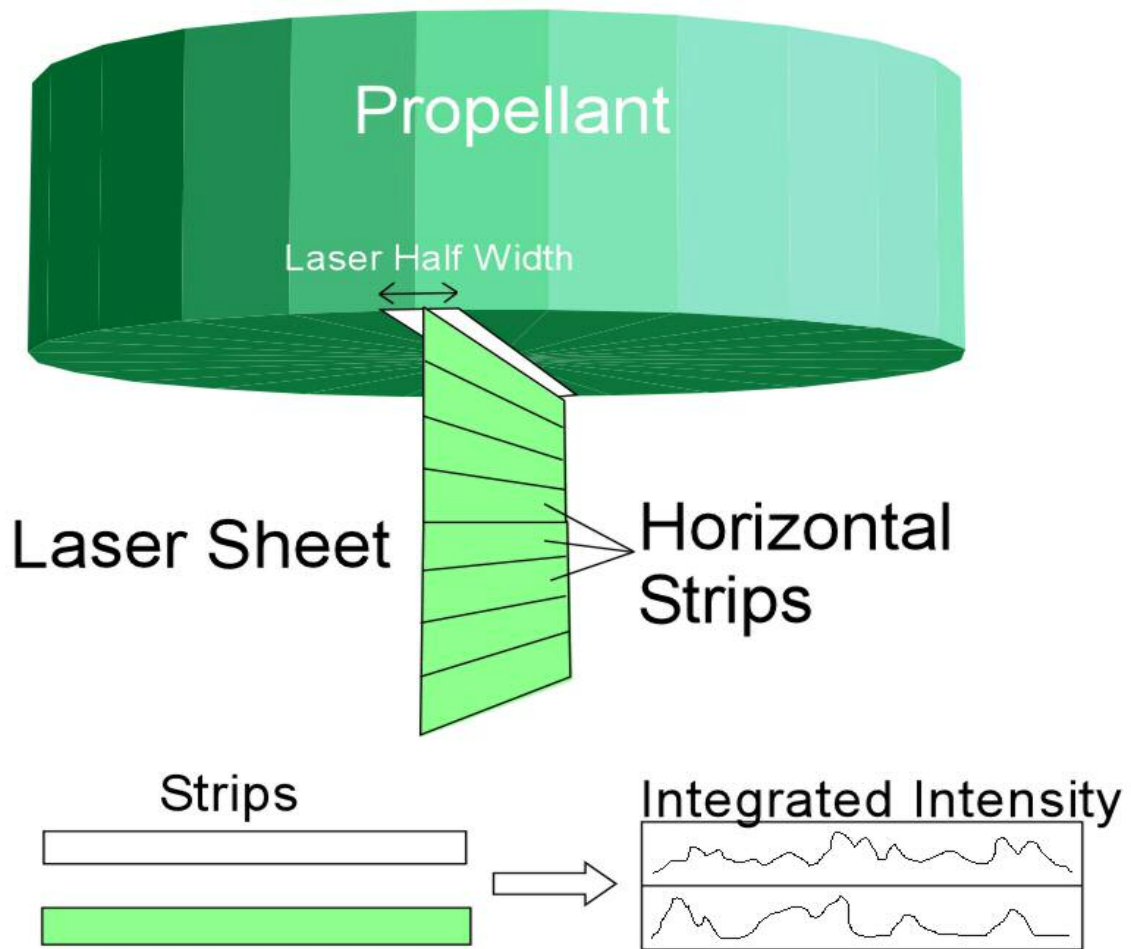


Figure 4.17: Diagram of method to produce vectors used in cross-correlation.

Chapter 5: Results and Discussion

ELECTRICAL CHARACTERISTICS OF DISCHARGE CIRCUIT

The current through the capillary was measured by a Rogowski coil and can be seen in Fig. 5.1. The theory and use of a Rogowski coil to make current measurements was described in Chapter 4. The figure shows the radiation chamber current together with the current for an open air discharge. The current traces are almost the same, as expected, because the discharge circuits are the same. The discharge lasts about 50 μs longer for the radiation chamber setup, which is possibly because the chamber pressure slows the depressurization of the capillary.

By measuring the voltage across the capillary the energy deposited into the plasma can be calculated. The voltage is measured by connecting a fast response 1000 \times voltage divider to the conductors where the current enters and exits the plasma firing assembly. The voltage is then recorded by a Tectronix digital oscilloscope. Power input can then be calculated from the product of the current and the voltage across the capillary, and the cumulative energy into the plasma is calculated by integrating the power over time. Current, voltage, and energy input to the radiation chamber discharge are shown in Fig. 5.2. The total energy deposited into the plasma is 1.68 kJ. This is 54% of the 3.14 kJ originally stored in the capacitor. This shows that while the plasma energy is normally described in the literature by the stored electrical energy, the energy deposited into the plasma is substantially smaller. In this setup, 87% of the energy is deposited during the first oscillation of the current, which indicates that most of the plasma is produced during the first 250 μs .

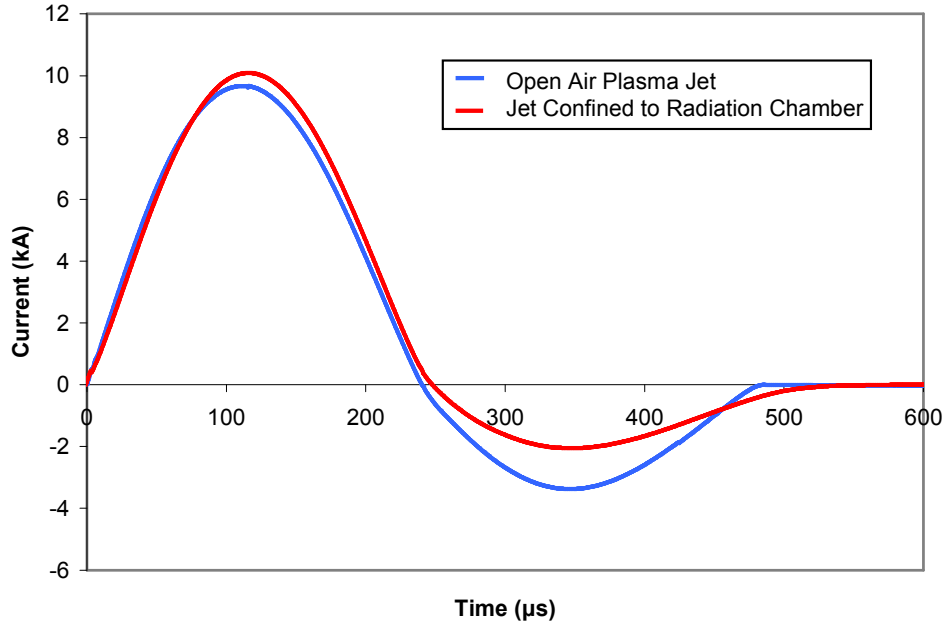


Figure 5.1: Capillary current during the plasma discharge for two different setups.

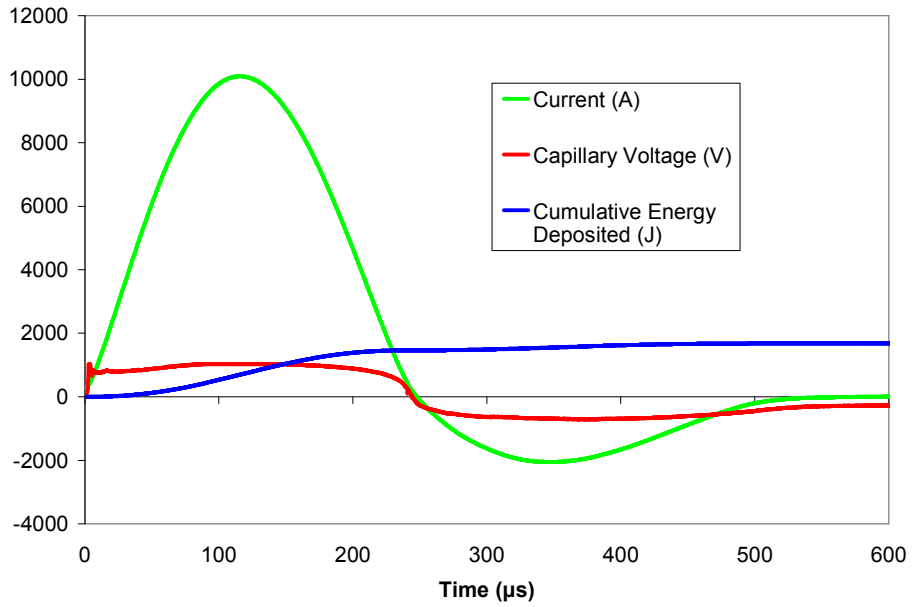


Figure 5.2: Current, capillary voltage, and plasma energy deposition during the capacitor discharge with the radiation chamber setup.

HEAT FLUX MEASUREMENTS

Figure 5.3 shows the radiative flux recorded by the heat-flux sensor along the axis of the plasma jet exhausting into room air. The measurements were made as a function of sensor standoff distance. The closest distance shown is 4.67 cm from the jet exit. No useful data could be collected when the sensor was closer to the jet exit because of electromagnetic interference from either the plasma discharge or the current through the plasma firing assembly. This interference can be seen until 250 μ s in the run at a standoff distance of 4.67 cm. A defined Mach disk does not reach much further than 5 cm during the discharge. A pseudo time-series of visible emission images of an open air plasma jet produced with the same discharge circuit used in the present study (Kohel et al. 1999) shows this. As a result, the measured heat flux time histories do not reflect an underexpanded supersonic jet structure. The recorded fluxes tend to peak at about 300 μ s in all cases, although this may be due to the 300 μ s response time of the sensor. The flux decreases as the distance from the jet exit increases. Two peaks can be seen in the runs at 12.3 cm and 14.8 cm. A firing was also conducted with the sensor at a standoff distance of 9.75 cm and with a viewing angle of 30° off the jet centerline. The heat flux measured in this case is less than half the measured heat flux at 9.75 cm while looking directly down the bore of the capillary. The probable explanation is that a large portion of the radiative heat flux measured on-axis is from the inside of the capillary and not the expanding plasma. The dense plasma inside the capillary bore is close to a blackbody radiator and is at a higher temperature than the expanding, optically thin plasma outside the jet exit. The first peak seen in the runs with a much larger standoff distance might be from the capillary bore and the second peak might be from the plasma reaching the sensor.

With the fused silica flat removed for the total flux measurements significant electromagnetic interference was observed at a greater distance from the jet exit. As a result the conductive and convective heat flux traces could only be calculated at the largest standoff distances. Even in these cases the early portions of the time history are unreadable. These traces are shown in Fig. 5.4. Once again the heat flux decreases as standoff distance increases. This graph shows that when the plasma is able to impinge upon the sensor, the electromagnetic interference lasts until 500 μs , double the time for the radiative flux measurements. This suggests that there is interference directly from the plasma.

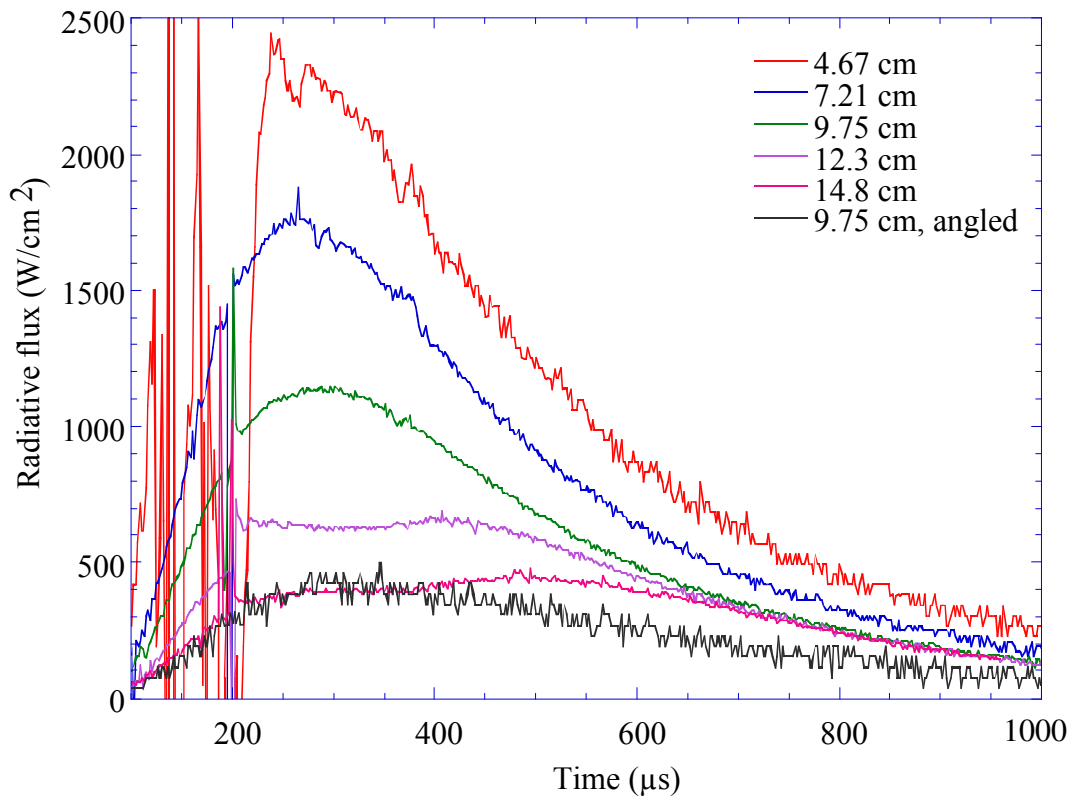


Figure 5.3: Time-dependent radiative heat flux measurements at several axial locations.

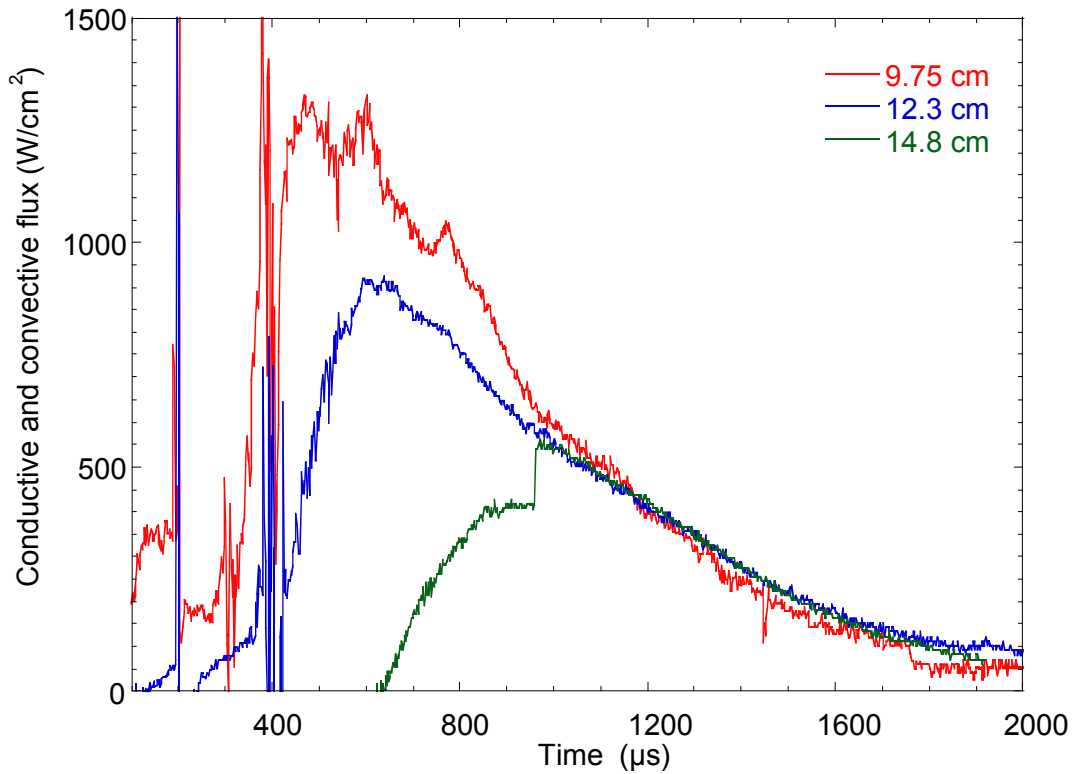


Figure 5.4: Time dependent conductive and convective heat flux calculated from radiative and total heat flux.

Figure 5.5 shows the values of the peak heat flux for each location along the axis of the jet for both radiative and conductive/convective (cc) flux cases. The time taken to reach the peak heat flux at each location is also included on the figure. As mentioned above, peak radiative and cc heat flux both decrease as standoff distance increases along the jet axis. This can be explained by the fact that the plasma expansion increases with distance downstream, Additionally, the solid angle subtended by the capillary exit decreases with downstream distance. Generally, the time to peak heating also increases with axial distance. This trend is valid even though the delays measured are skewed by the long response time of the sensor. Peak conductive and convective flux is greater than radiative flux at the axial distances tested, but they are of the same order of magnitude. At

9.75 cm the peak conductive and convective flux is three times greater than the peak radiative flux taken off axis. This shows that radiative energy transfer could have a significant effect on propellant ignition. The observed time of peak conductive and convective heat flux is larger than the observed time for peak radiative flux. This reflects the fact that plasma radiation reaches the sensor much quicker than the plasma. The peak flux values measured here are in the range of a few kW/cm². This is comparable to the values Williams and White (2001) and Das et al. (2005) obtained in their heat flux measurements.

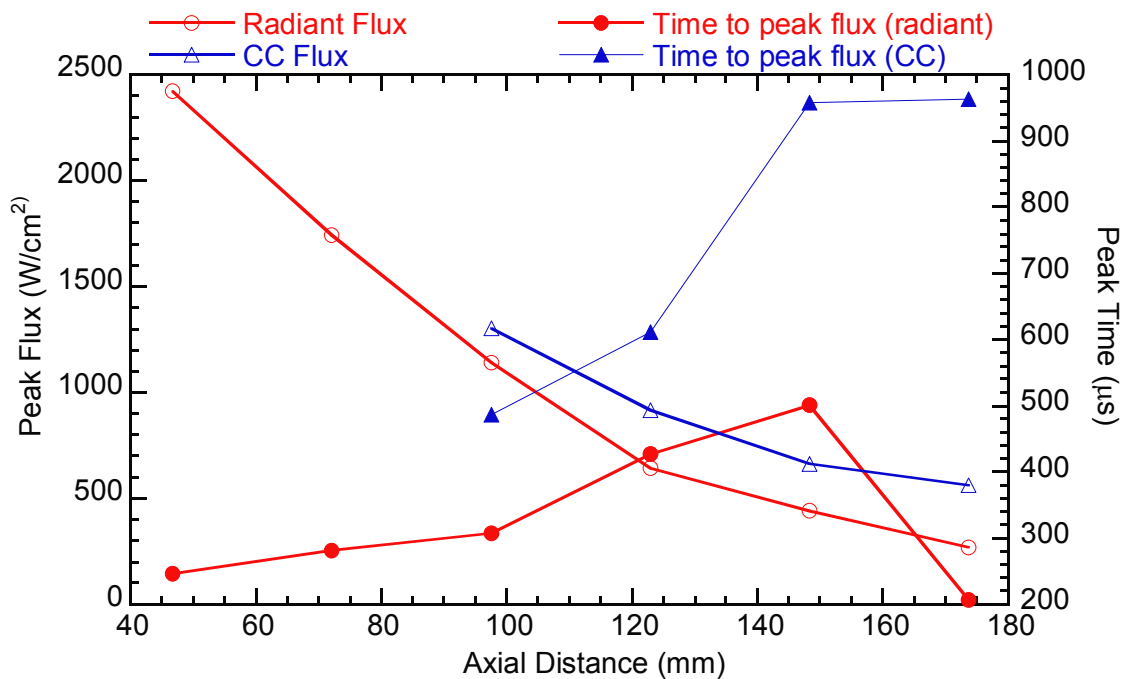


Figure 5.5: Values of peak heat fluxes and time delay of heat fluxes with respect to downstream distance.

PLASMA RADIATION

Figure 5.6 shows the plasma radiation intensity measured by a fast response photodiode. The photodiode was placed 11.4 cm above the plasma chamber window, with a neutral density filter (OD 2) attenuating the plasma light. The intensity ramps up rapidly and peaks at about 80 μs . The radiation then steadily decreases until between 600-650 μs , when the capacitor stops discharging. The intensity decays exponentially from 600 μs to 1500 μs . The dip in intensity around 300 μs is probably a result of the capillary voltage switching polarity as the capacitor current oscillates. After the firing the acrylic window guard is always somewhat blackened and the surface looks like it was partially melted from the plasma. The fused silica mask always has much more deposition on the surface than the acrylic mask and is opaque after firing. The acrylic mask is transparent after the firing. Greater ablation from the acrylic surface might explain the difference in the two surfaces after firing. The steady intensity decay during the discharge might be explained by the effect of the plasma on the mask. No direct measurements of heat flux to the propellant surface were made, but for an order of magnitude estimate it can be assumed the confined plasma produces fluxes equal to or higher than the same plasma expanding into open air. A measurement was made of the peak radiative flux on a probe 4.67 cm from the jet exit of a plasma expanding into room air to be 2500 W/cm^2 and the flux was above 1000 W/cm^2 for the entire capacitor discharge.

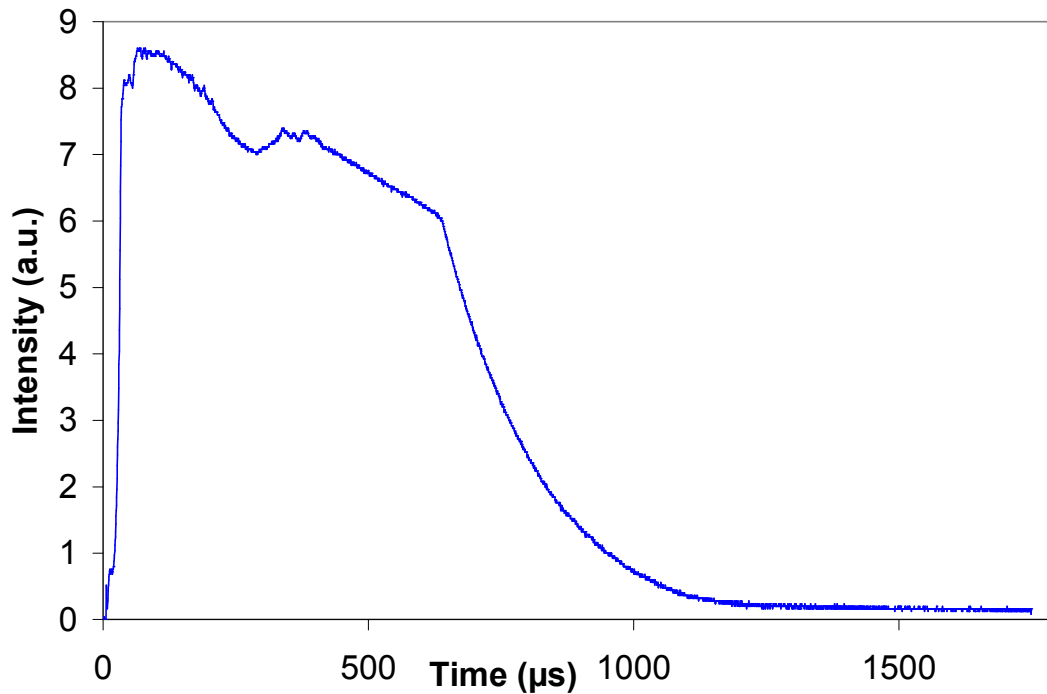
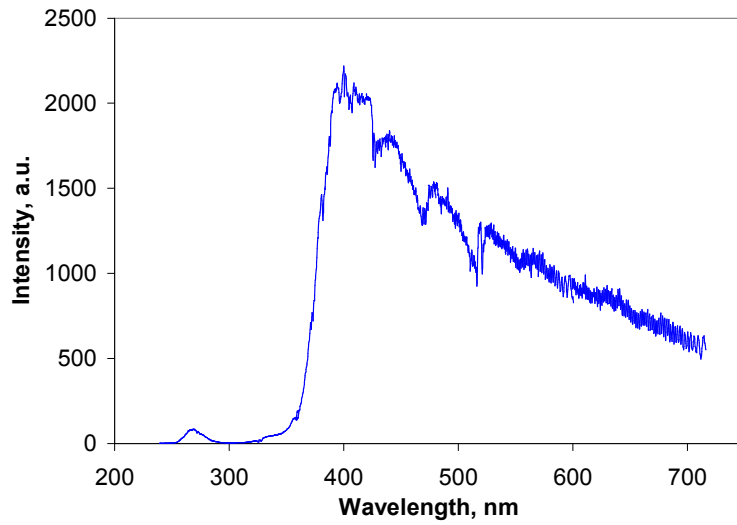
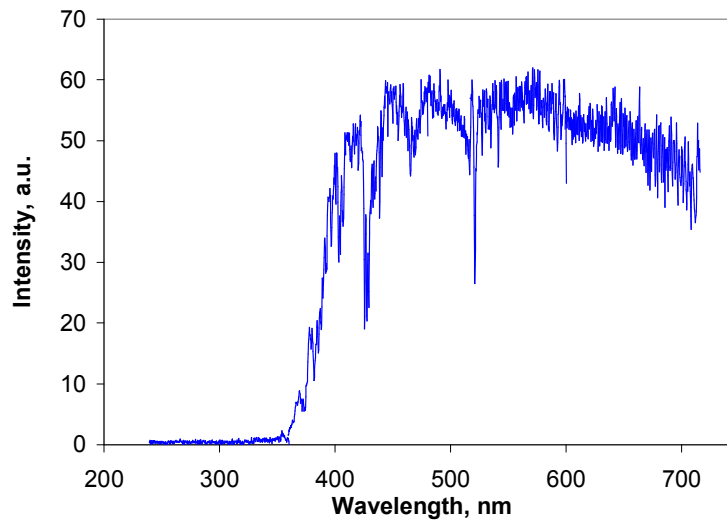


Figure 5.6: Plasma radiation intensity measured by a fast response photodiode

Plasma spectra combined from a number of firings with the acrylic mask can be seen in Fig. 5.7. The spectral range of the spectrometer is 120 nm so each curve is a combination of four acquisitions at the same delay. Curves were produced for 150 μs and 500 μs delays. At both delays the spectrum is characterized by broadband emission with a few noticeable absorption lines or bands at 428, 470 and 520 nm. This is characteristic of a confined electrothermal plasma discharge. The cutoff below 380 nm is due to attenuation by acrylic. The oscillations on the right side of both curves are due to interference fringes on the detector. The integrated emission intensity at 500 μs is much less than that at 150 μs and the spectra change over time. The reduction in intensity is probably a combination of lower energy in the plasma and higher attenuation through the



a)



b)

Figure 5.7: Plasma emission spectra at a) 150 μ s b) 500 μ s

mask as the surface is degraded. At 150 μ s there is a marked peak at 400 nm. Because the acrylic cuts off at 380 nm, it is impossible to know where the true plasma radiation peak is and the peak is probably at a lower wavelength than observed. At 500 μ s the peak

shifted to between 500-600 nm. This indicates a reduction in temperature of the plasma between 150 to 500 μ s.

Before these radiation experiments began there was some question as to how much the plasma radiation would affect the propellant, and also how similar the effects would be to results from other studies that focus on interactions of plasma with graphite free JA2 propellant (Beyer and Pesce-Rodriguez 2004, Koleczko et al. 2001). Most tests involving plasma propellant interactions involve higher plasma energies than the 3.1 kJ of the current plasma. In addition, graphite free JA2 transmits more radiation in depth than the propellant used in these experiments. Figure 5.8 shows propellant discs before and after exposure to plasma radiation and an open air plasma jet. The level of interaction from plasma radiation, while not as great as that from an open air plasma jet, and far from ignition, is enough to have clear visible effects on the surface of the JA2 disc.

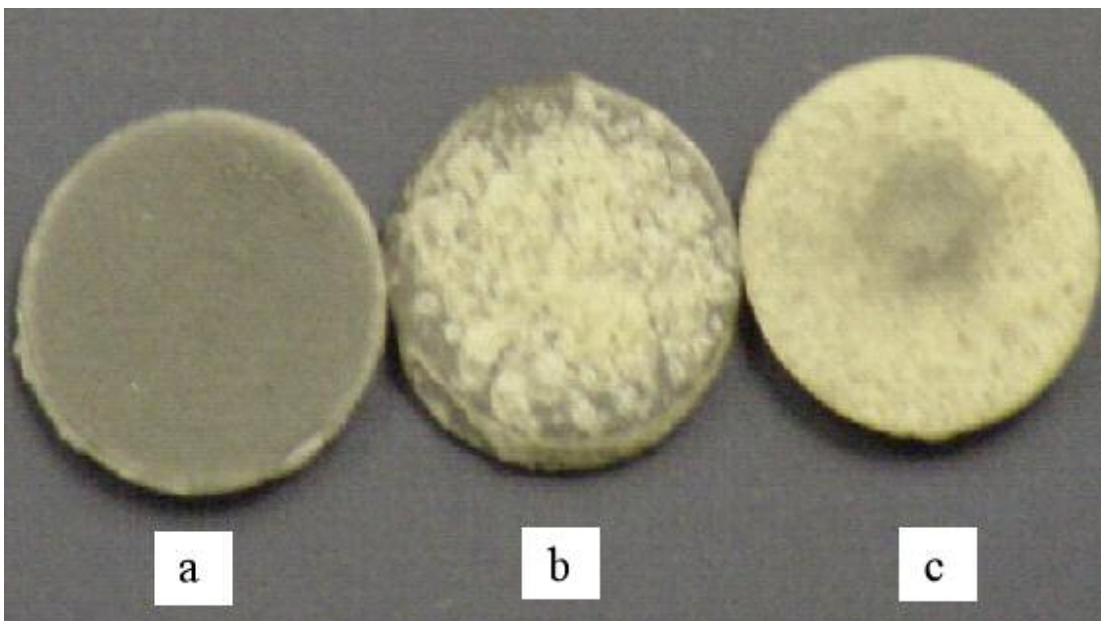


Figure 5.8: JA2 disc surface a) before, b) after plasma radiation exposure, and c) after open air plasma jet impingement

The structures produced on the propellant surface from plasma radiation exposure can be better seen in the higher resolution monochrome image shown in Fig. 5.9. These structures are caused by decomposition reactions taking place in the propellant as a result of plasma radiation. The brighter regions correspond to blisters and in-depth voids formed in the semi-transparent JA2 after exposure to plasma radiation. Kappen and Beyer (2003) published surface images as well as cross sectional images of transparent JA2 after exposure to plasma radiation. Kappen and Beyer's images showed in depth voids in

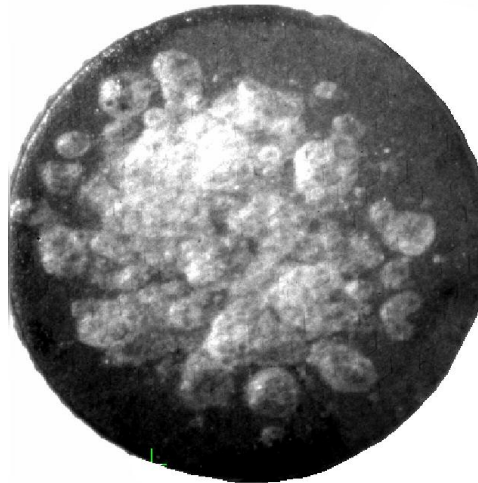


Figure 5.9: Semi-transparent JA2 propellant surface after exposure to plasma radiation during current study.

the propellant material that corresponded to the circular structures seen on the surface images. This is the reason these structures are termed “blisters.” The range of sizes of the structures observed on transparent and semi-transparent propellant are very similar. There is smaller structure in individual blisters on the semi-transparent JA2, while this is not observed in the transparent JA2. The major structures seen at the propellant surface are

discrete objects, circular in shape, with a maximum diameter between 1-2 mm. In semi-transparent JA2 used in the current study they were observed to a depth less than 0.5 mm, while in transparent JA2 they were observed throughout the propellant sample (Kappen and Beyer 2003). The similar size and shape of the structures in transparent and semi-transparent JA2 implies that decomposition from graphite heating is probably not a major cause for the surface changes observed.

NITRIC OXIDE PLIF

An example NO PLIF image is shown with a diagram of the experimental geometry in Fig. 5.10. The brightest swath at the top of the image is propellant luminosity/radiation scattering. Radiation from the plasma travels from bottom to top. The laser propagates from left to right across the image. The entire propellant disk is seen in the camera's field of view. A series of example NO PLIF images, one taken from each delay sampled (out of 3 images per delay), can be seen in Fig. 5.11. They are arranged such that a representative time history is shown. Each image is false colored from grayscale and has been rescaled individually in order to better visualize the NO. Many of the images show scattering off large particles as well as bright structures related to the disc edge in addition to the structures containing NO below the center of the propellant. To distinguish between NO fluorescence and scattering, a few images were taken with the pump laser tuned slightly off resonance. An example image at 500 μ s delay can be seen in Fig. 5.12. This image's intensity was scaled such that signal of the same intensity as the minimum brightness structures in the NO PLIF images would clearly be visible. The large particles can still be seen in Fig. 5.12 as well as some possible scattering very close to the propellant surface. However, the large structures away from the propellant surface and at the edge are observed only when the laser is tuned on resonance.

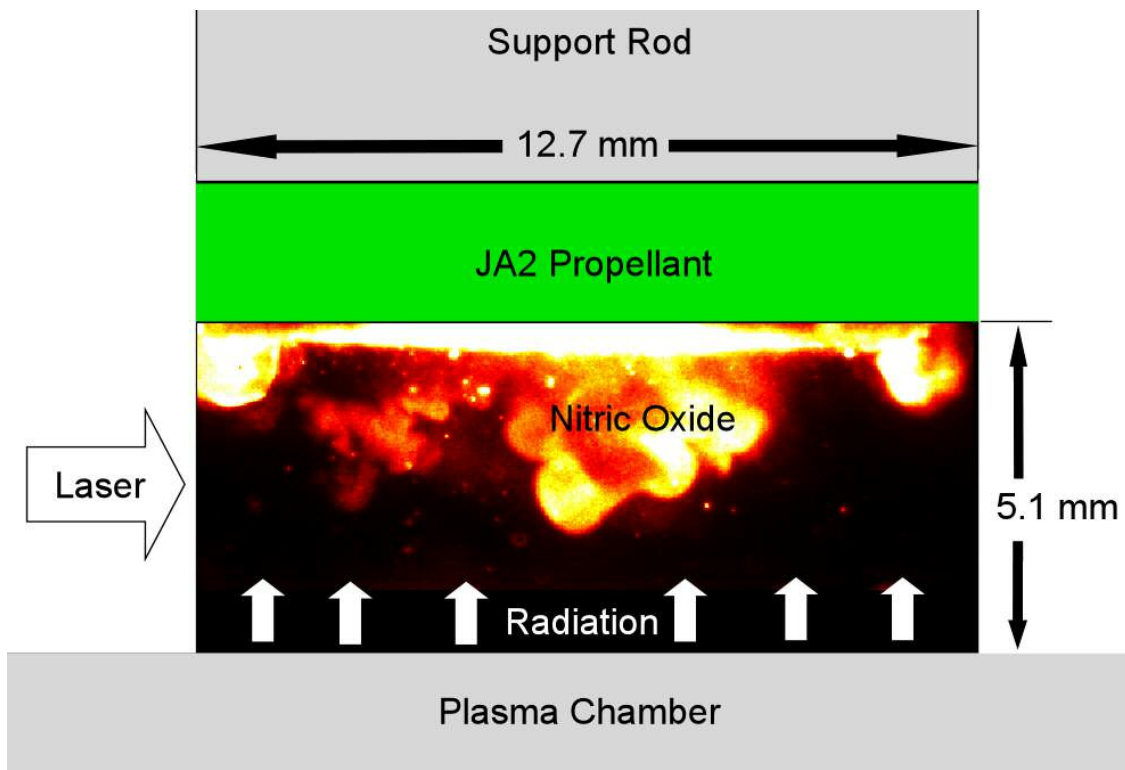


Figure 5.10: Geometry for camera field of view in NO PLIF and YAG PLMS experiments.

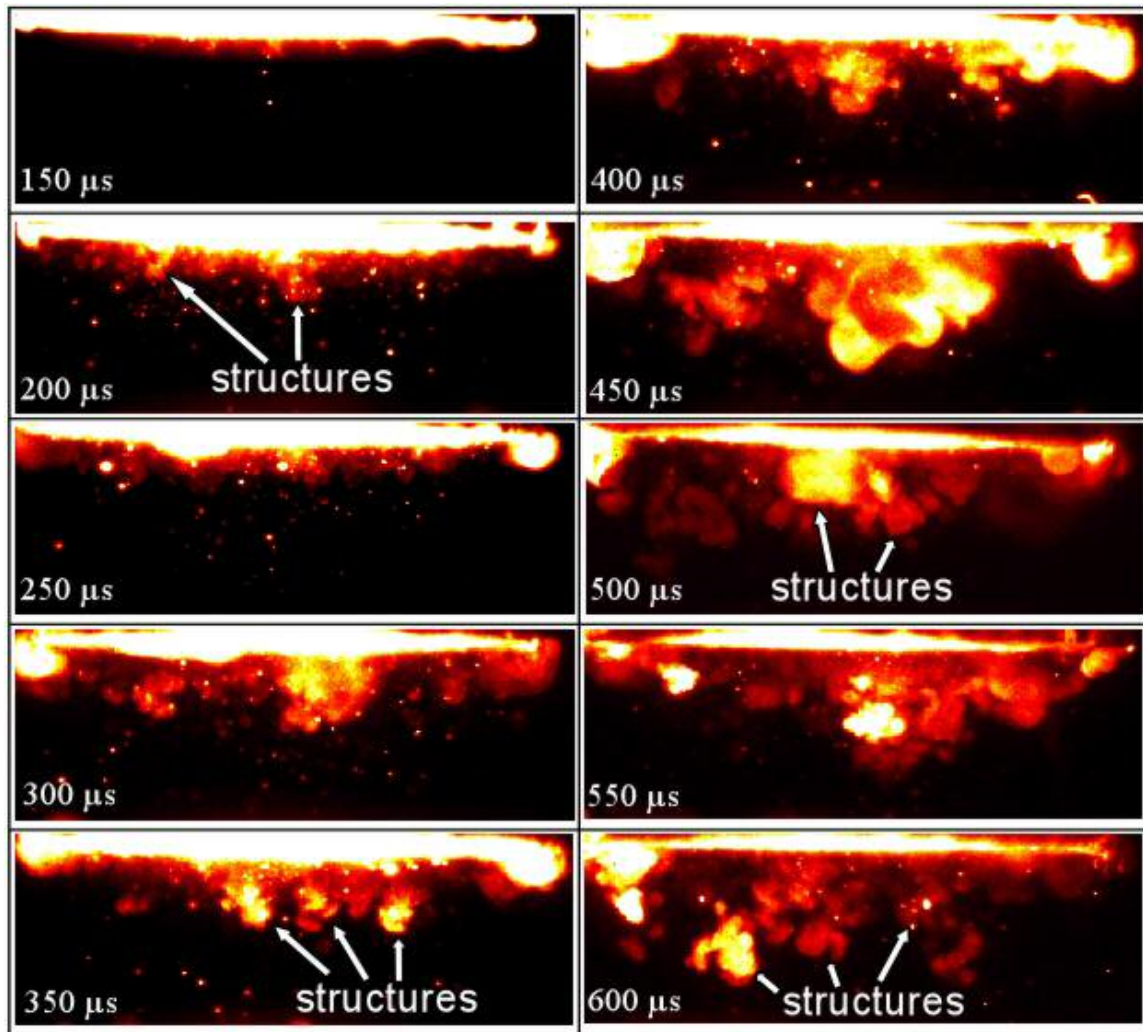


Figure 5.11: Time sequence of NO PLIF images created from separate firings. NO ejection structures are labeled.

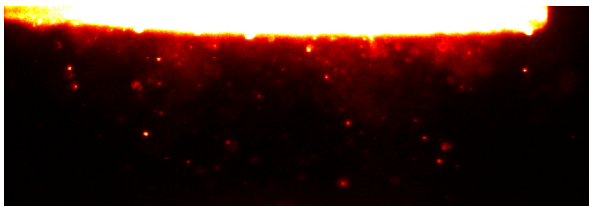


Figure 5.12: Example image of tuning NO pump laser off absorption line at 500 μs delay.

NO signal is not observed until after 100 μs in Fig. 5.11. At 150 μs small globular structures appear and grow as the discharge progresses. These are labeled in Fig. 5.11. In many of the images, especially at times after 350 μs , discrete nitric oxide structures can be seen separate from the propellant surface. This suggests that NO is being produced in short bursts rather than continuous jets during the discharge. An alternative explanation is that the clouds of NO propagate parallel to the surface of the propellant. However, very few structures in the images have a cross section consistent with NO moving sideways, so this is not as likely. From the unprocessed images it can be inferred that the brightest NO signal is present when the clouds first appear at 150 μs , and the signal gradually decreases until 300 μs where it stays relatively constant. The temperatures of the propellant surface and the gases being released by the propellant during the interaction were not measured. Simulated spectra suggest that the NO signal should increase with decreasing temperature. It is reasonable to assume that the gases ejected from the propellant are at temperatures equal to or greater than the surrounding air as a result of the energy deposition by the plasma radiation. If the temperature of the gases produced was greater than the ambient air, the temperature would decrease as the gases propagated away from the propellant and mixed with ambient air. Nitric Oxide does not absorb in the visible range and so plasma light would not affect it. The resulting NO PLIF signal would increase from this temperature decrease. Because the signal is observed to decrease as the NO structures propagate away from the propellant, the other main driver of fluorescence signal, species number density, must be the cause. This matches expectations of the NO structures mixing with and diffusing into the ambient air.

The velocity of the NO structures was roughly estimated by measuring the average rate of change of the distance from the bottom edge of the NO structures to the propellant surface. The order of magnitude of the velocity calculated is 10 m/s. It is

unclear whether the source of this ejected material is the outer surface or pockets of decomposition directly underneath the surface. The pressure difference needed for isentropic expansion in air to cause this velocity is a small fraction of atmospheric pressure. While double base propellant decomposition can be pressure dependent due to autocatalysis from NO_2 (Kimura 1988), pressure differences in these experiments are probably small enough that they do not affect decomposition rate, which would affect burn rate in a gun firing.

LASER MIE SCATTERING

Figure 5.13 shows laser scattering images taken with the pulsed double Nd:YAG of particles emitted from the propellant. These were individually rescaled from grayscale images. A representative time history similar to Fig. 5.11 gives an idea of the type of scattering structures and how they propagate during the discharge. Once again the structures begin to appear at 150 μs and grow larger and propagate down as the discharge progresses. There are two distinct types of scattering structures observed. The first, composed of a range of particle sizes, appear and grow as the large majority of NO clouds do in Fig. 5.11. This is labeled “A” in the 450 μs image of Fig. 5.11. The shapes are similar enough that they probably are the same type of structures, visualized two different ways. The second type of structure, seen only in the 400 and 450 μs images away from the propellant, but also throughout the images at the propellant edges, is characterized by much brighter scattering, larger size, and homogeneity of the particle sizes, inferred from the relatively constant signal throughout the structure. This is labeled “B” in the 450 μs image of Fig. 5.11. This structure type is much rarer, as it was only seen away from the propellant surface on those two images in 25 runs. However, the surface of the propellant after these two runs looked no different to the naked eye than after any other run. A corresponding NO structure might be seen in the 450 μs image of

Fig. 5.11. The large NO structure in the center of that image is brighter than the surrounding structures, bigger, and has a much smoother surface. In addition, similar bright structures can be seen at the edges of the propellant in Fig. 5.11.

The two different structures observed can be seen side by side in the 450 μs image of Fig. 5.13. That image is scaled differently from the majority of images in the figure. The smaller structure, with the same brightness as the other blotchy structures in the other images, has intensity counts ranging from 5,000 to 20,000 while the larger structure has a brightness similar to the material coming off the edge of the propellant and saturates the detector with 65,535 counts at its brightest. The brighter structures correspond to an ejection where more material is produced. This is supported by the larger scattering signal and size of these structures. They might appear at the edges of the propellant because the grains are exposed there. During these radiation interactions it has been observed that the blisters form along the propellant grain. In sheet JA2 propellant, the grain is parallel to the surface. Blisters that would normally be forming underneath the surface are exposed to open air there and so would be better able to discharge material. In the 450 μs image of Fig. 5.13 a structure similar to a mushroom-like vortex ring can be seen at the bottom. This might correspond to a stronger than normal jet of material coming from the propellant surface.

The images show a large number of particles separating from the propellant surface during the radiation interaction. The particles have a range of sizes. The smallest particles, especially in the large bright structures, are unresolved, while the largest are around 6 \times 6 pixels, corresponding to a diameter of 156 μm (individual pixels correspond to an area 26 by 26 μm). JA2 propellant has three major nitrate esters, two of which, nitroglycerin (NG) and diethylene glycol dinitrate (DEGDN), are liquid at room temperature. JA2 also has many other components at low concentration so it is

impossible to know the composition of the particles in the images shown. They could be chunks of nitrocellulose (NC) fiber, liquid mists of NG or DEGDN, an agglomeration of NC, NG, and DEGDN, or some smaller decomposition product that scatters light. The large jump in pressurization seen in closed bomb plasma ignition tests (Lieb et al. 2001) during the plasma discharge might be due in part to the increased burning surface area provided by these particles, in addition to the known outgassing that occurs. No film or buildup of particulates was ever observed on the top of the chamber. In addition, a scale with a 0.002 g resolution could detect no difference in the mass of the propellant disks before and after radiation exposure. Propellant disks normally had a mass around 0.5 g, and thus only less than 0.4% of the semi-transparent JA2 propellant mass is lost during this interaction with plasma radiation.

The structures observed jetting from the propellant could directly correspond to formation of individual blisters on the propellant surface. Blisters overlap on the propellant surface so in order to create clear individual jets they would probably need to form at different times.

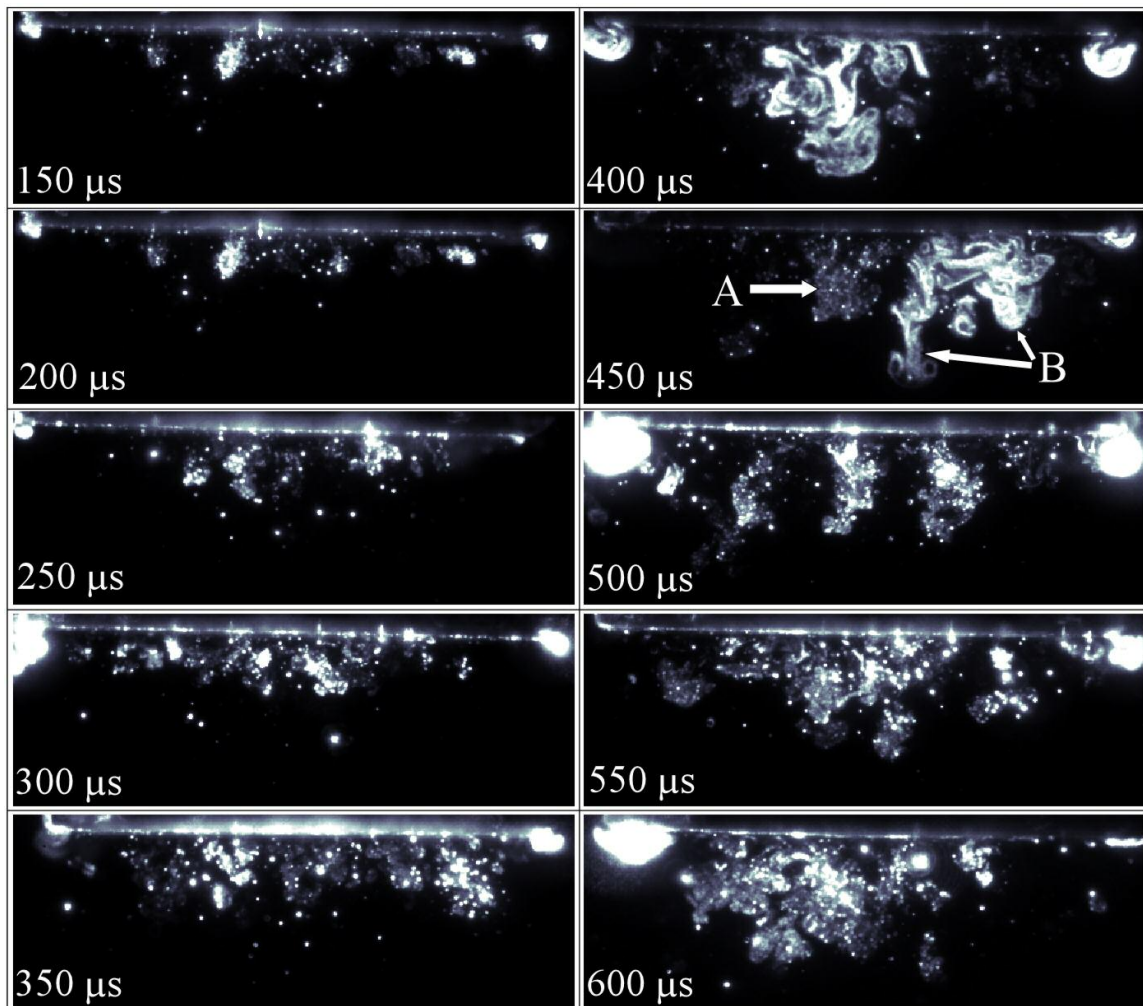


Figure 5.13: Time sequence of laser scattering composed of images from individual runs. Labels A and B mark smaller more common scattering structures and larger, brighter, less common scattering structures respectively.

SIMULTANEOUS TWO CAMERA IMAGING

Figure 5.14 shows a representative series of images of the propellant surface from a single run using an acrylic mask on the window. The framing rate of the camera was 50 kHz and the illumination source was the same plasma light that caused the decomposition. While the images were taken every 20 μs, they are displayed at intervals of 60 μs to conserve space. For better viewing these images have been processed by a

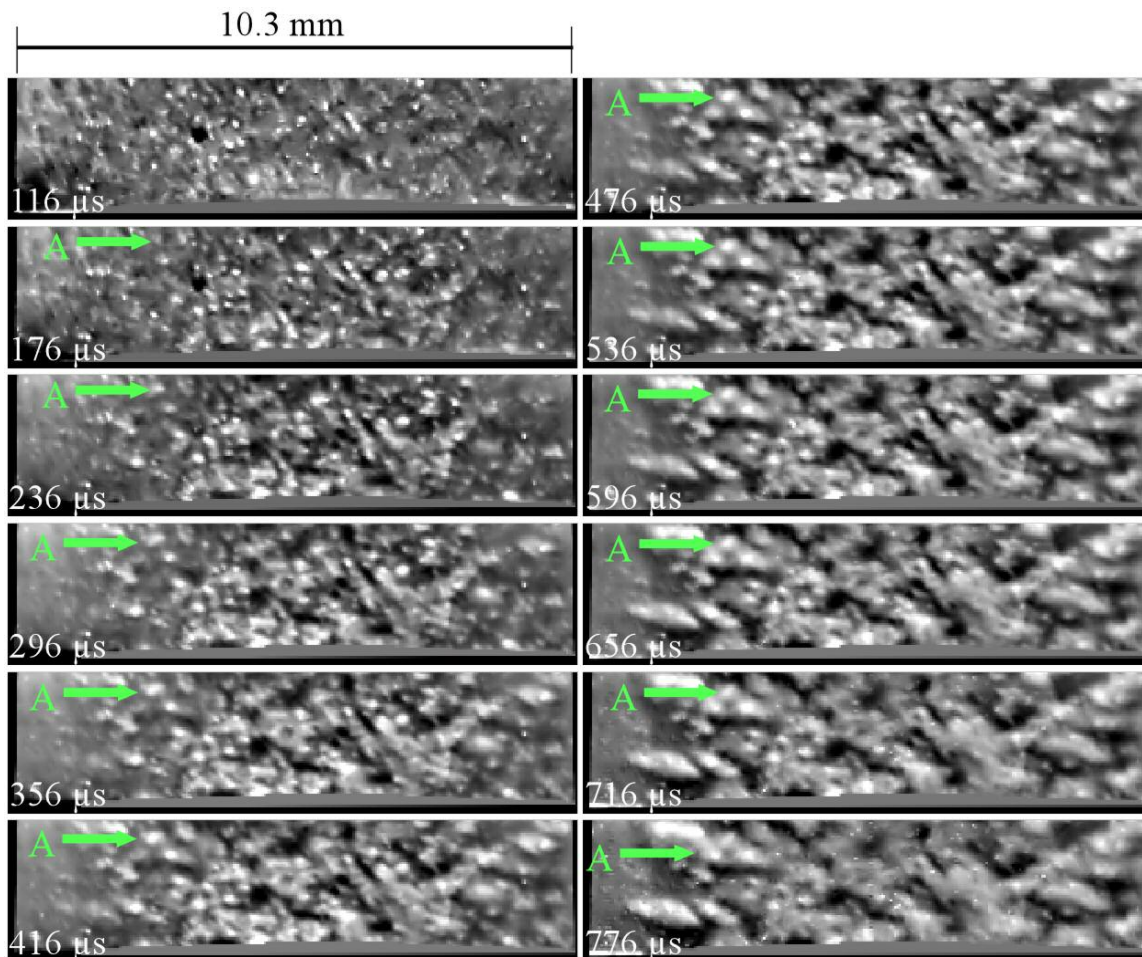


Figure 5.14: Time series of propellant surface during the plasma discharge during 2 camera experiment. Delay times from the capacitor trigger are marked in the bottom left corner of each image. The label A marks a structure as it changes throughout the plasma discharge.

variety of methods using Matlab. All linear filtering was accomplished by modifying the two dimensional Fourier transforms of each image. These images have had their DC component filtered out to account for the change of the plasma brightness over time. Also, their low frequency components have been filtered out to account for spatial variations in the lighting. These spatial variations imply that the confined plasma has

spatial structure inside the chamber. Camera fixed pattern noise has been filtered out as well. A code (Kovesi 1999) was run to reduce the readout noise and improve visualization of the affected areas of the propellant. Otherwise the images at the end of the sequence would be very difficult to see because the illuminating plasma light is reduced at that time. The images have been transformed using the camera registration technique described in Chapter 4 to show the propellant surface as if viewed directly from below. Further, the images were intensity scaled so that the brightest 1% appeared white and the darkest 1% appeared black. A section on the bottom of each image was deleted because it was completely saturated over most of the run. This was a result of bleeding from oversaturated pixels that imaged the plasma chamber window beyond the edge of the mirror.

In general, the brighter regions of the images are the areas that have been affected by the plasma radiation. This is reasonable since the blisters seen by the naked eye are white while the unaffected surface is dark green. Visible propellant scattering spectra displayed earlier show that the blister reflectance is much higher than that of the pristine surface. However, at the beginning of the sequence preexisting blemishes on the surface appear as bright spots. Most of these blemishes diminish and disappear as the propellant begins to change. Some coincide with spots where blisters begin to form on the surface.

The propellant surface begins to change at about 116 μs , which is the first image in the sequence. This coincides with the ICCD camera experiments where material began ejecting from the propellant between 100 and 150 μs . The surface changes throughout the plasma discharge, and continues to change afterwards albeit at a much lower rate. During the discharge, changes in the surface are visible between consecutive images 20 μs apart. Irregularly shaped small structures are observed to appear and grow through random expansion at their edges and merge with other growing structures. An example of this is

labeled “A” in Fig. 5.14. Blisters might not be the correct term to describe these structures because there is no obvious evidence of gas forming beneath the surface. These structures might just be discoloration of the top layer of propellant as it decomposes. Also, they are smaller than the 1 mm diameter circular blisters seen in Fig. 5.9, as well as irregular in shape. The surface changes earlier and more quickly at the center of the image, which is closer to the center of the propellant disk, and then later nearer the edges. This is expected because the irradiation at the propellant disk decreases with increasing distance away from the center. Most structures start off very small, with a characteristic size in the range of 0.1 mm, and by 776 μs grow to a size around 0.5 mm. Most large structures at the end of the firing are an agglomeration of smaller ones. They are not isolated but connected to the other large structures, and show considerable variation scattering intensity over their area, evidence of their formation history. A structure the size of the large blisters in Fig. 5.9 was never observed in any of the runs by the propellant surface camera. It will be shown later that the propellant continues to change well after the capacitor is finished discharging and that the larger blisters observed after the firing might be a result of this.

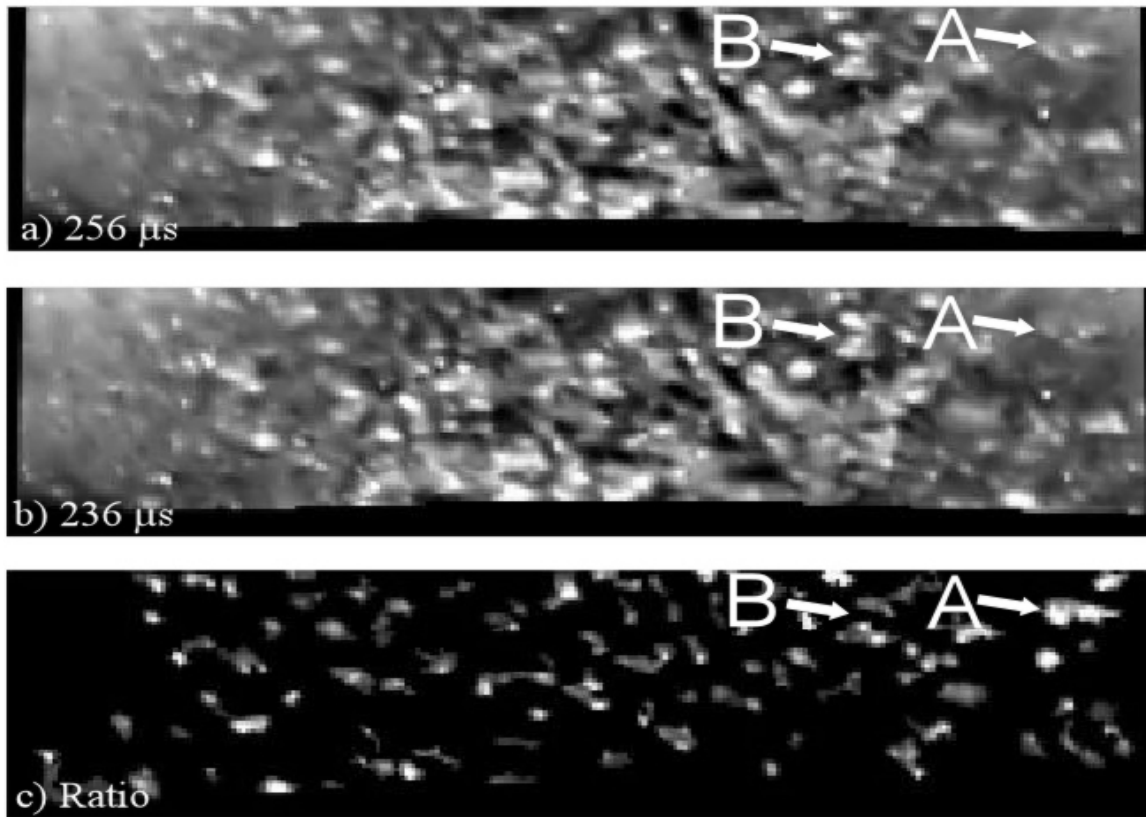


Figure 5.15: Example of difference image, with the two images used to calculate it.

An example of the propellant surface image ratio technique is shown in Fig. 5.15. The ratio image has many small blobs of varied shape and size. These regions of change support the conclusion that the structures seen on the propellant surface grow randomly by small amounts between consecutive images during the plasma discharge. Although there are regions of change that encompass all of a smaller decomposition structure (labeled “A” in Fig. 5.15), in general these ratio regions comprise a small part of an existing structure or are on some portion of the edge of an existing structure (labeled “B” in Fig. 5.15).

Statistics on these regions can be compiled by applying this ratio method to multiple runs. The ratio images are converted to binary images and the regions of change are defined as regions of pixels that are 4-connected, meaning neighboring pixels to the left, right, top and bottom that are above the threshold are part of the same region. Diagonally connected pixels are not necessarily part of the same region. Data such as the number of regions, total area covered, and median size can be computed. The data are averaged over three runs for each mask, and a 95% confidence interval is computed using a student's t distribution estimation. These data show some interesting trends.

Figure 5.16 shows the average intensity per pixel of unprocessed propellant surface images over the course of several runs using both acrylic and fused silica window masks. This shows the timing for the plasma illumination. While there is some variation, on the whole it resembles the radiation intensity history of Fig. 5.6. The intensities with both masks are expected to be the same because the camera filters block the UV light. The maximum illumination is reached shortly after 100 μs . There is a local minimum at about 300 μs when the current oscillates in the discharge circuit, and a secondary maximum is reached at about 400 μs , after which the signal tapers off.

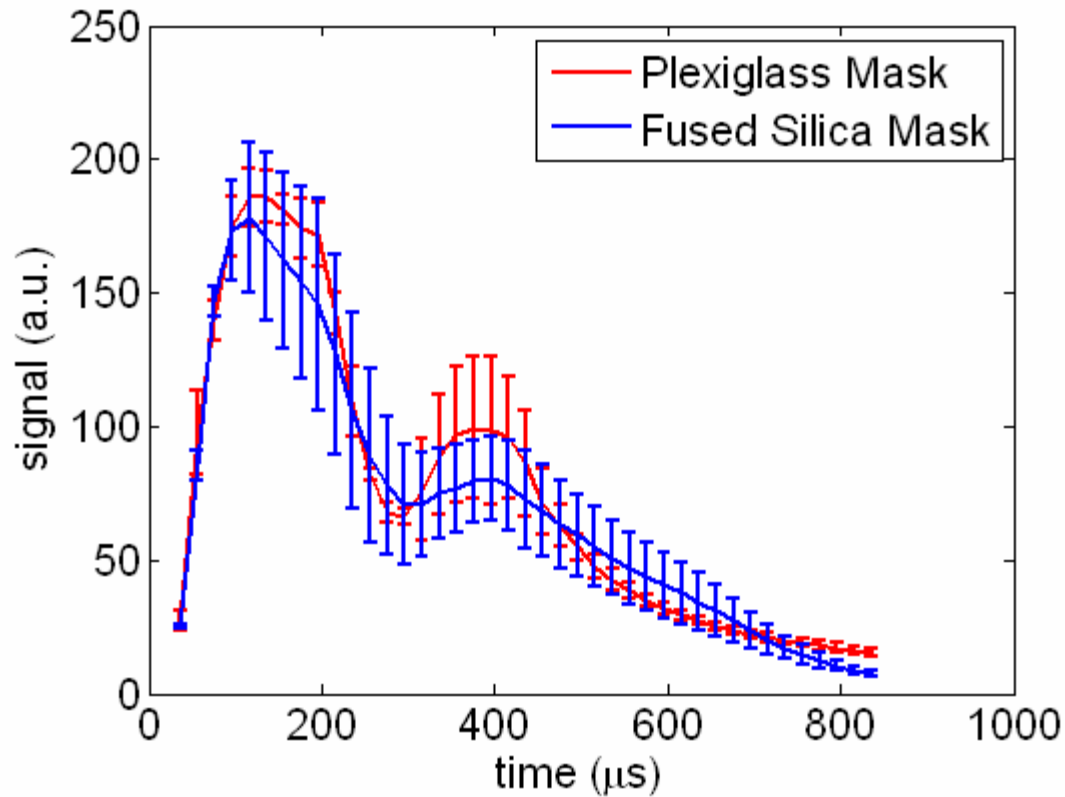


Figure 5.16: Average intensity of propellant surface image using each window mask.

Figure 5.17 shows the number of regions of change over the course of several runs. There is no major noticeable difference between the runs using a fused silica mask and an acrylic mask. Also, the number of regions peaks shortly after 200 μs. This is 100 μs after the peak of illumination from the plasma. After the peak the number of regions steadily declines until 600 μs at which point the number of regions increases slightly or stays constant. The data after 600 μs are unreliable because the signal to noise ratio of the propellant images is very low at this point. In addition, as mentioned before, the data before 100 μs are also suspect because of the very rapid changes in illumination over that short time period. The number of regions of change begins at a finite value and then

decreases until 100 μs . This data has been ignored. Viewing the propellant surface images by eye shows that this is not actually happening.

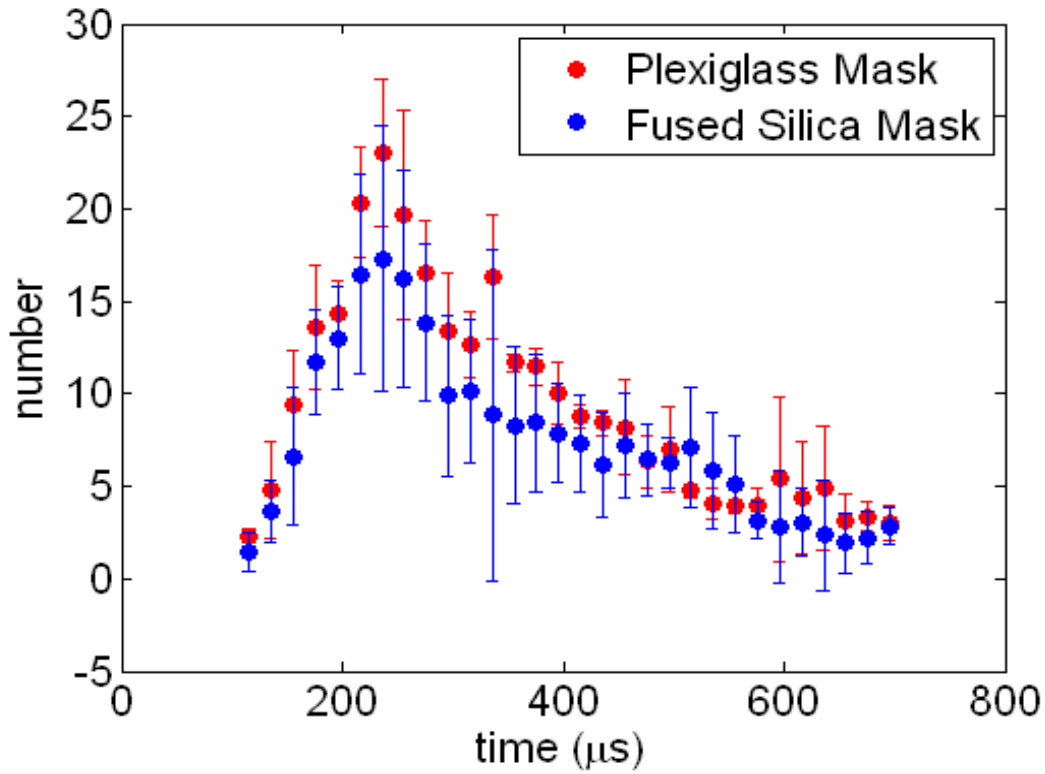


Figure 5.17: Average number of regions of change appearing over multiple runs.

Figures 5.18 shows the percent of total area of each ratio image covered by regions of change. The data were generated by summing the area covered by all regions of change and comparing it to the size of the image. Figure 5.19 shows the median size in pixels of the regions of change. Both figures show data for the same runs shown in Fig 5.17. Median region size was chosen instead of average region size to avoid the skewing of data due to the presence of artificially large regions of change at the edge of the image as previously mentioned. While these graphs display different statistics, they show the same trends as Fig. 5.17. Both total area and median area of regions of change reach a

peak at about 200 μs , although the large variation between individual runs in Fig. 5.19 causes the confidence interval to be large. On the whole, both total area and median area show gradual declines after the initial peaks. The analysis results are unreliable before 100 μs and after 600 μs as explained earlier.

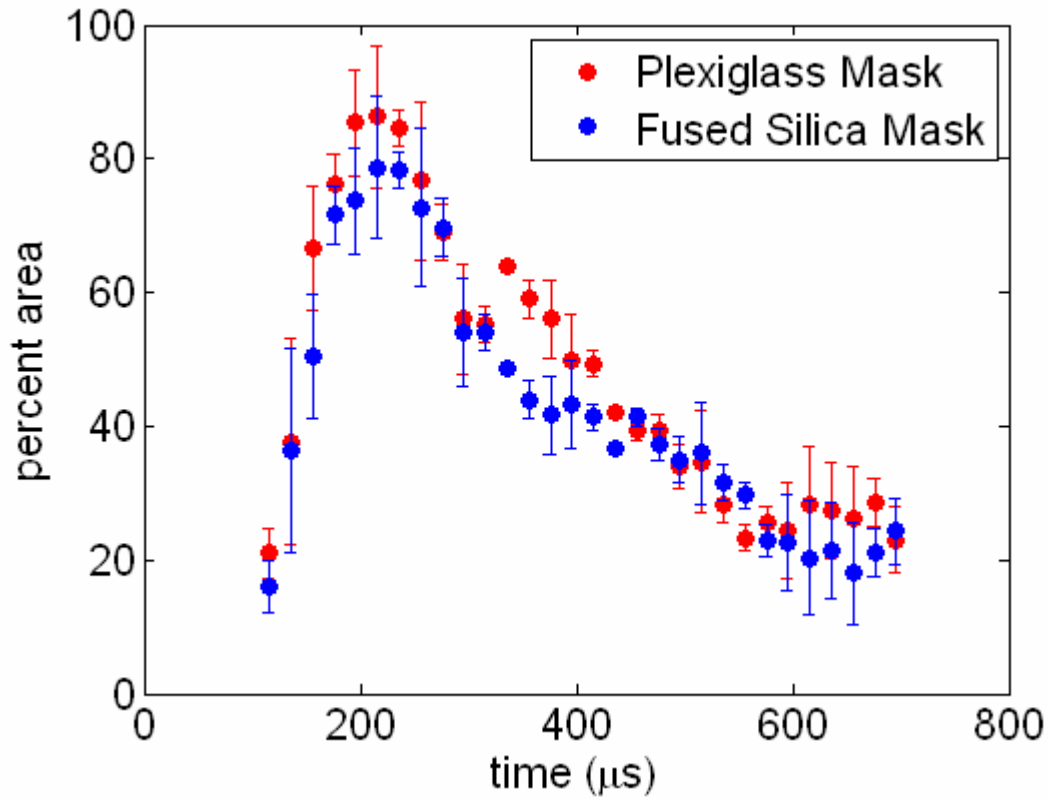


Figure 5.18: Average percent of total image area covered by regions of change for each mask.

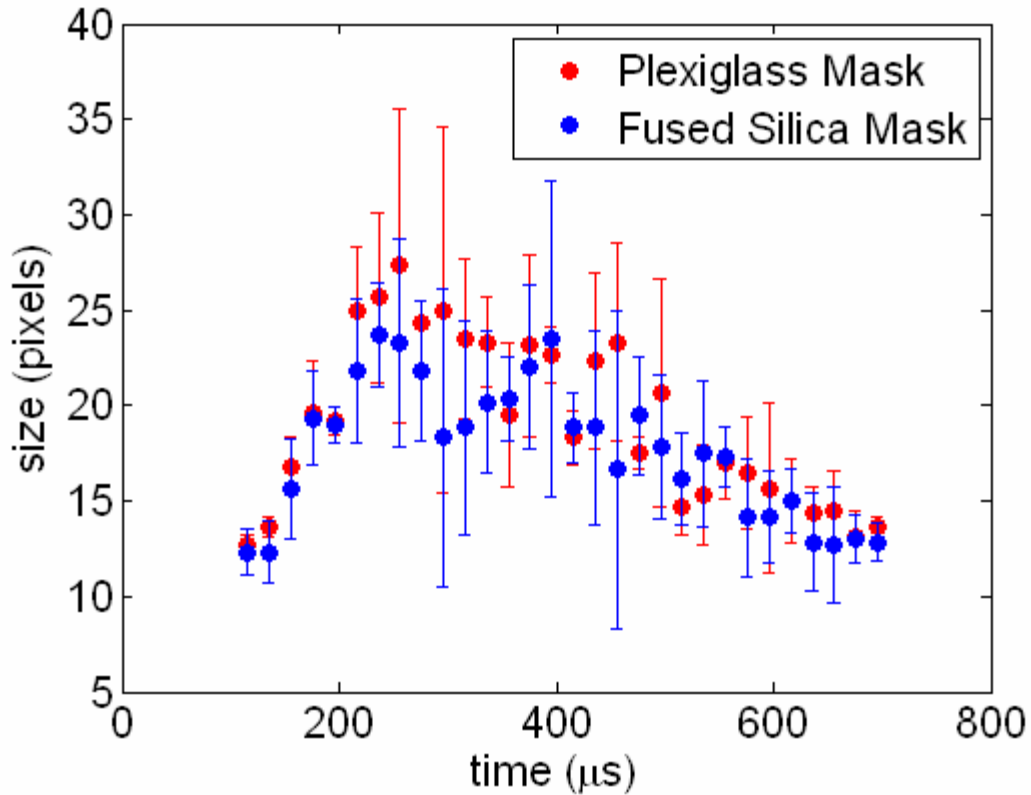
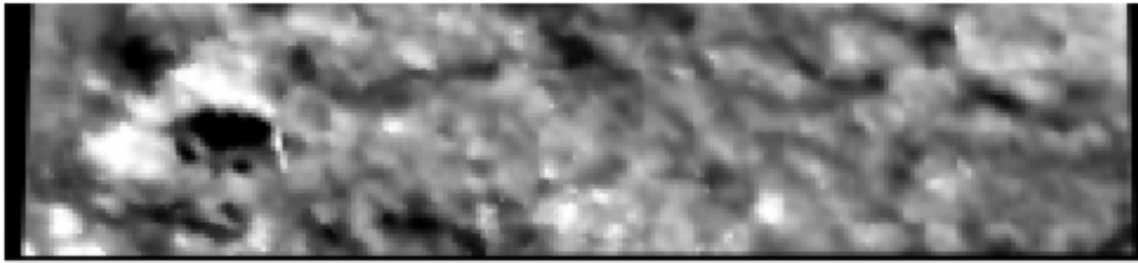


Figure 5.19: Average median size of regions of change over multiple runs.

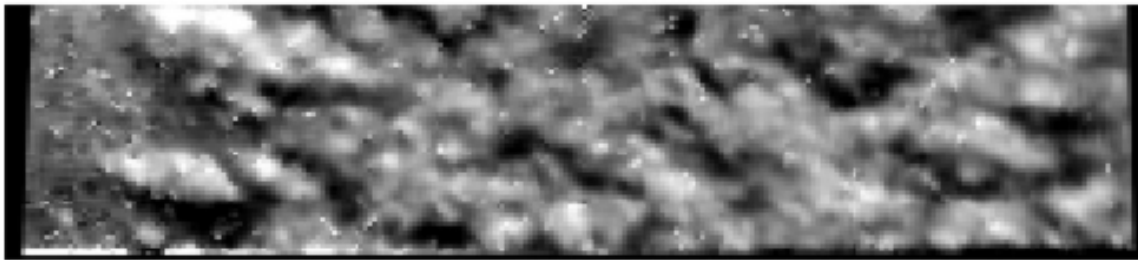
The fact that the data trends are consistent over the runs for all these statistical quantities gives greater credibility to the trends discovered by this ratio method. Blocking the UV plasma light from reaching the propellant has no observable effect on the propellant decomposition. The ratio structures form at the same rate, at the same sizes, and in the same numbers between runs with an acrylic and a fused silica window mask. The same fused silica run shows lower illumination in Fig. 5.16, lower number of regions in Fig. 5.17, and lower percent area in Fig. 5.18. The window cracked during this run and the lower amount of plasma radiation reaching the propellant resulted in less energy transfer to the propellant and hence less decomposition at the surface. From this result, we can conclude that the difference in radiative energy reaching the propellant surface

between using the fused silica mask and the acrylic mask is insignificant, and the additional UV light hitting the propellant through the fused silica mask has no observable effect over the visible/IR plasma light. This supports the conclusion that the plasma radiation/propellant interaction is largely a thermal decomposition process.

One last observation made using the propellant surface images alone is shown in Figure 5.20. The last image illuminated by the plasma during a run (836 μ s) is compared with an image of the same propellant surface a few minutes after the run. The propellant surface has changed significantly during this interval. There are no large blisters evident in the image after firing. This is surprising because Fig. 5.9, a larger and lower resolution view of a similar surface shows larger blisters. However, the larger blisters are difficult to distinguish in the center of the propellant in Fig. 5.9, which is the field of view for Fig. 5.20. The image of the propellant after the firing does show that the area containing decomposition structures is larger. Therefore the propellant continues to react and decompose after the plasma irradiation ceases.



(a)



(b)

Figure 5.20: Comparison between propellant surface images at a delay of a) 5 minutes after the plasma firing b) 836 μ s

Figure 5.21 is an example time sequence of laser scattering images all taken during the same run. The sequence very closely resembles the pseudo time series taken by the ICCD in Fig. 5.13. The major differences are that there is lower resolution and a smaller field of view for the images in Fig. 5.21. Also, the exposure time of the camera is greatly increased so the background plasma light can be seen scattering off particles outside the focal plane at delays of 136 and 236 μ s. One of the original reasons for using the high framing rate cameras was to observe how the material propagated away from the propellant surface

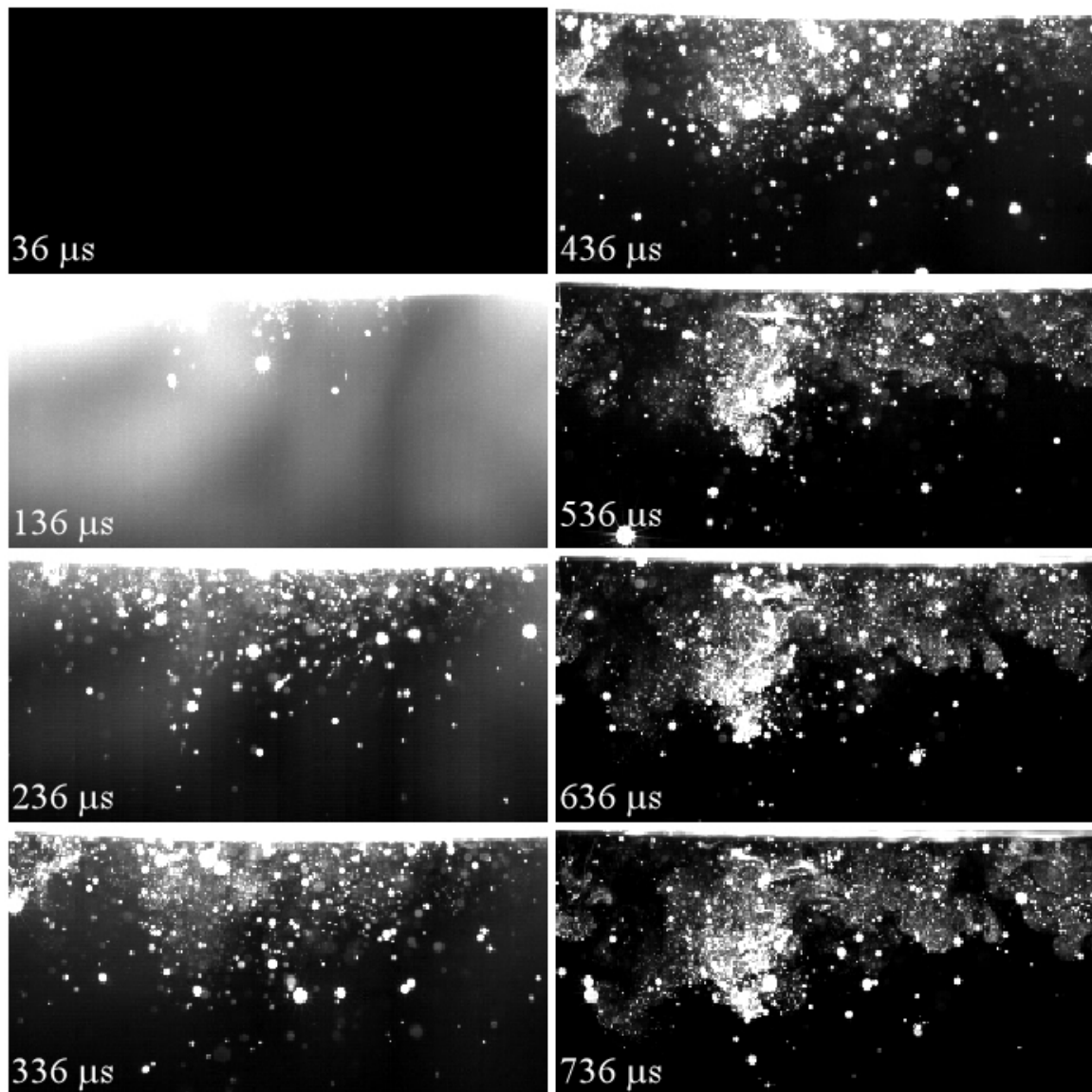


Figure 5.21: Example time sequence of laser scattering images taken during the same run.

during the discharge. The sequence in Fig. 5.21 starts out the same as in Fig. 5.13, with particles appearing between 100 and 150 μs . Material propagates downward as the discharge progresses. However, the structures observed throughout Fig. 5.13 are not readily apparent over times of 136 to 536 μs in Fig. 5.21. It is probable that the particles in the laser plane are slightly obscured by scattering from plasma light. After 536 μs there

is an obvious correlation between images, and the particle structures change very little from frame to frame. The bright structure that is fully formed at a delay of 536 μs is too bright to be obscured by plasma light scattering, and appears to form at about 200 μs . The temporal resolution of the image sequence is not high enough to resolve trajectories of individual particles and larger structures during the plasma discharge. It should also be noted that the momentum of the structures observed must be very small for them to form in 200 μs and then be stopped by the surrounding air for the rest of the sequence.

Figure 5.22 is an example time series of cross-plane plots of both the scattering and propellant surface images. These plots are similar to the one described in Fig. 5.18 of Chapter 4. The observer is looking at both the laser scattering and propellant surface from a point below the propellant and towards the cameras. The propellant is reacting throughout the entire field of view of the camera during the entire series, yet the ejection structures are not appearing throughout the width of the scattering images. An examination of the particle evolution reveals no obvious correlation between the particles and the changes to the surface. While brighter particle structures do appear at decomposition regions, particle structures do not appear over all decomposition regions. Unfortunately the half width of the laser sheet, marked in the images, is larger than the size of most decomposition structures during the discharge. This makes it difficult to determine the exact location from where the propellant material is ejecting. After 536 μs the particles away from the propellant surface move very little between images, and so these later images would not be expected to correlate with what is observed on the propellant surface.

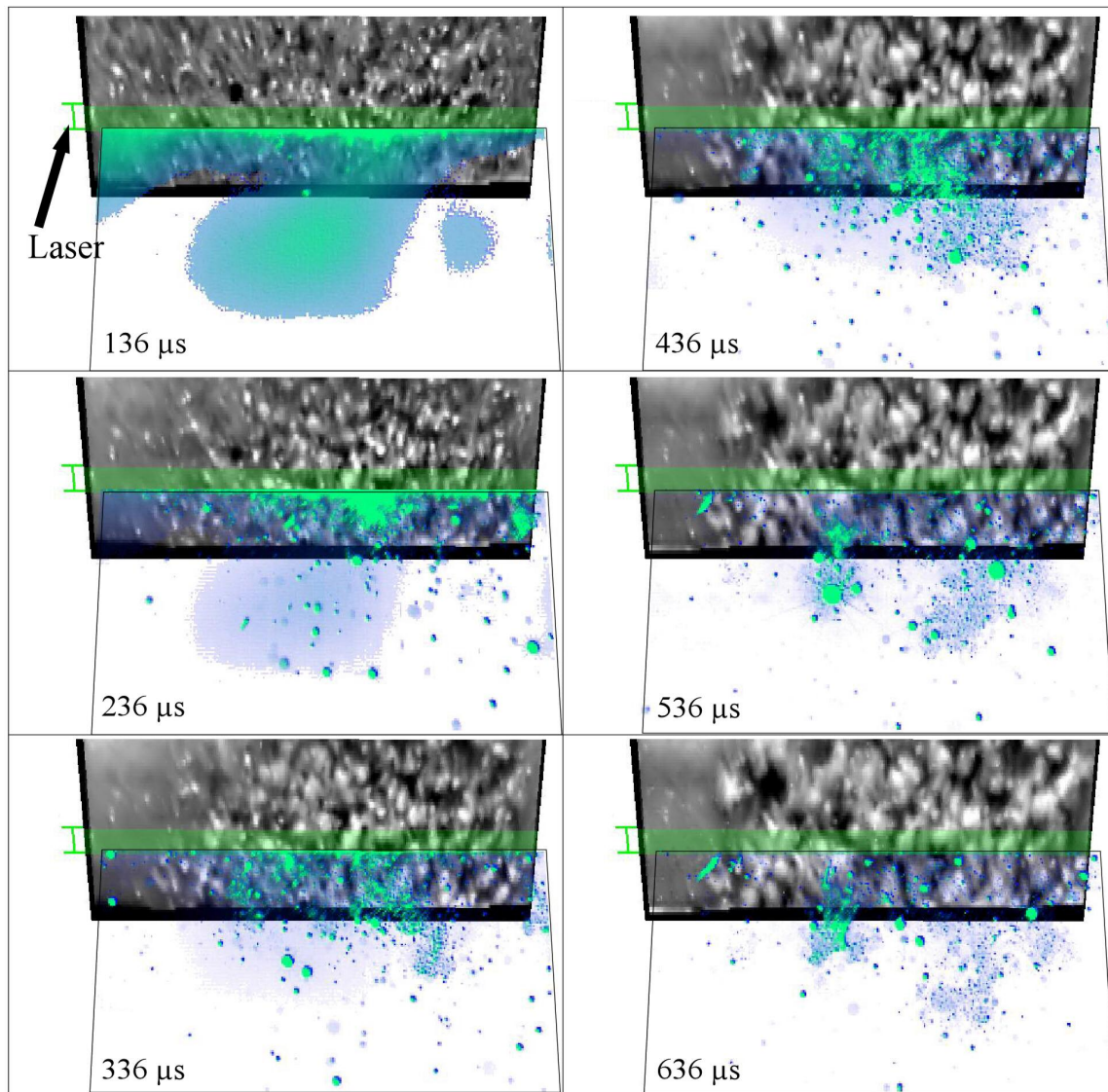


Figure 5.22: Example time series of propellant surface images and laser scattering images plotted together.

Attempts to correlate sections of the particle images away from the propellant surface with the region of propellant images encompassed by the laser met with little success. Figure 5.23 shows examples of correlations made from two runs at three different delays. Delays of 236 and 436 μs are during the plasma discharge while the delay of 636 μs is on the tail end of the discharge and is not expected to produce a strong

correlation. The cross-correlations for each time delay were converted into an array so that the top row corresponds to the correlation of the scattering image strip closest to the propellant surface. Surface plots of the cross correlations were made and appear at the same viewing angle as the laser scattering images in Fig. 5.22. The top of each plot shows the correlation for the strip closest to the propellant surface, with the bottom being the furthest away. The run on the left is the same run that produced Fig. 5.22.

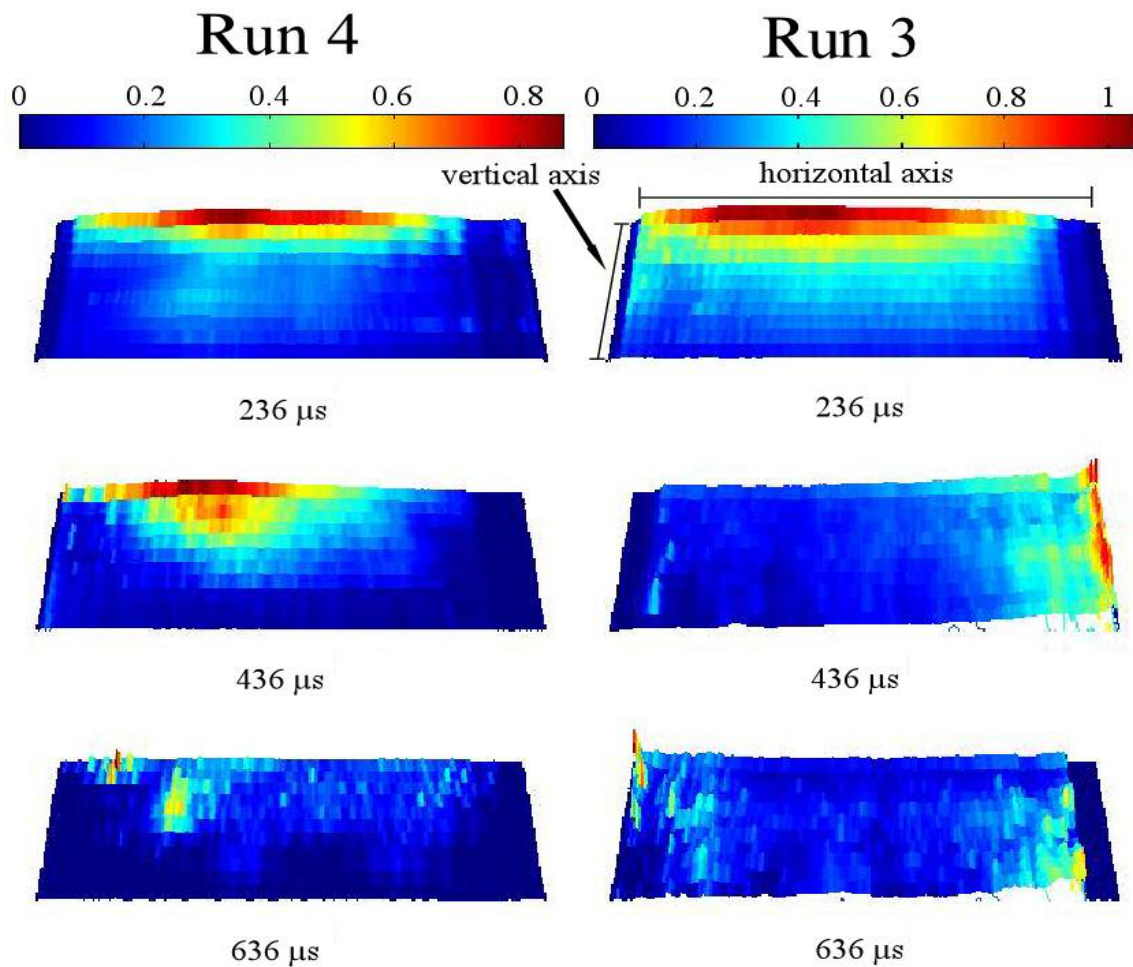


Figure 5.23: Example cross correlations between the propellant surface and laser scattering images.

If the scattering and surface images correlated well, a peak would be expected in the center of each strip corresponding to zero position. At the early times this peak should appear only in the strips closest to the propellant surface. As time progressed smaller and broader peaks would be expected to appear in strips further from the propellant as the particle structures expanded and moved away from the original position that produced them and the decomposition structures on the propellant surface grew. Particles further

away from the propellant surface would correlate with decomposition structures formed earlier on the surface, which would still be visible throughout the entire image sequence. None of the runs produced this ideal cross correlation. The run on the left of Fig. 5.23 is the closest the correlations came to matching the ideal. There is a peak, but it is offset to the left. Looking at Fig. 5.22, this seems to be caused by the bright particle structures near the surface to the right of center correlating with the bright decomposition structure in the center of the surface images.

It was common in the early images of all runs to find the strip closest to the propellant surface with high correlations along its entire length. The reason for this is the top row of pixels in these scattering images have large signals due to bleeding from detector pixels viewing the propellant surface as well as a large amount of particles being created across the entire width of the propellant at this time. Also there is no correlation between the images at 636 μs because particles are not being produced at that time, and all the scattered particles were produced at an earlier time. Cross correlations between the surface ratio images and the laser scattering images were attempted as well. Correlation peaks would only be expected in the strips closest to the surface. However, very little correlation was found with these two image sets as well.

Another phenomenon observed with the laser scattering images was continued reaction and bubble formation well after the plasma discharge. Figure 5.24 contains an example sequence of images starting at a delay of 1036 μs and progressing to 10 ms. Two observations are made in this series. The first is a large bright region appearing and growing on the surface of the propellant during the sequence, labeled "A" in the figure. The bubble appears between 1 and 2 ms and grows steadily until 8 ms with a maximum width of about 2.6 mm. Bubbles are commonly seen growing out of the propellant

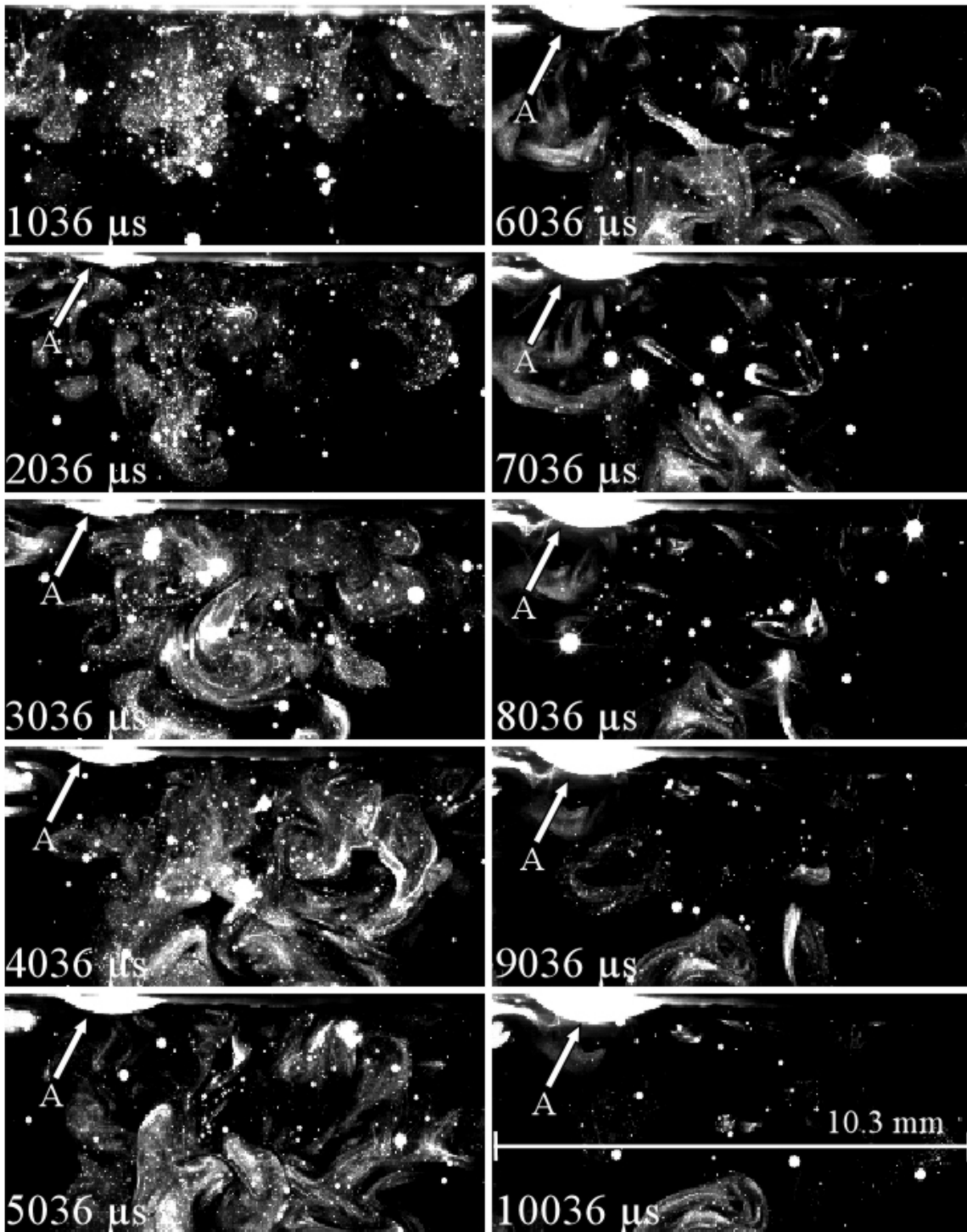


Figure 5.24: Example scattering image sequence after firing.

surface after the plasma firing and are seen in all the scattering image runs. This image sequence is displayed because the bubble is so large; bubbles are usually about 1 mm in size. These bubbles are probably the larger blisters observed on the propellant surface after each firing. It is interesting that the laser illuminates both sides of the bubble. This might be evidence that the structure seen is in fact hollow.

The second observation is that during this sequence the larger, more diffuse type of scattering structure appears. At 1 and 2 ms the particles are similar in structure to those in Fig. 5.21. However, at 3 ms some scattering structures appear that resemble the larger, brighter, more diffuse scattering structures seen in Fig. 5.13. These structures resemble an intermediate point in a scalar mixing process where the particle density is considered the scalar. This implies that at some point previously these particles were in a region of more uniform density and were then mixed with the air away from the propellant surface. The bubbles would presumably contain a relatively homogenous volume of fluid before bursting. Also, these structures coincide with the appearance of the bubbles on the surface, so it is possible that they are a result of exhaust from the bubbles.

One run was conducted using simultaneous imaging where the OD2 neutral density filter on the propellant surface camera with an OD0.6 neutral density filter. This enabled viewing of the propellant surface over much longer times. A bubble did appear in the scattering images on this run, and Fig. 5.25 is a time sequence of close up views of the two camera images plotted on the same cross-plane view. The green strip across the surface images marks the laser. The bubble appears at 1516 μs and grows up to, and beyond, the end of the sequence at 2616 μs . It has been colored light-blue and labeled "A" throughout the sequence in Fig. 5.25. It appears on the figure below the laser strip because the top of the scattering images are actually offset from the original surface position and the cross-plane figures are viewed at an angle. The changes on the propellant

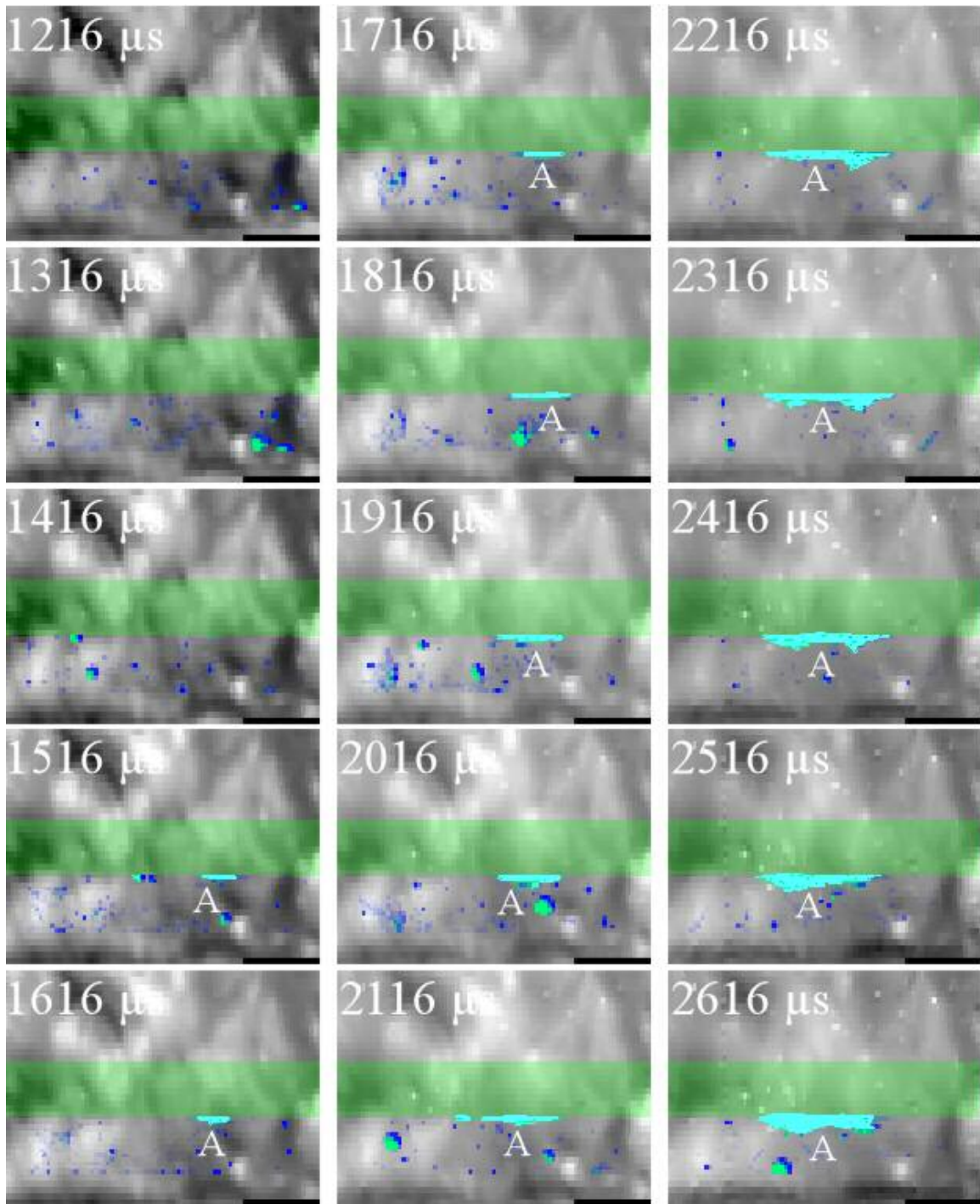


Figure 5.25: Time sequence of close up view of bubble growing with corresponding propellant image. Bubble has been false colored light-blue and labeled “A”.

surface do track with the formation of the bubble in the scattering images. The propellant continues to decompose throughout the time sequence, and there are lighter regions on the surface where the bubble is lowest, with darker regions where the bubble surface dips. However, there is nothing in the surface images alone to obviously mark that region as bubbling outwards. This does suggest that there is some three dimensionality associated with all the changes taking place on the propellant surface.

REPEATABILITY OF RESULTS OVER MULTIPLE FIRINGS

The trends observed in this work are sometimes exemplified by data taken from single runs of the plasma firing and plasma propellant interaction. These trends are valid only when the results are repeatable over many runs. It has been mentioned that generally the results of individual firings are similar and because of that the trends observed by comparison of images and data taken from separate firings are valid. This section will examine this claim in greater depth.

An extensive study of repeatability over many shots using one experiment was not conducted. However, for almost every experiment a few runs of a specific setup or delay were recorded, and the results, over many different experiments on the plasma jet, show that all aspects of the plasma jet and plasma propellant interaction are generally repeatable. While one example of repeatable results is not enough to show it in general, the constant repeatability over small numbers of firings for a large number of experiments is enough to conclude the results are generally repeatable.

Figure 5.26 shows four monochrome visible emission images of the plasma jet into open air at the same delay of 150 μ s over four different runs. While there are noticeable variations in the plasma jet on the small scale, the large scale structures are the same in each image. The barrel shock and Mach disk are clearly visible. Also, the width of the barrel shock and the distance of the mach disk and upper boundary of the jet from

the jet exit are very similar between each image. The fact that the plasma jet firing is almost the same from run to run is the cause for repeatability of the plasma propellant interaction.

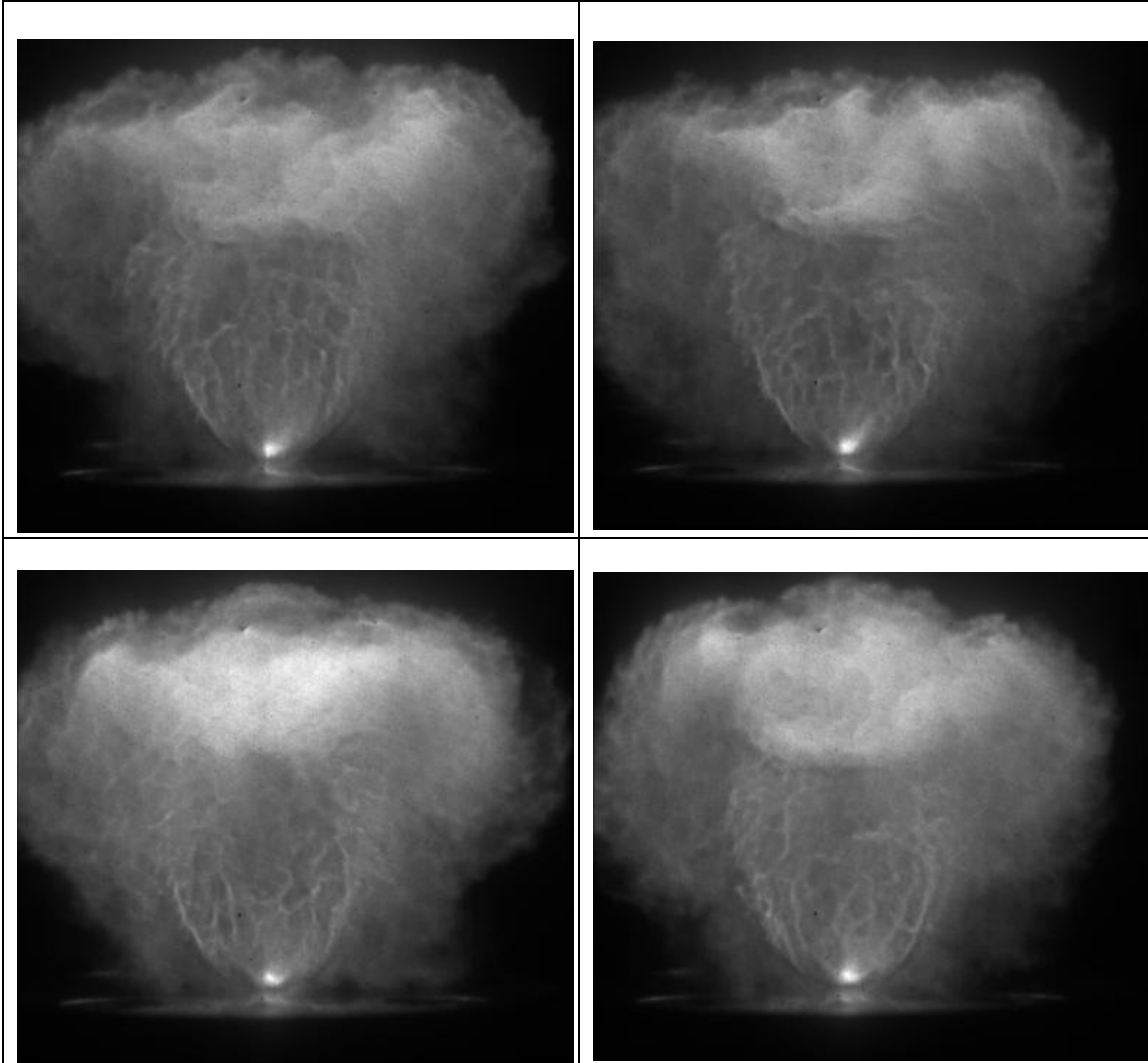


Figure 5.26: A number of visible emission images of the plasma jet in open air taken at a delay of 150 μs .

Figure 5.27 shows two acquisitions of one portion of the emission spectrum used to create Fig. 5.7. This data shows the emission of the plasma confined in the radiation

chamber between 360 and 480 nm. While the two do not match exactly, the intensity is generally the same. Also, the positions of the oscillations in the spectra match closely.

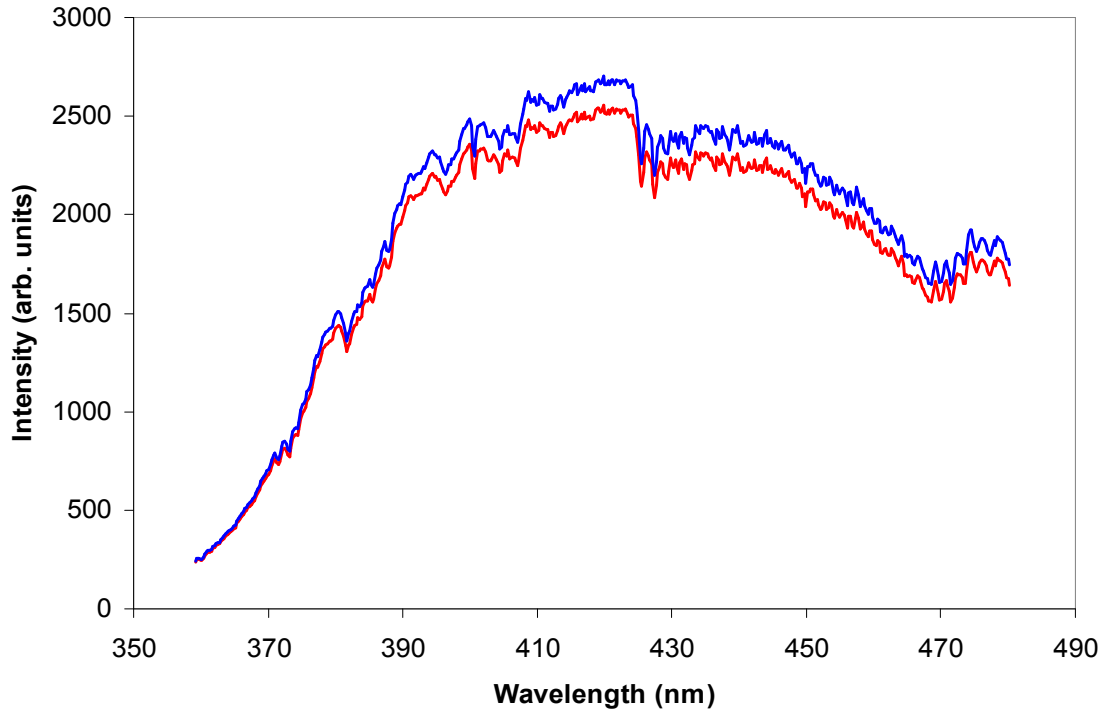


Figure 5.27: Two emission spectra taken during separate firings of the plasma inside the radiation chamber at 150 μ s.

Three NO PLIF images taken at 250 μ s during three different runs are shown in Fig. 5.28. There are marked differences between the runs in this case, but the general features are similar. By this time NO has appeared below the entire propellant surface in all three images. The NO structures appear below the propellant surface with different distributions in each image, but the distance the NO has reached away from the propellant at this delay is similar in each image. In addition to this, the more prevalent structures (smaller, dimmer) are of similar sizes for each run.

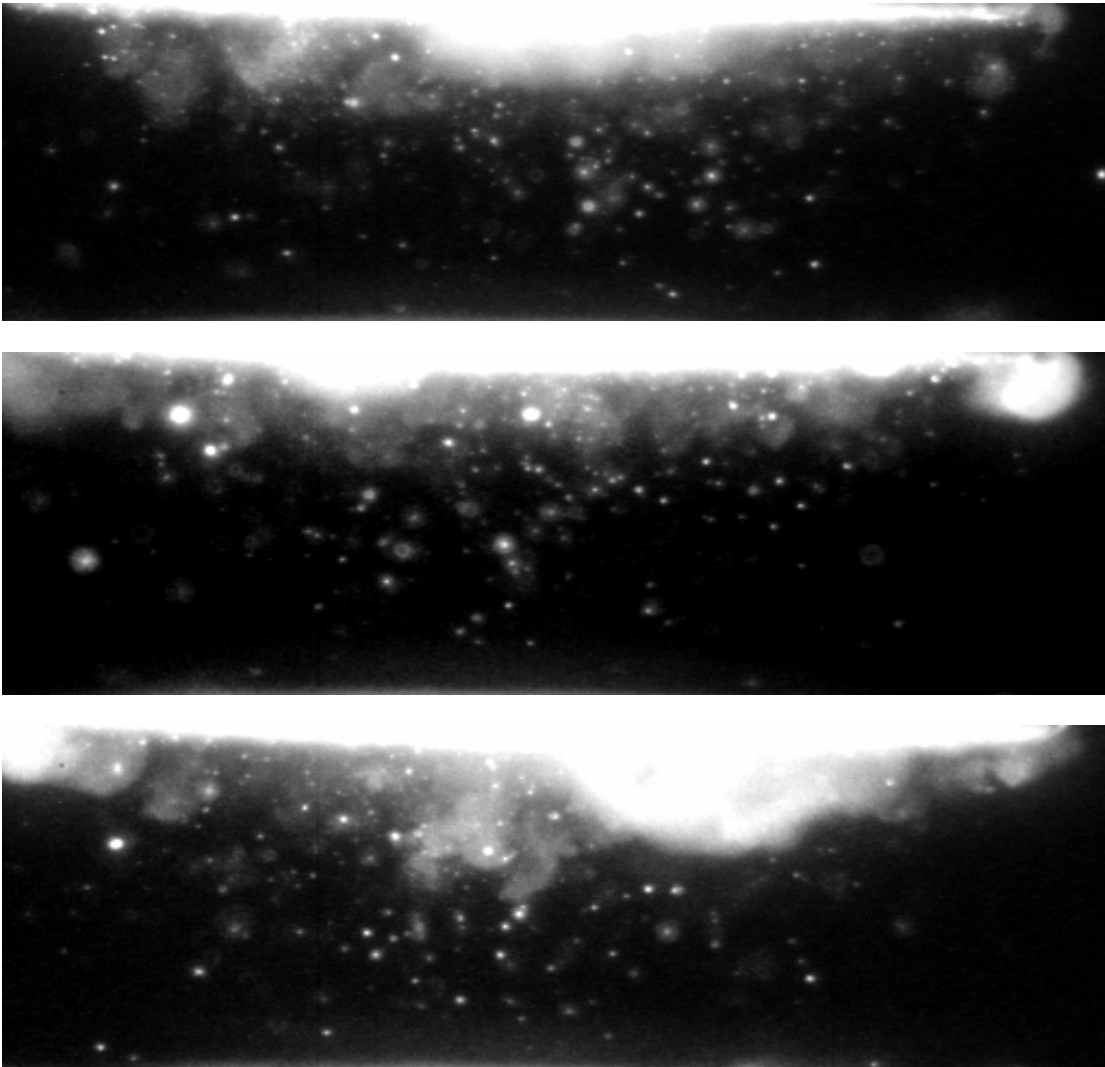


Figure 5.28: Three NO PLIF images at 250 μ s delay.

The same comparisons made for the NO PLIF images can be made for the particle scattering images shown in Fig. 5.29. Here, the particle structures have not appeared below the entire surface, but the structure sizes and shapes are very similar between images. Also, the structures have reached similar distances away from the propellant.

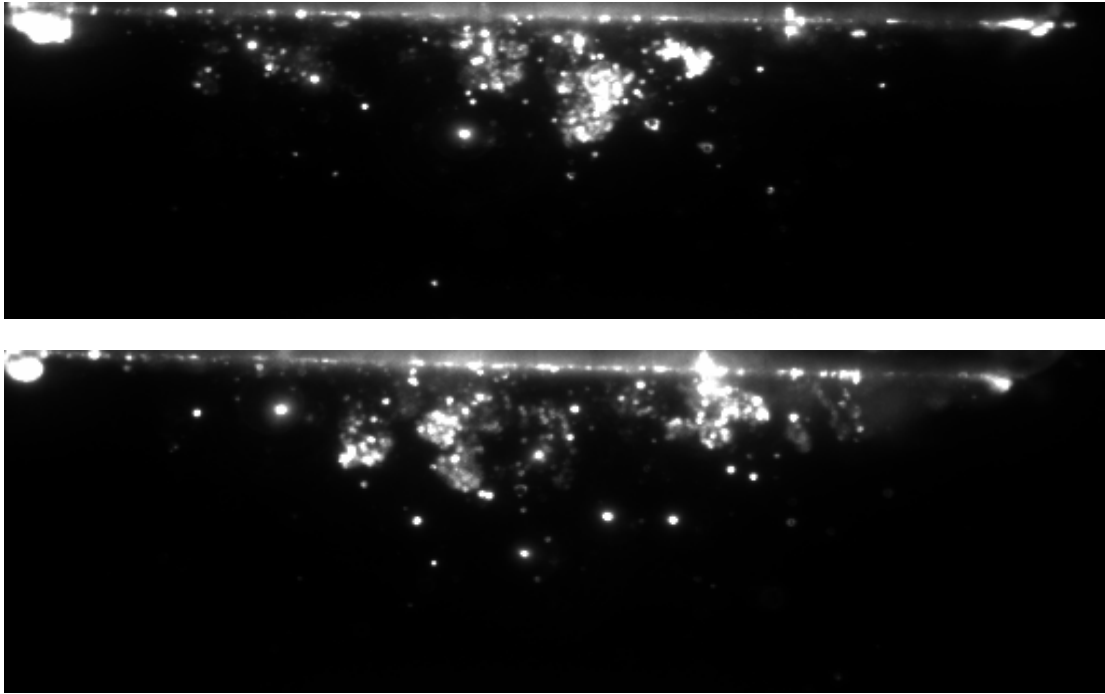


Figure 5.29: Two particle scattering images at 250 μs delay.

Finally, the imaging of the propellant surface is shown to be fairly repeatable in Figs. 5.30 and 5.31. The average intensity per pixel is shown over the course of a number of runs for both window masks in Fig. 5.30. While the exact signal is not always the same, the trends in the intensity over the course of the run are the same in all firings. There is an increase in intensity up to a global peak at 100 μs . Then the intensity decreases to a local minimum at about 300 μs . There is a second peak at about 400 μs after which the intensity decays completely. Figure 5.31 shows the number of regions of change seen on the propellant surface over the course of multiple runs. Once again, the number of regions is not always the same, but the trends are the same throughout each run. The number of regions quickly increases to a peak at about 200 μs , after which the number gradually decreases until the plasma discharge is finished.

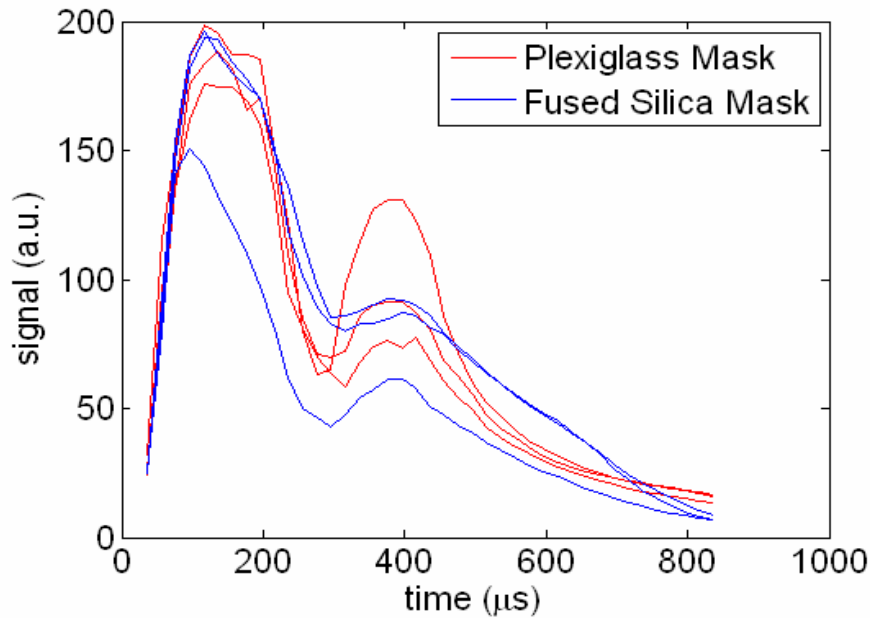


Figure 5.30: Average intensity per pixel of propellant surface images for individual runs.

As has been shown in this section, the phenomena occurring in the plasma and the plasma propellant reaction are generally repeatable. While there are obvious differences between runs, the large scale events and trends occur in every run. Throughout the discussion of results a concentration on the absolute numbers in these measurements has been avoided. The absolute numbers of the measurements are not always the same between runs, but the trends are. Therefore the trends observed in a few runs can be assumed to occur during most plasma firings with this setup.

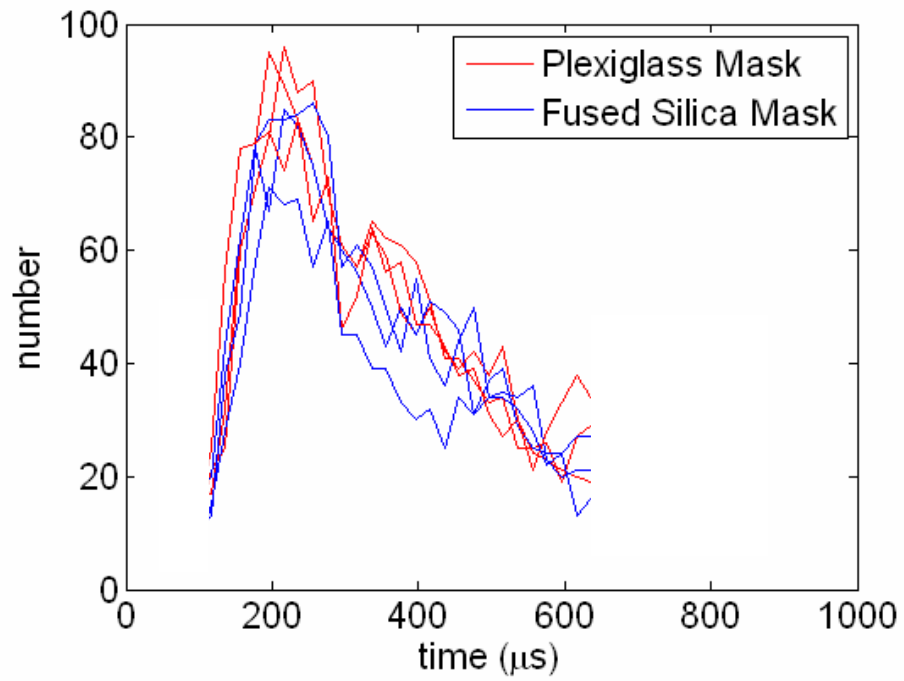


Figure 5.31: Number of regions of change on propellant surface for individual runs.

Chapter 6: Conclusions

These experiments were designed to gain some insight into what is happening at the propellant surface during a plasma radiation/propellant interaction. Both NO and particles were observed ejecting from the surface of the propellant during the PRPI, and the propellant surface change was observed in real time during the interaction. The fact that this interaction was observed in real time is significant. No imaging of the propellant surface or ejected material during the interaction was found in the literature. The propellant has generally been tested and imaged at delays much greater than the time scale of the PRPI.

A major new result of this work is the observation that decomposition of the propellant occurs with the ejection of material in semi-discrete events. It has not been determined if these discrete ejections occur directly on the surface or come from the bursting of blisters forming on the surface. The observation of mushroom shaped vortex rings in the particle scattering images, though rare, is evidence of jets of material from the propellant.

Furthermore, another important finding is that particles are ejected from the propellant surface during the plasma radiation/propellant interaction. These particles have a large range of sizes, and their composition is unknown. The particles cannot be tracked during the plasma firing using the Photron high speed cameras. The delay of 100 μ s between frames is not short enough to follow particle movement. Also, the mass percentage of material produced in the decomposition composed up of particles is not known. If a large number of particles are produced in a plasma ignition event this could greatly influence the rate of gas produced by the propellant during and after the plasma

discharge. The large surface area to mass ratio of individual particles would greatly increase the decomposition and/or burning surface area of the propellant.

The NO ejection structures appeared to correspond to the particle-scattering structures. Both the NO and particle structures appeared at the same time in the discharge, had similar shapes and sizes, and expanded at similar rates. This is evidence that common decomposition events during the PRPI cause both the expected decomposition products as well as particle ejections.

No major correlation was observed between the ejected material and the changes occurring on the propellant surface. There are two possible reasons. Firstly, the data did not have high enough temporal and spatial resolution to discern the changes. Secondly, changes observed on the surface do not necessarily mark where material is being ejected. The propellant surface imaging showed a surface that changed constantly during the plasma discharge. However, the ejected material imaging showed evidence of discrete events, at least with individual larger particles, if not with the particle structures themselves. If the surface changes were considered to be small blisters at the surface, ejection would be in the form of discrete events. The surface changed similarly over the entire field of view of the camera during the plasma discharge, yet this did not produce evenly distributed amounts of material ejecting over the entire surface. It is also possible that the material produced during the plasma discharge is a result of ablation and subsequent dissociation directly from the propellant surface as a result of energy deposition there. If this were the case, decomposition underneath might not correlate with the material produced. Simultaneous NO imaging and surface imaging or particle imaging would help to determine if decomposition of the nitrate groups in the propellant was simultaneous with particle emissions or changes to the surface. Unfortunately, simultaneous high speed particle scattering and NO imaging was not possible.

In the two camera experiment only the smaller more irregular type of particle structure was observed during the plasma firing while the brighter, larger structures appeared later. The difference might be a result of lower radiation reaching the propellant surface due to increased distance, or it might not have occurred in the small number of runs recorded with the two camera setup. The larger, smoother structures can be seen in scattering images well after the discharge terminates (this can be seen in Fig. 5.24). It is probable that the smaller, blotchy structures are a result of the high radiation flux during the plasma discharge. Plasma radiation continues to impinge on the propellant after the discharge (there is enough light at 2.6 ms to illuminate the propellant in a 4 μ s exposure through an OD 0.6 neutral density filter, about 25 times less light than at the end of the discharge) but these structures do not appear. The larger particle structures observed in the two camera imaging might be the result of a larger blister exhausting. The larger blisters tend to appear at the same time as the larger, brighter particle structures, well after the plasma discharge terminates.

A reasonable guess can be made as to whether radiative or thermal decomposition causes the major changes to the propellant. There was no noticeable difference in the changes to the propellant surface between runs using a fused silica mask and an acrylic mask. Also, the propellant continues to react and change up to and possibly beyond the 10 ms the scattering camera recorded, with the larger surface structures visible to the naked eye probably forming after the initial plasma discharge. It is possible that there is sufficient irradiation of the propellant by the plasma to cause decomposition well after the capacitor is finished discharging. However, no new small particle structures appear at the propellant surface after the plasma discharge. It is possible that the decomposition is a slow process taking milliseconds to complete. However, this is very unlikely because

NO, a final decomposition product, is seen as soon as the propellant surface begins to change.

It is most likely that the propellant continues to decompose due to the increase in temperature resulting from absorption of plasma radiation in the bulk of the propellant during the plasma discharge. The larger blisters form at depth inside the propellant, and the surface continues to change long after the majority of the radiative energy has been absorbed by the propellant. The JA2 used in these experiments contained graphite that made it less transparent than graphite-free JA2. This markedly reduced the depth to which radiation affected the propellant. It is assumed that the reactions to plasma radiation are similar in both regular JA2 and graphite free JA2 because of the similarities of the propellant surfaces after exposure to plasma radiation.

Regardless of the source of change, the delayed propellant response to the plasma radiation raises a major question of the plasma radiation-propellant interaction. It is unknown how much the observed changes in JA2 propellant due to plasma radiation would affect propellant burning in a gun firing. Propellant burning in full scale gun tests lasts tens of milliseconds. However, the portion of propellant most affected by plasma radiation burns off early in the firing due to its proximity to the burning surface. While the burning rate of the propellant is increased when temperature is raised in-depth from radiative energy deposition, it might be increased more if in depth decomposition begins and blisters form before the burning surface reaches it.

Appendix A: Propellant Surface Temperature Measurements in Open Air Jet

EXPERIMENTAL SETUP

Because of its effect on propellant decomposition rate, gas generation rate, and potentially on ignition, time-resolved propellant surface temperature was studied during an open air plasma-propellant interaction. Fitting relative copper emission line strengths to a Boltzmann plot is a common method of studying electrothermal plasma temperature, and it has been used in the past to study a plasma propellant interaction. In an open air interaction the propellant does not ignite, but the surface is visibly affected by a decomposition reaction. For the copper line temperature measurements the plasma jets into room air through the 3 mm cathode-nozzle. A 12 mm diameter disk of JA2 sheet propellant is placed 12 mm above the jet exit on the end of a steel rod so that the jet impinges normally to the surface. This is closer than the heat flux gauge was ever placed, but was done to create a significant level of reaction on the propellant surface. A lens focuses plasma light onto either a 400 μm or 100 μm diameter fiber optic which a Spex 1681 spectrograph spectrally resolves and a Princeton Instruments PI-Max intensified CCD camera records. The spectrometer, gated to 1 μs , records line of sight emissions spectra focused on the 3 mm or 0.75 mm closest to the propellant surface, depending on the fiber diameter. Because image acquisition speed is much slower than 500 μs , only one spectrum is taken per firing. However, firings are repeatable so that it is possible to measure a full time history of the temperature of the fluid at the propellant surface during the plasma discharge.

The spectrometer is set to record spectral data between 480-600 nm. The spectra are processed to account for differential wavelength response by the detector and

differential response with respect to pixel number due to the spectrograph. Six copper emission peaks in this wavelength range, shown in Table A1, are then fit to Lorentzian lineshapes while simultaneously fitting surrounding lines and the background continuum luminosity (estimated as linear). The areas under each fitted emission lineshape are interpreted as total emission signal and are then compared on a Boltzmann plot. The points should fall on a line with the formula

$$\ln\left(\frac{I\lambda}{A_{ul}g_u}\right) = B - \frac{E_u}{kT_{exc}}$$

Here I is the relative intensity of an emission line, λ is the emission wavelength, A_{ul} is the spontaneous emission rate, and g_u is the degeneracy or statistical weight factor for the excited (upper) state, B is a constant, E_u is the energy of the upper state, k is Boltzmann's constant, and T_{exc} is the excitation temperature. If the gas is in local thermal equilibrium $T_{exc} = T$, where T is the gas temperature. In practice the temperature is inferred from the slope of a straight line fit to the data using a least squares technique.

Line #	λ nm	g_u	E_u eV	g_l	E_l eV	A_{ul} $\times 10^8 \text{ s}^{-1}$
1	510.55	4	3.816	6	1.389	0.020
2	515.32	4	6.190	2	3.785	0.60
3	521.82	6	6.191	4	3.816	0.75
4	529.25	8	7.735	8	5.394	0.109
5	570.02	4	3.816	4	1.642	0.0024
6	578.21	2	3.785	4	1.642	0.0165

Table A1: Copper emission lines used in temperature measurement.

DETERMINATION OF LOCAL THERMODYNAMIC EQUILIBRIUM

In order to calculate a valid temperature from emissions data, the plasma must be in local thermodynamic equilibrium. With a reference ionized carbon plasma at 10,000 K calculations using formulas from Griem (1997) or Fujimoto et al. (1990) show that the electron density needs to be around 10^{21} cm^{-3} for full LTE. However it is not clear how these models extend to atoms and ions that are not hydrogenlike. The density criterion is most likely reduced for a real plasma because ionization energies, explicit in Griem's formula and implicit in the model of Fujimoto et al., are much lower for less ionized species.

Using another formula from Griem (1997: 225), valid only when the plasma is already near complete LTE, the relaxation time of copper at 10% ionization is 1.5 ns. The largest velocities in the electrothermal plasma produced for this experiment are around 1800 m/s, so the corresponding relaxation distance is only 2.7 μm . Therefore, if copper in the plasma is already near LTE, local transport phenomena will probably not take it out of LTE.

With typical electron densities around 10^{17} - 10^{18} cm^{-3} (Kim et al. 2002) outside the capillary, it is not clear whether the plasma is in LTE. Inside the capillary, LTE is a reasonable assumption because the plasma is denser than that in the jet. It is in quasi-steady state and optically thick.

SPECTROMETER CALIBRATION

All the spectroscopic emission data shown in this work was taken with a PI-Max 512 intensified CCD camera connected to a Spex 1681 spectrograph with a 300 gr/mm grating. The spectrometer must be calibrated to ensure accurate wavelength positioning and relative intensity measurements across the visible spectrum. All data taken is

originally an image recorded by the ICCD camera. Light from the spectrograph is deposited along a band about 120 pixels wide across the camera image. An example Hg lamp image with discrete emission lines can be seen in Fig. A1. Intensity is integrated across the width of the band to calculate the signal across the spectral range. The dark charge is removed by integrating the same band on a dark image taken with the same gate duration, then subtracting it from the signal data. Signal to noise ratio is large as a result of the integration.

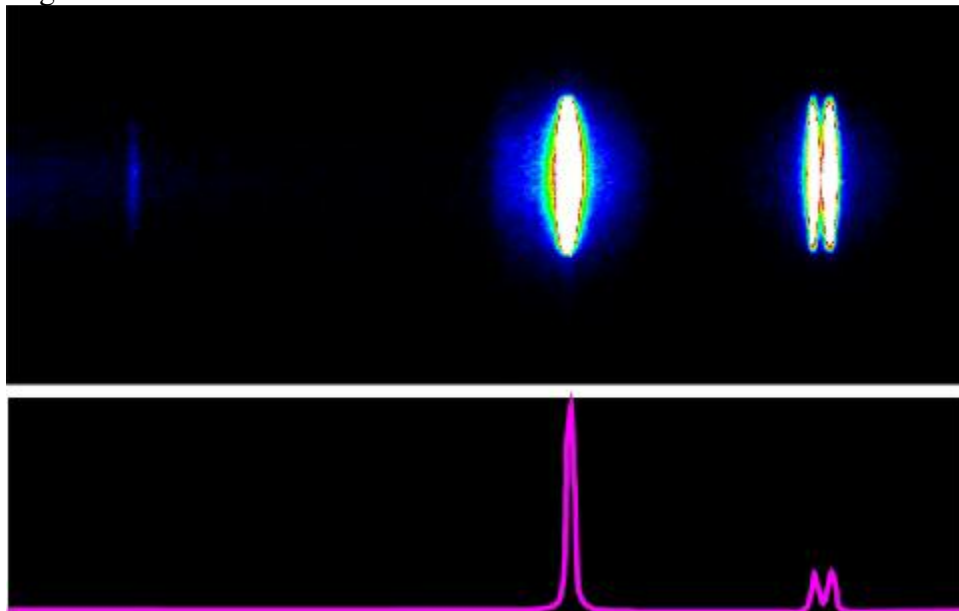


Fig. A1 Example false colored spectrometer image with corresponding integrated signal.

Wavelength is calibrated first. The spectral range of the spectrometer is about 120 nm, and the wavelength is chosen by winding a dial to the desired position (around $\frac{1}{4}$ the wavelength because the dial is set for a 1200 gr/mm grating). Images are taken with the spectrometer focused on a Mercury lamp at a range of settings. Individual Hg lines are identified by finding the direct reflection from the grating, then rotating the grating and identifying the prominent lines as they pass the detector. The peak of a number of Hg

lines (404.656, 435.833, 546.074, 576.066, 576.066 nm) are recorded when they appear at a given dial setting.

We assume the center wavelength is (dial setting – offset) X 4, the offset being the error accrued since the spectrograph was built. We also want to determine the wavelength for any given pixel depending on the spectrometer setting. Choosing the center pixel as number 256 (out of 512) the ratio of the change in wavelength per pixel must be found. The equation below is fit to the recorded Hg line positions, solving for the pixel to wavelength ratio and the offset.

$$\lambda(p) = \frac{p - 256}{r} + (s - o) \times 4$$

where p is the pixel number, r is the pixel to wavelength ratio, s is the spectrometer setting, and o is the offset. The ratio was found to be 4.22 pixels/nm and the offset was 7.1.

To calibrate the relative intensity response of the spectrometer with respect to wavelength a number of images were taken at different dial settings while focused on a Tungsten lamp with a 1/8" wide filament. The lamp is approximately a blackbody emitter, and has a calibration curve of relative intensity over the ultraviolet and visible range. Seven calibration intensity curves are shown in Fig. A2. In these curves, response seems to be dependent on pixel number as well as wavelength, termed pixel response and wavelength response henceforth, so this was taken into account as well in the calibration.

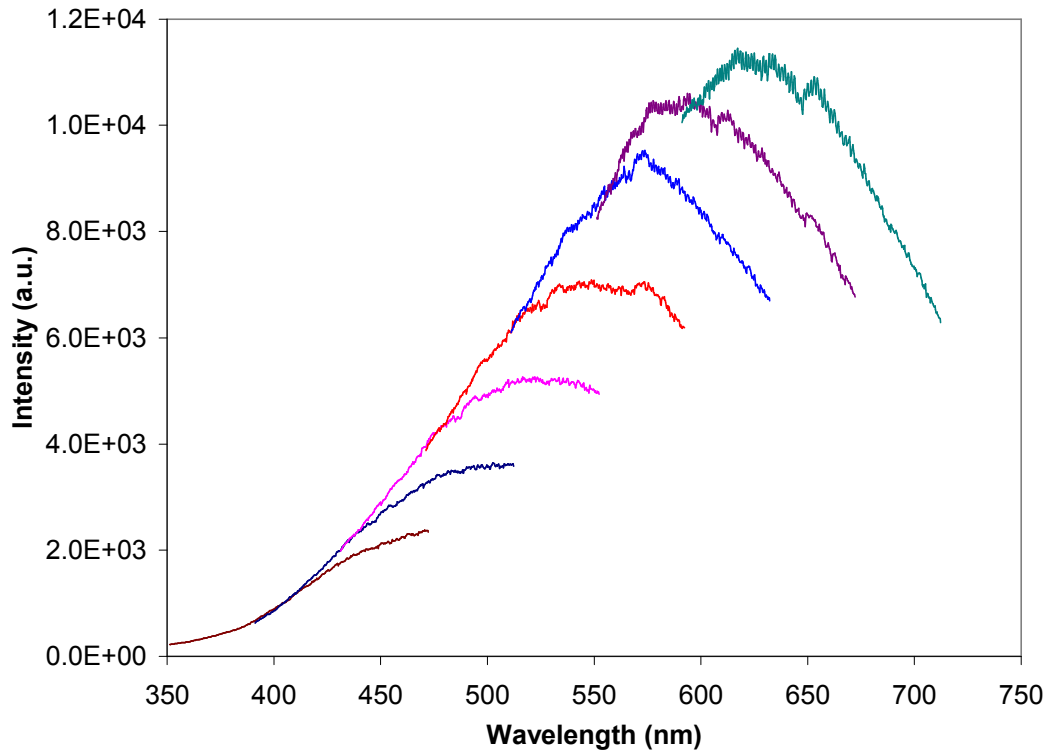


Figure A2: Calibration curves of tungsten lamp intensity over a range from 350 to 730 nm.

The intensity measured compared to emission signal is:

$$I = S \cdot P(p\#) \cdot W(nm) \cdot C$$

where I is intensity, S is signal collected by the optics, P is pixel response dependent on pixel number, W is wavelength response dependent on wavelength, and C is the unit conversion from light energy to intensity. C is ignored because units are unimportant when looking at relative intensities.

To find P it was assumed that a small section of lower number pixels and a large section of higher number pixels were attenuated, while the middle section left over was not attenuated by pixel response. A curve was produced out of all the correct middle sections from Fig. A2, which was then compared to individual attenuated sections. The

average attenuation over all the runs for a given pixel was calculated, which then became P . The wavelength response W was found by comparing the correct pixel curve with the calibration curve of the tungsten lamp.

RESULTS

A sample emission spectrum from the plasma impinging on a propellant disk is shown in Figure A3. The emission spectrum shown was collected from 0 to 3 mm offset from the propellant surface at a delay of 60 μ s after discharge initiation. The spectral fit to obtain the relative intensity of the copper emission lines is also shown. The spectral fit includes the contributions of 7 separate lines, and includes Cu lines 1-4 from Table A1. Emission spectra were also collected near 570 nm to record the intensities of lines 5 and 6 of Table A1. A Boltzmann plot of the relative intensities is shown in Fig. A4.

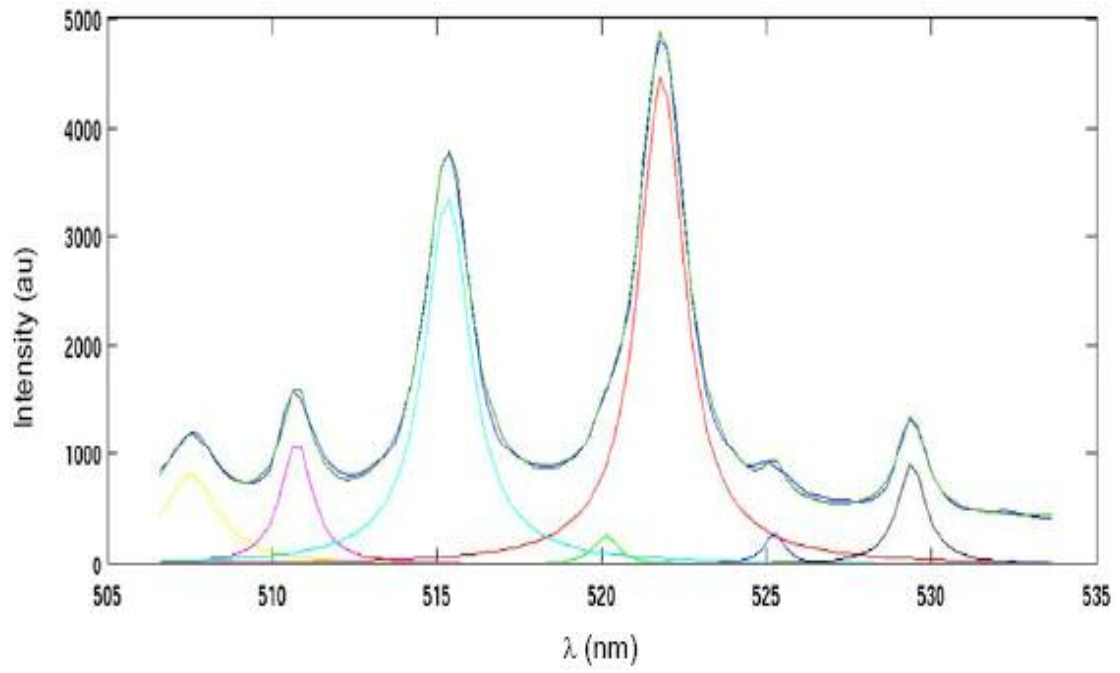


Figure A3: Plasma emission spectrum collected 3 mm from propellant surface at a delay of 60 μ s.

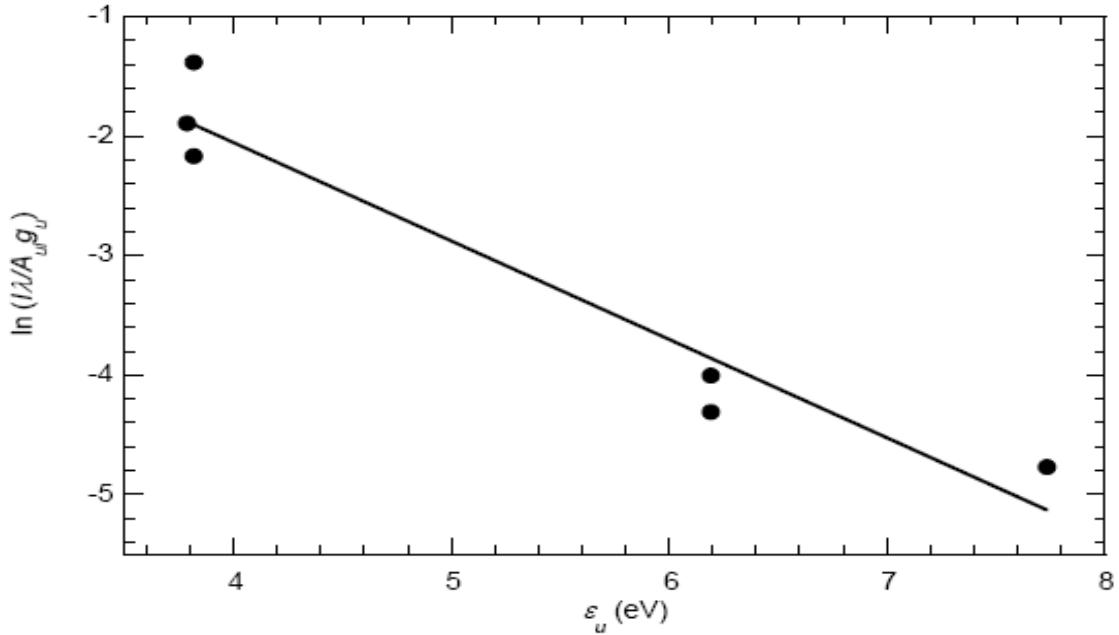


Figure A4: Boltzmann plot of Cu emission lines at 60 μ s delay; inferred temperature 14,100 K

Figure A5 shows temperature measured over the course of the discharge as well as the absolute value of current through the capillary. The solid line on Fig. A5 is the absolute value of the current and the symbols are the temperatures inferred from Boltzmann plots of emission intensities of Cu lines taken during separate firings. Two measurements were made for each delay up to 450 μ s, at which point the capacitor discharge cut off. There is a correlation between discharge current and measured plasma temperature as expected. Because the voltage across the capillary is approximately constant, the power input is nearly proportional to the absolute value of the current. However, the measured values all were lower than those previously measured behind the Mach disk in an open air free plasma jet in this lab (Kim et al. 2002). It was concluded that the spatial resolution of 3 mm with the 400 μ m fiber was larger than the bow shock

on the propellant disk. A large portion of the detected light must have been emitted from a region upstream of the bow shock. Spectra were then taken with a 100 μm fiber.

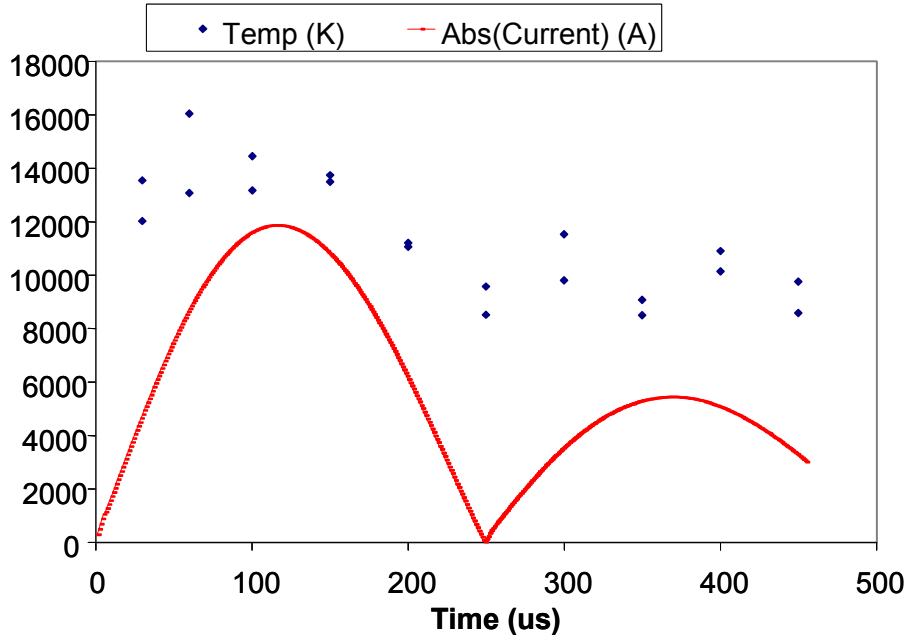


Figure A5: Variation of measured plasma temperature near propellant surface and absolute value of discharge current through capillary.

With the 100 μm fiber and the resulting 0.75 mm spatial resolution, the spectra were broadband at all delays. This made it impossible to measure temperature by fitting individual lines. A sample spectrum at a 30 μs delay can be seen in Fig. A6. Individual copper emission lines can still be seen at 570 and 578 nm. However, the lines at 510, 515, and 521 nm all appear as absorption lines in a broadband spectrum. At delays of 60 μs to 450 μs the spectra is completely broadband with no individual emission lines. An attempt was made to fit blackbody curves to these emission spectra, but the accuracy of the fits was poor. The broadband emissions and copper absorption lines with the smaller field of view indicate the plasma behind the bow shock on the propellant is optically thick. Also,

the density is greater there, with the corresponding greater temperature, than in the Mach disk, which is expected.

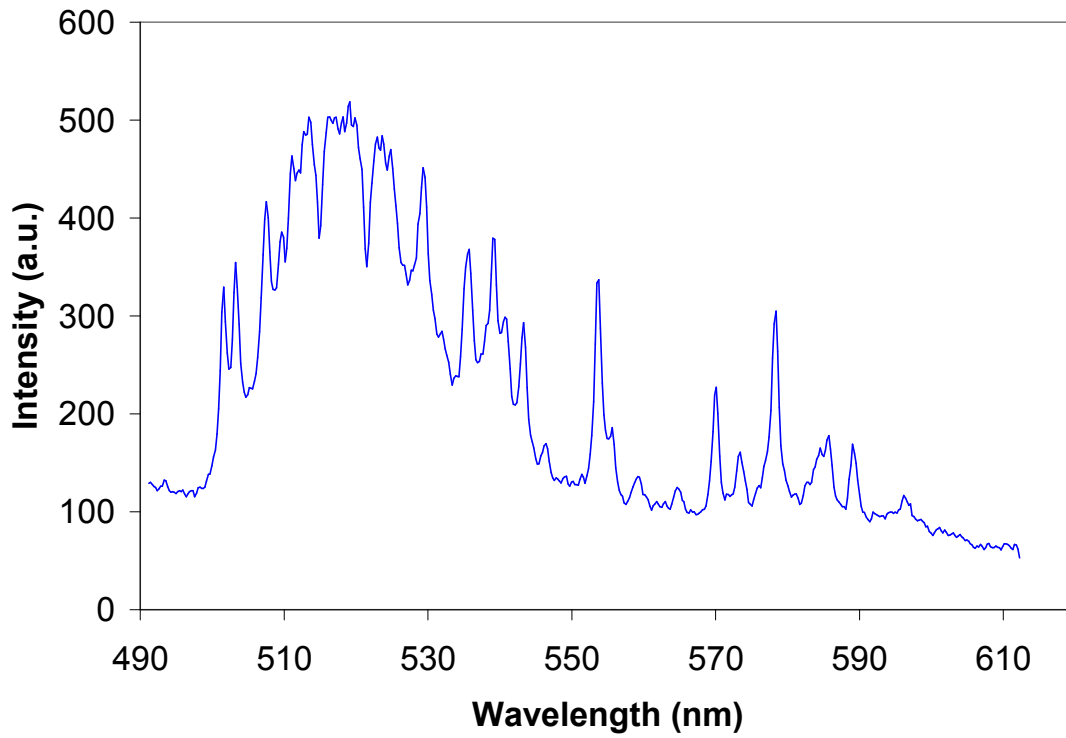


Figure A6: Emission spectrum with 100 μm fiber at a delay of 30 μs.

Appendix B: Pressure Chamber Observations

EXPERIMENTAL SETUP

For the 3.1 kJ maximum energy plasma employed in this work, a pressure chamber was necessary for the JA2 solid propellant to ignite by the plasma jet. A pressure chamber was designed so that the plasma jet normally impinged onto a disc of propellant. The plasma was confined originally to a chamber $\sim 75 \text{ cm}^3$. The first design iteration can be seen in Fig. B1. The chamber was cylindrical in shape, measuring 44 mm in diameter by 48 mm deep.

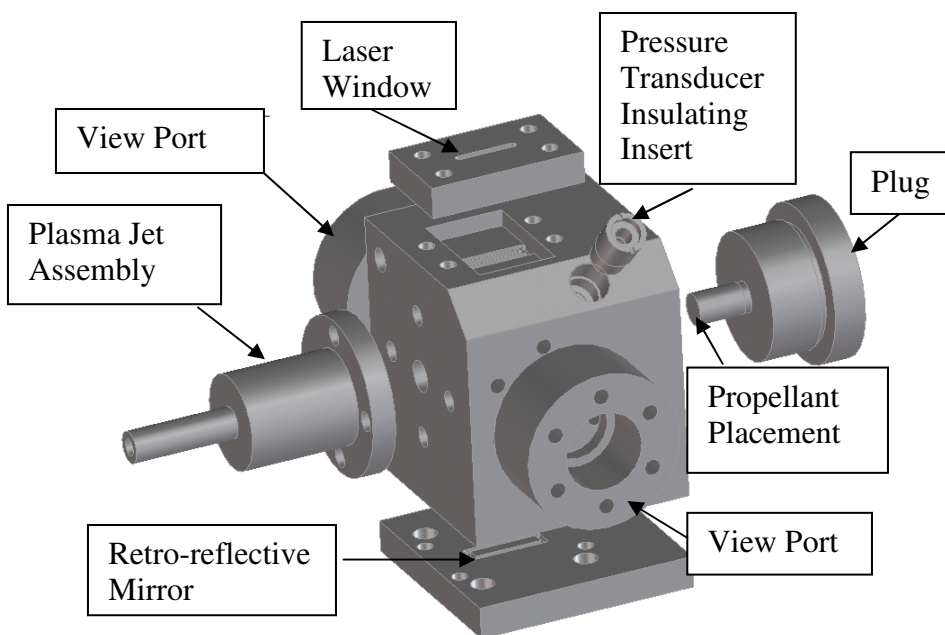


Figure B1: Closed combustion chamber with windows for viewing and laser access

Sample disks 12 mm in diameter were cut from the 2.5 mm thick propellant sheet and attached to a support rod mounted inside the combustion chamber. The plasma-jet issued normally onto the propellant disk through an elkonite nozzle 26.1 mm long, almost

three times longer than the nozzle used for the open air and radiation chamber firings. The chamber included three windows to provide optical access for the laser sheet and imaging, with space for a retro-reflective mirror on the bottom of the chamber to increase laser fluence. Furthermore, a measurement port was machined to enable pressure measurements in the chamber during the discharge by using a fast-response pressure transducer. All part interfaces were sealed by 1/16" thick viton o-ring material.

Firings with initial capacitor voltage of 3.6 kV (1.6 kJ) or greater led to propellant ignition. Subsequent design iterations involved reducing the chamber volume to $\sim 5 \text{ cm}^3$ by installation of filler pieces. These can be seen in Fig. B2. The distance of the propellant from the plasma nozzle exit was reduced to 3.2 mm, and instead of being placed on the end of a rod, the propellant disk was placed inside a well designed to hold it. Laser, pressure transducer, and imaging access were still possible, as shown in the figure.

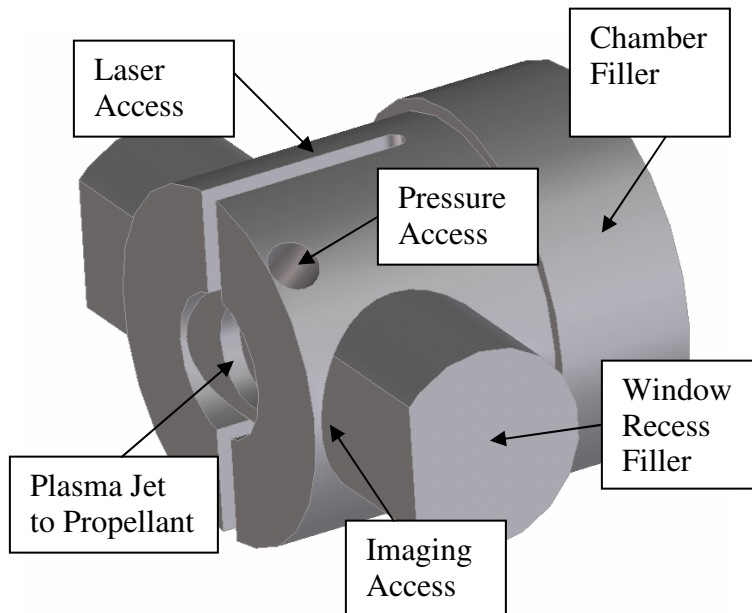


Figure B2: Filler pieces assembled to fill the main chamber and the window recesses while providing laser and pressure transducer access.

All pressure measurements were taken using a Kistler 211B1 piezoelectric pressure transducer connected to a Kistler 5114 power supply/coupler. Voltage was measured during each firing with a Tectronix TDS 520C digital oscilloscope connected to the coupler by a BNC cable. Voltage was converted to pressure by multiplying by the calibration constant, as the response was linear across the entire pressure range. The transducer has a 1 μ s rise time, and its maximum pressure is 10,000 psi. It was electrically isolated from the chamber, which is the capacitor ground, by a polycarbonate insert. This can be seen in Fig. B1.

RESULTS

Figure B3 shows a sequence of images of the visible luminosity for the case of plasma-ignition of JA-2 in the original design of the combustion chamber. The initial discharge voltage and energy were 4 kV and 2 kJ, respectively. These images were taken with a Kodak Ektapro high speed camera at a framing rate of 13,500 frames per second. The distance between the exit of the plasma jet and the JA-2 disk was 22 mm. The sequence is a composite assembled from multiple runs, because a single camera/lens setting does not have sufficient dynamic range to capture the range of intensities detected over the duration of a run. In these images the plasma axis is horizontal and it travels left to right. The propellant disk is vertical and is labeled in the second image.

The first image, captured at 0.222 ms from the start of the plasma discharge, shows the structure of the impinging plasma jet. The luminous bore exit can be seen at left and the very luminous Mach disk is seen as the triangular shaped region at right. At this instant the propellant is enveloped in the plasma. At 1.48 ms the high plasma luminosity has largely dissipated, although swirling lower-luminosity gas can still be seen in the videos. It should also be noted that the side of the propellant mounting rod can be seen in the image. Between 30-50 ms the bright luminous specks are ejected from the

surface of the propellant, which presumably mark the beginning of ignition. Such particles can be seen at 50, 100 and 150 ms in Fig. B3. A normal propellant flame as described in Chapter 2 is well established by 150 ms. The dark zone and luminous flame zone can be seen in the figure. As the propellant burned and pressure increased, the standoff distance of the luminous zone decreased. The propellant disks finished burning around 0.5 s.

Interestingly, at 10 ms the rod and propellant are barely visible. This is a result of the particulates created from condensation as the plasma cools. While this phenomenon was not noticed until laser induced fluorescence was attempted inside the chamber, it is visible even in emission images. Inside the plasma jet, temperatures are around 10,000 – 20,000 K. The total mass of material ejected in the electrothermal plasma is ~8 mg. Even when confined the plasma cools rapidly from radiation and heat transfer to the much more massive air and metal walls of the chamber at room temperature. The boiling points of the atomic iron, copper, carbon, and tungsten in the plasma range from 3134 to 5828 K. Once these temperatures are reached, nanoparticles condense out of the plasma. This condensation optically thickens the chamber, and completely scatters lasers propagating through. It is a problem that eventually led to studying a plasma radiation/propellant interaction alone to avoid it altogether.

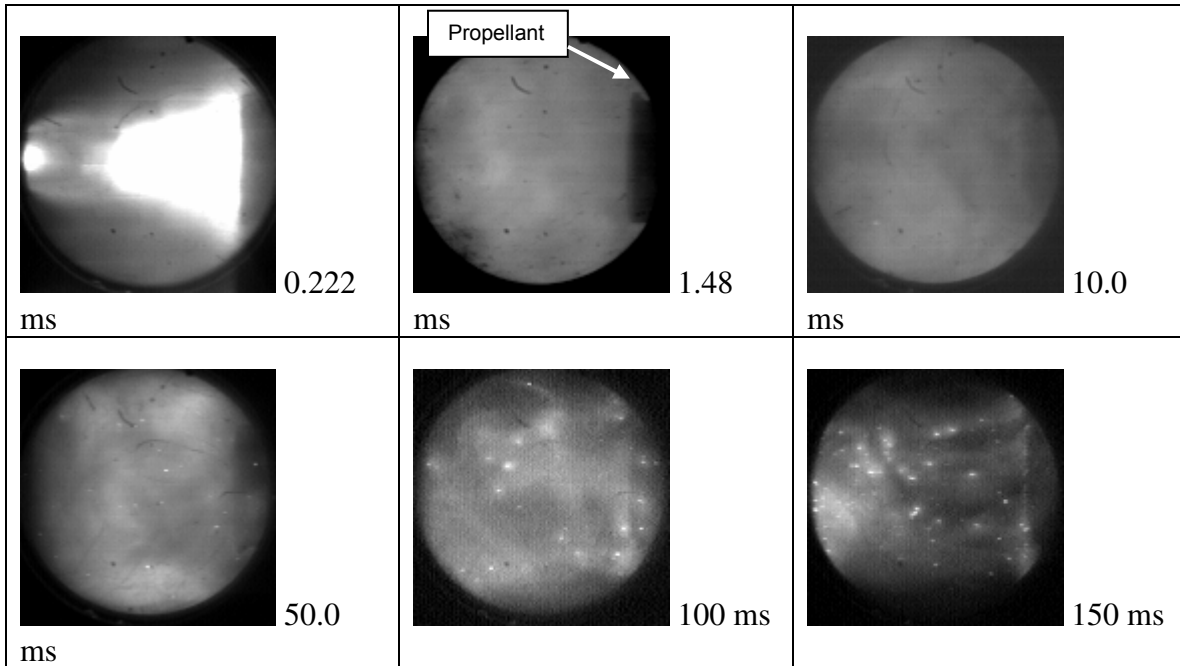


Figure B3: Visible-luminosity images during plasma-ignition of JA-2. The images were acquired at a framing rate of 13,500 frames per second.

In addition to high speed video, pressure measurements were taken during plasma ignition of the propellant inside the original chamber. Runs with the propellant at distances of 23, 10, and 4 mm from the jet exit are shown in Fig. B4. The capacitor was charged to 4 kV in all three runs. The initial pressure spike, between 200 – 300 psi at a delay of 150-250 μ s in all three runs, is due to the plasma jet and gasification of the propellant. The propellant does not burn during this time, but material is photolyzed and pyrolyzed to form gaseous decomposition products that increase the pressure beyond that of the plasma alone. The pressure reduces quickly as the plasma cools, and reaches a minimum around 50 ms for the two higher separation distances. This minimum marks propellant ignition, after which chamber pressure increases again as self sustaining burning begins.

The initial pressure spike is larger when the propellant is closer to the jet exit. This indicates a larger amount of propellant vaporized by the plasma jet as a result of the higher heat flux from the plasma to the propellant. However, this increased initial pressure does not affect ignition time. For the runs shown ignition time doubles for the shortest standoff distance while it would be expected to decrease for higher pressure. In all tests inside the pressure chamber, the propellant ignites long after the plasma is finished discharging. The propellant does not burn as the plasma cools because the sharp reduction in heat transfer to the propellant over such a short time impairs the self-sustaining dissociation to gas-phase reaction to surface heat transfer cycle necessary for burning. Instead, the hot and pressurized exhaust gases circulating through the chamber for tens of milliseconds after the plasma jet ignite the propellant.

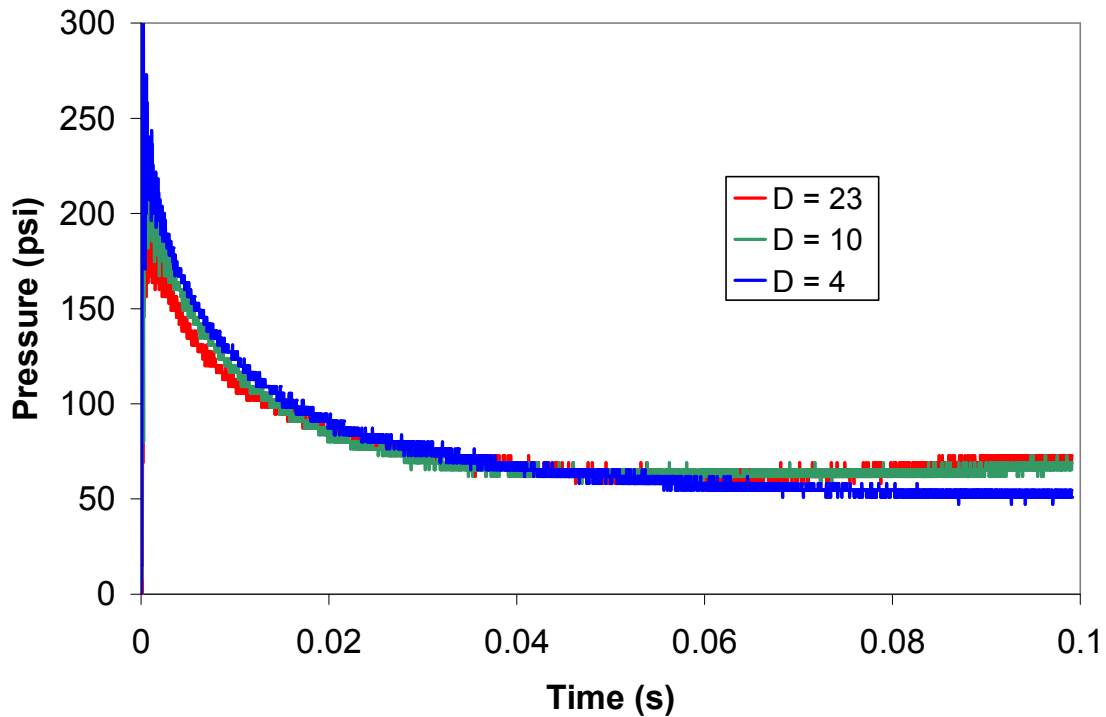


Figure B4: Pressure measurements inside the original chamber while plasma ignites the propellant.

OH PLIF imaging was attempted in the closed chamber to study the ignition of the propellant after interaction with the plasma. OH is a common reaction zone marker in combustion. However, no fluorescence signal could be detected during propellant ignition. A He-Ne laser beam was aimed through the chamber and the spot it produced on a card was imaged with the high speed camera. It was observed that the spot disappeared a few milliseconds after the plasma pulse and did not return for hundreds of milliseconds later. The extinction occurred both with and without propellant in the chamber. This is the same phenomenon seen in Fig. B3 when the surface of the rod is no longer visible. In an effort to reduce the ignition time to below that of when these particulates form, spacers were designed to fill most of the chamber volume. These are shown in Fig. B2. The hope

was that the higher pressures attained with a smaller volume would cause the propellant to ignite during the plasma discharge.

Some example pressure traces with the spacer installed can be seen in Fig. B5. The chamber seals were poorly designed so the maximum pressures reached and the ignition time varied from shot to shot. With the 5 cm³ chamber volume and the 3 mm standoff distance the ignition time was reduced below 12 ms regularly. However, it never reached the 600 μs that marks the end of the plasma discharge, and rarely was below 5 ms. All the pressure curves exhibit the initial pressure spike of the plasma/propellant interaction, followed by rapid decay of the plasma cooling and then subsequent pressure increase marking propellant ignition characteristic of a low energy, short duration electrothermal plasma.

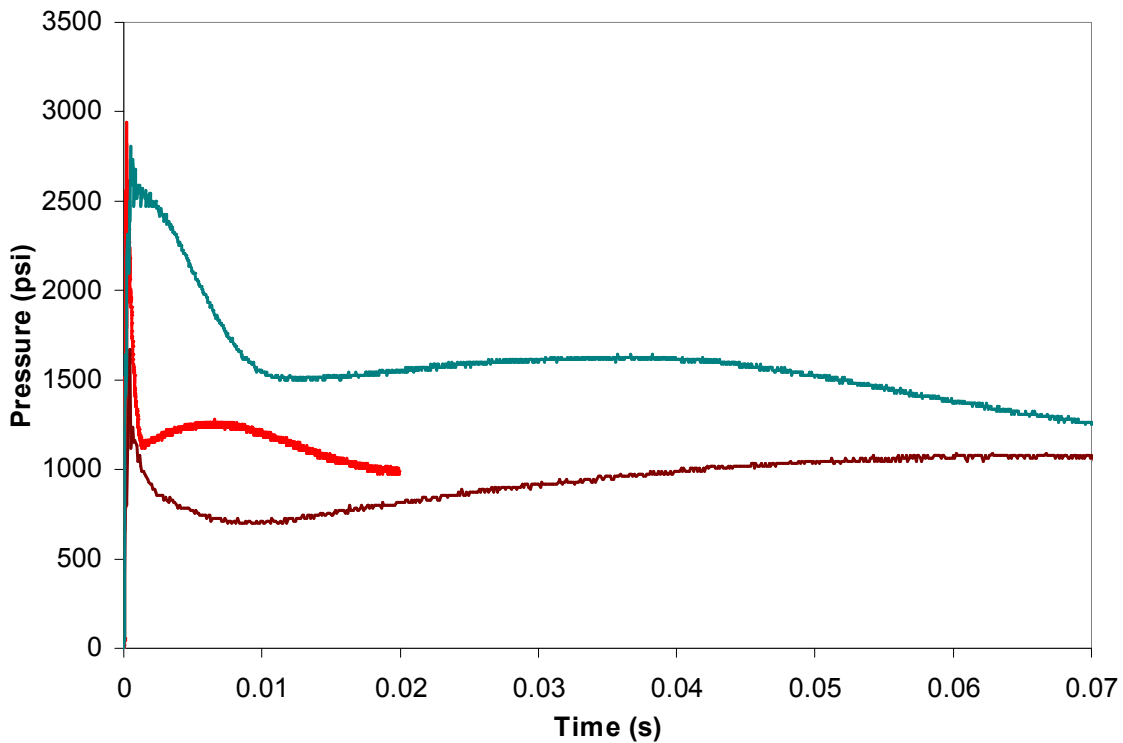


Figure B5: Example pressure traces during plasma ignition in 5 cm³ chamber.

It was discovered that with the reduction in chamber volume, the chamber became optically thick (measured by He-Ne attenuation) before 1 ms. This made it impossible for laser diagnostics inside the chamber after the plasma, and the background luminosity of the plasma itself makes it extremely difficult for laser diagnostics during the plasma. Much effort was spent modifying the chamber and plasma production mechanism to try and increase the time before condensation. However, none of the changes were effective.

The changes are noted in Table B1.

Change Made	Desired Effect
Teflon capillary	Reduce Carbon percentage in plasma
Zinc fuse wire	Increase condensation time due to lower boiling temperature
Pure Tungsten electrodes	Reduce ablation from electrodes
Increase capacitor voltage to 5 kV	Reduce ignition time further
Larger Inductor	Jet plasma longer to decrease ignition time and increase condensation time
Recess windows	Decrease or eliminate deposition on windows to allow longer optical access

Table B1: Changes made to create window of time where optical diagnostics was possible.

Appendix C: NO₂ PLIF

NO₂ planar laser induced fluorescence was attempted during the plasma radiation-propellant interaction using the same experimental setup as the NO fluorescence except with a different pump beam. Nitrogen dioxide is one of the first decomposition products of a nitrate ester propellant. NO₂ has a broadband visible absorption spectrum with four electronic states directly or indirectly interacting along with a complicated vibrational and rotational band structure (Hsu et al. 1978). This qualitative experiment was designed to record the time and place of any NO₂ in the flow. NO₂ was pumped using the same frequency doubled Spectra Physics Nd:YAG at 532 nm mentioned earlier. The ~100 mJ per pulse laser was apertured to 5 mm high and formed into a sheet by a 225 mm convex cylindrical lens. The broadband fluorescence was imaged with the PI-Max ICCD through an OG-570 color glass filter to cut out laser scattering.

NO₂ was not detected during the plasma propellant radiation interaction. Figure C1 shows an example NO₂ PLIF image taken at 200 μs. Scattering of large particles, as well as probable scattering from edge structures can be seen in the image. Also, the bulbous very bright structure in the center at the propellant surface is most likely scattering as well. NO₂ was unlikely to be observed because it is a broadband absorber. Pumping with a narrowband laser produces low fluorescence yields. Because propellant surface luminosity and particle scattering is very bright, it would be difficult to distinguish the expectedly small fluorescence signal from the former phenomena. In addition, NO₂ usually quickly dissociates into NO during nitrate ester decomposition in atmospheric pressure air (Oyumi and Brill 1986). It is probable that NO₂ does not appear below the propellant surface because it has dissociated into NO before exiting the propellant.

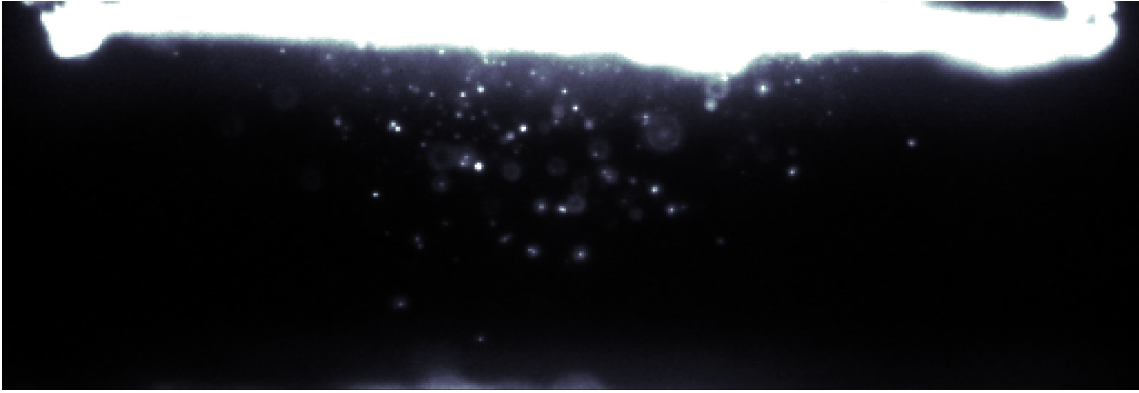


Figure C1: Example NO₂ PLIF image at 200 μ s.

References

- Anderson, R., Fickie, K. "IBHVG2 – A User's Guide," BRL-TR-2829, U.S. Army Ballistic Research Laboratory, Aberdeen Proving Ground, MD, July 1987
- Ashkenazy, J., Kipper, R., Caner, M., "Spectroscopic Measurements of Electron Density of Capillary Plasma Based on Stark Broadening of Hydrogen Lines," *Physical Rev. A*, vol. 43, p. 5568, May 1991
- Bekefi, G., *Principles of Laser Plasmas*, Wiley, New York, 1976
- Bekefi, G., *Radiation Processes in Plasmas*, John Wiley and Sons, New York, 1966, p. 41
- Beyer, R. Pesce-Rodriguez, R., "The Response of Propellants to Plasma Radiation," ARL-TR-3189, U.S. Army Research Laboratory, Aberdeen Proving Ground, MD, June 2004
- Beyer, R., Pesce-Rodriguez, R., "Experiments to Define Plasma-Propellant Interactions," *IEEE Trans. Magnetics*, vol. 39, Jan. 2000, p. 207
- Birk, A., Del Guercio, M., Kinkennon, A., Kooker, D., Kaste, P., "Interrupted-Burning Tests of Plasma-Ignited JA2 and M30 Grains in a Closed Chamber," *Propellants, Explosives, Pyrotechnics*, vol. 25, 2000, p. 133
- Bourham, M., Gilligan, J., Oberle, W., "Analysis of Solid Propellant Combustion Behavior Under Electrothermal Plasma Injection for ETC Launchers," *IEEE Trans. Magnetics*, vol. 33, Jan. 1997, p. 278
- Bussiere, W., Duffour, E., Andre, P., Pellet, R., Brunet, L., "Experimental Assessment of Temperature in Plasma Wall Interaction," *Eur. Phys. J. D*, vol. 28, 2004, p. 79
- Caillard, J., Izarra, C., Brunet, L., Vallee, O., Gillard, P., "Assessment of the Blast Wave Generated by a Low-Energy Plasma Igniter and Spectroscopic Measurements," *IEEE Trans. Magnetics*, vol. 39, Jan. 2003, p. 212
- Clark, D.T. Stephenson, P.J., "An ESCA Study of the Surface Chemistry of Cellulose Nitrates and Double Based Propellants, with Particular Reference to their

- Degradation in Ultra-violet Light,” *Polymer Degradation and Stability*, vol. 4, 1983, p. 185
- Das, M., Thynell, S.T, Li, J., Litzinger, T.A., “Transient Radiative Heat Transfer from a Plasma Produced by a Capillary Discharge,” *J. Thermophysics and Heat Transfer*, vol. 19, no. 4, Oct. 2005, p. 572
- Davidson, J.E., Beckstead, M.W., “Improvements to Steady-State Combustion Modeling of Cyclotrimethylenetrinitramine,” *J. Propulsion and Power*, v. 13, no. 3, 1997, p. 375
- Del Guercio, M., Stobie, I., Oberle, W., “The Effect of Delayed Plasma Injection on the Combustion Characteristics of Solid JA2 Propellant,” ARL-MR-322, U.S. Army Research Laboratory, Aberdeen Proving Ground, MD, July 1996
- Deluca, L., Caveny, L.H., Ohlemiller, T.J., Summerfield, M., “Radiative Ignition of Double-Base Propellants: I. Some Formulation Effects,” *AIAA Journal*, vol. 14, n. 8, Aug. 1976, p. 940
- Deluca, L., Caveny, L.H., Ohlemiller, T.J., Summerfield, M., “Radiative Ignition of Double-Base Propellants: II. Pre-ignition Events and Source Effects,” *AIAA Journal*, vol. 14, n. 8, Aug. 1976, p. 1111
- Edwards, C.M., Bourham, M.A., Gilligan, J.G., “Experimental Studies of the Plasma-Propellant Interface for Electrothermal-Chemical Launchers,” *IEEE Trans. Magnetics*, vol. 31, p.404, Jan. 1995
- Eisenreich, N., Fischer, T.S., Langer, G., Kelzenberg, S., Weiser, V., “Burn Rate Models for Gun Propellants,” *Propellants, Explosives, Pyrotechnics*, v. 27, 2002, p. 142
- Fifer, R., Sagan, E., Beyer, R., “Chemical Effects in Plasma Ignition,” *IEEE Trans. Magnetics*, vol. 39, Jan. 2003, p. 218
- Fifer, R.A., “Chemistry of Nitrate Ester and Nitramine Propellants,” *Fundamentals of Solid-Propellant Combustion*, Progress in Astronautics and Aeronautics, v. 90, K. Kuo and M. Summerfield ed., 1984
- Fujimoto, T., McWhirter, R.W.P., “Validity Criteria for Local Thermodynamic Equilibrium in Plasma Spectroscopy,” *Physical Rev. A*, vol. 42, no. 11, p. 6588, 1990
- Gigosos, M.A., Cardenoso, V., “New Plasma Diagnosis Tables of Hydrogen Stark Broadening Including Ion Dynamics,” *J. Phys. B*, vol. 29, no. 2, 1996, p. 10
- Gilligan, J.G., Mohanti, R.B., “Time-Dependent Numerical Simulation of Ablation Controlled Arcs,” *IEEE Trans. Plasma Sci.*, vol. 18, p. 190, April 1990

- Greig, J., Earnhart, J., Winsor, N., McElroy, H., "Investigation of Plasma-Augmented Solid Propellant Interior Ballistic Processes," IEEE Trans. Magnetics, vol. 29, Jan. 1993, p. 555
- Griem, H.R., *Principles of Plasma Spectroscopy*, Cambridge University Press, Cambridge, 1997, p.225
- Hankins, O.E., Bourham, M., Mann, D., "Observations of Visible Light Emission from Interactions Between an Electrothermal Plasma and a Propellant," IEEE Trans. Magnetics, vol. 33, Jan, 1997, p. 295
- Hankins, O.E., Bourham, M.A., Earnhart, J., Gilligan, J.G., "Visible Light Emission Measurements From a Dense Electrothermal Launcher Plasma," IEEE Trans. Magnetics, vol. 29, Jan. 1993, p. 1158
- Hankins, O.E., Mann, D., "Analyses of Molecular and Neutral Atomic Emission Spectra from an Electrothermal Launcher Plasma," IEEE Trans. Magnetics, vol. 31, p. 410, Jan. 1995
- Hanson, R.K., Seitzman, J.M., and Paul, P.H., "Planar Laser-Fluorescence Imaging of Combustion Gases," Appl. Phys. B, v. 50, no. 6, 1990, p. 441
- Harilal, S.S., Bindhu, C.V., Issac, R.C., Nampoore, V.P.N., Vallabhan, C.P.G., "Electron Density and Temperature Measurements in a Laser Produced Carbon Plasma," J. Appl. Phys., vol. 82, no. 5, P. 2143, 1997
- Hermance, C., "Solid-Propellant Ignition Theories and Experiments," Fundamentals of Solid-Propellant Combustion, Progress in Astronautics and Aeronautics, v. 90, K. Kuo and M. Summerfield ed., 1984
- Hewkin, D., Figura, E., "Fundamental Research and Numerical Modeling of the Internal Ballistics of Electrothermal Chemical Guns," IEEE Trans. Magnetics, vol. 29, p. 561, Jan. 1993
- Hsu, D.K., Monts, D.L., Zare, R.N., *Spectral Atlas of Nitrogen Dioxide 5530 to 6480 Å*, Academic Press, New York, 1978
- Hurley, J.D., Bourham, M.A., Gilligan, J.G., "Numerical Simulation and Experiment of Plasma Flow in the Electrothermal Launcher SIRENS," IEEE Trans. Magnetics, vol. 31, p. 616, Jan. 1995
- Kaplan, Z., Melnik, D., Sudai, M., Plotnik, D., Appelbaum, G., Kimhe, D., Alimi, R., Perlmutter, L., "A Field Study of a Hypervelocity Solid Propellant Electrothermal 105 mm Launcher," IEEE Trans. Magnetics, vol. 31, Jan. 1995, p. 425

- Kaplan, Z., Saphier, D., Melnik, D., Gorelic, Z., Ashkenazy, J., Sudai, M., Kimhe, D., Melnik, M., "Electrothermal Augmentation of a Solid Propellant Launcher," IEEE Trans. Magnetics, vol. 29, Jan. 1993, p. 573
- Kappen, K. Beyer R., "Progress in Understanding Plasma-Propellant Interaction," Propellants, Explosives, Pyrotechnics, vol. 28, no. 1, 2003, p. 32
- Kappen, K., Bauder, U.H., "Calculation of Plasma Radiation Transport for Description of Propellant Ignition and Simulation of Interior Ballistics in ETC Guns," IEEE Trans. Magnetics, vol. 37, p. 169, Jan. 2001
- Kappen, K., Bauder, U.H., "Simulation of Plasma Radiation in Electrothermal-Chemical Accelerators," IEEE Trans. Magnetics, vol, 35, p. 192, Jan 1999
- Kaste, P., Birk, A., Kinkennon, A., Lieb, R., Del Guercio, M., Schroeder, M., Pesce-Rodriguez, R., "Analysis of Burning Rate Phenomena and Extinguished Solid Propellants from an Interrupted Closed Bomb with Plasma Igniter," IEEE Trans. Magnetics, vol. 37, Jan. 2001, p. 173
- Kaste, P., Kinkennon, A., Lieb, R., Birk, A., Del Guercio, M., Newberry, J., Schroeder, M., Pesce-Rodriguez, R., "Surface Phenomena of Solid Propellants Ignited by Plasma," ARL-TR-2500, U.S. Army Research Laboratory, Aberdeen Proving Ground, MD, May 2001
- Kaste, P., Kinkennon, A., Pesce-Rodriguez, R., Del Guercio, M., Birk, A., Devynck, D., Howard, S., Schroeder, M., Newberry, J., "Characterization of Extinguished Solid Propellants from an Interrupted Closed Bomb with Plasma Igniter," ARL-TR-2036, U.S. Army Research Laboratory, Aberdeen Proving Ground, MD, Aug. 1999
- Kaste, P., Pesce-Rodriguez, R., Schroeder, M., Katulka, G., White, K., Leadore, M., Kinkennon, A., "Chemical Characterization of Plasma-Treated Solid Gun Propellants," ARL-TR-1798, U.S. Army Research Laboratory, Aberdeen Proving Ground, MD, Sept. 1998
- Katulka, G., White, K., Oberle, W., Kaste, P., Pesce-Rodriguez, R., Leadore, M., "Experimental Characterization of Plasma Effects on Energetic Materials for Electrothermal Chemical Launch Applications," IEEE Trans. Magnetics, vol. 35, Jan. 1999, p. 197
- Katulka, G.L., Oberle, W.F., Wren, G.P., Okamitsu, J., Neale, A.M., "Pulsed-Power and High Energy Plasma Simulations for Application to Electrothermal-Chemical Guns," IEEE Trans. Magnetics, v. 33, no. 1, Jan. 1997

- Kim, J., Clemens, N.T., Varghese, P.L., "Experimental Study of the Transient Underexpanded Jet Generated by Electrothermal Capillary Plasma," *J. Propulsion and Power*, vol. 18, no. 6, 2002
- Kimura, J., "Chemiluminescence Study on Thermal Decomposition of Nitrate Esters (PETN and NC)," *Propellants, Explosives, Pyrotechnics*, vol. 14, 1989, p. 89
- Kimura, J., "Kinetic Mechanism on Thermal Degradation of a Nitrate Ester Propellant," *Propellants, Explosives and Pyrotechnics*, 13, 1988, p. 8
- Kohel, J.M., Su, L.K., Clemens, N.T., Varghese, P.L., "Emission Spectroscopic Measurements and Analysis of a Pulsed Plasma Jet," *IEEE Trans. Magnetics*, vol. 35, p. 201, Jan 1999
- Koleczko, A., Ehrhardt, W., Kelzenberg, S., Eisenreich, N., "Plasma Ignition and Combustion," *Propellants, Explosives, Pyrotechnics*, vol. 26, 2001, p. 75
- Kovesi, P., "Phase Preserving Denoising of Images," *The Australian Pattern Recognition Society Conference: DICTA'99*, Dec. 1999. Perth WA. pp 212-217
- Kubota, N., "Survey of Rocket Propellants and their Combustion Characteristics," *Fundamentals of Solid-Propellant Combustion, Progress in Astronautics and Aeronautics*, v. 90, K. Kuo and M. Summerfield ed., 1984
- Kukhlevsky, S.V., Kaiser, J., Samek, O., Liska, M., Erostyak, J., "Stark Spectroscopy Measurements of Electron Density of Ablative Discharges in Teflon-(CF₂)n Capillaries," *J. Phys. D: Appl. Phys.*, vol, 33, p. 1090, 2000
- Lachney, E.R., "Two-Dimensional Temperature and Pressure Imaging of a Supersonic Flat Plate Wake," *Master's Thesis, Aerospace Engineering, University of Texas at Austin*, 1995
- Lengelle, G., Duterque, J., Trubert, J.F., "Physico-Chemical Mechanisms of Solid Propellant Combustion," *Solid Propellant Chemistry, Combustion, and Motor Interior Ballistics*, *Progress in Astronautics and Aeronautics*, vol. 185, V. Yang, T. Brill, W. Ren ed., 2000
- Levin, M., Marcus, G., Pukhov, A., Zigler, A., Sasorov, P., "High-Current Capillary Discharge with Prepulse Ablative Plasma," *J. Appl. Phys.*, vol. 93, no. 2, 2003, p. 851
- Li, B., Li, H., "Discussion on Emission Spectroscopy Measurements from a Dense Electrothermal Launcher Plasma," *19th Int. Symposium of Ballistics*, May 2001, p. 203

- Li, J., Das, M., Litzinger, T.A., Thynell, S.T., "Normal Impingement of Electrothermal Plasma on Solid Propellants," 41st AIAA/ASME/SAE/ASEE Joint Propulsion Conference and Exhibit, July 2005, Tucson, Arizona, AIAA 2005-3975
- Li, J., Litzinger, T.A., Thynell, S.T., "Interaction of Capillary Plasma with Double-Base and Composite Propellants," J. Propulsion and Power, vol. 20, no. 4, Aug. 2004, p. 675
- Li, J., Litzinger, T.A., Thynell, S.T., "Plasma Ignition and Combustion of JA2 Propellant," J. Propulsion and Power, vol. 21, no. 1, Jan. 2005, p. 44
- Lieb, R., Gillich, C., "Morphology of Extinguished Monolithic JA2 Grains Fired in a 30-mm Solid Propellant Electrothermal-Chemical (SPETC) Gun," ARL-TR-606, U.S. Army Research Laboratory, Aberdeen Proving Ground, MD, Nov. 1994
- Lieb, R., Kaste, P., Birk, A., Kinkennon, A., Pesce-Rodriguez, R., Schroeder, M., Del Guercio, M., "Analysis of Burning Rate Phenomena and Extinguished Solid Propellants from an Interrupted Closed Bomb with Plasma Igniter," ARL-TR-2561, U.S. Army Research Laboratory, Aberdeen Proving Ground, MD, Aug. 2001
- Loeb A., Kaplan, Z., "A Theoretical Model for the Physical Processes in the Confined High Pressure Discharges of Electrothermal Launchers," IEEE Trans. Magnetics, vol. 25, p. 32, January 1989
- Mauck, M., "Knife Edge Profiling of a Q-Switched Nd:YAG Laser Beam and Waist," Appl. Optics, v. 18, n. 5, 1979, p. 599.
- Miller, M.S., Anderson, W.R., "Burning-Rate Predictor for Multi-Ingredient Propellants: Nitrate-Ester Propellants," J. Propulsion and Power, v. 20, No. 3, May-June 2004
- Miller, M.S., Anderson, W.R., "Energetic-Material Combustion Modeling with Elementary Gas-Phase Reactions: a Practical Approach", Ch. 2.12, *Solid Propellant Chemistry, Combustion, and Motor Interior Ballistics*, v. 185, 2000, p. 501
- Mohanti, R.B., Gilligan, J.G., Bourham, M.A., "Time-dependent Simulation of Weakly Nonideal Plasmas in Electrothermal Launchers," Phys. Fluids B, vol 3, p. 3046, Nov. 1991
- Nalty, K.Z., Zowarka, R.C., and Holland, L.D., "Instrumentation for EM Launcher Systems, IEEE Transactions on Magnetics, vol. 20, no. 2, March 1984
- Nusca, M.J., McQuaid, M.J., Anderson, W.R., "Development and Validation of a Comprehensive Model of the Plasma Jet Generated by an Electrothermal

- Chemical Igniter,” 19th International Symposium of Ballistics, May 2001, Interlaken, Switzerland
- Oberle, W., Kooker, D., “BRLCB: A Closed-Chamber Data Analysis Program,” ARL-TR-36, U.S. Army Research Laboratory, Aberdeen Proving Ground, MD, Jan. 1993
- Oberle, W., White, K., “The Application of Electrothermal-Chemical (ETC) Propulsion Concepts to Reduce Propelling Charge Temperature Sensitivity,” ARL-TR-1509, U.S. Army Research Laboratory, Aberdeen Proving Ground, MD, Spt. 1997
- Oberle, W., Wren, G., “Methods for Determining Burning or Gas Generation Rates of Plasma-Augmented Propellants with Applications to Electrothermal-Chemical (ETC) Guns,” IEEE Trans. Magnetics, vol. 31, Jan. 1995, p. 435
- Ohlemiller, T.J., Summerfield, M., “A Critical Analysis of Arc Image Ignition of Solid Propellants,” AIAA Journal, vol. 6, n. 5, May 1968, p. 878
- Oyumi, Y., Brill, T.B., “Thermal Decomposition of Energetic Materials 14. Selective Product Distributions Evidenced in Rapid, Real-Time Thermolysis of Nitrate Esters at Various Pressures,” Combustion and Flame, vol. 66, 1986, p. 9
- Pesce-Rodriguez, R., Beyer, R., Kinkennon, A., Del Guercio, M., Kaste, P., Newberry, J., “In-Depth Chemistry in Plasma-Exposed M30 and JA2 Gun Propellants,” ARL-TR-2505, U.S. Army Research Laboratory, Aberdeen Proving Ground, MD, June 2001
- Peterson, R.R., Moses, G.A., “MIXERG – An Equation of State and Opacity Computer Code,” Computer Physics Communications, Vol. 28, p. 405, 1983
- Powell, J.D., Zielinski, A.E., “Theory and Experiment for an Ablating-Capillary Discharge and Application to Electrothermal-Chemical Guns,” BRL-TR-3355, U.S. Army Ballistic Research Laboratory, Aberdeen Proving Ground, MD, June 1992
- Prasad, K., Yetter, R.A., Smooke, M.D., “An Eigenvalue Method for Computing the Burning Rates of RDX Propellants:,” Combustion, Science and Technology, v. 124, 1997, p. 35
- Proud, W., Bourne, N., “The Electrothermal Enhancement of Propellant Burning by Plasma Injection,” Propellants, Explosives, Pyrotechnics, vol. 22, 1997, p. 212
- Roos, B.D., Brill, T.B., “Thermal Decomposition of Energetic Materials 82. Correlations of Gaseous Products with the Composition of Aliphatic Nitrate Esters,” Combustion and Flame, vol. 128, 2002, p. 181

- Sakthivel, N., Bhattacharya, R., Chaturvedi, S., "Improved Opacity Calculations and Radiation Transport Modeling for ETC Plasma Cartridges," 12th IEEE International Pulsed Power Conference, Digest of Technical Papers, 1999
- Sakthivel, N., Chaturvedi, S., "Opacity Calculations for Dense Plasmas," *Contrib. Plasma Phys.*, vol. 41, p. 335, 2001
- Sandolache, G., Fleurire, C., Bauchire, J., Gentils, F., Zoita, V., "Determination of the Parameters of a Plasma JET Generated by a Capillary Discharge," *Nukleonika*, vol. 46, 2001, p. S21
- Seitzman, J.M., "Lines," "Spectra," Version 3.0, High Temperature Gasdynamics Laboratory, Mech. Engin. Dept., Stanford University, ©1985-1990
- Sueda, T., Katsuki, S., Akiyama, H., "Early Phenomena of Capillary Discharges in Different Ambient Pressures," *IEEE Trans. Magnetics*, vol. 33, Jan. 1997, p. 334
- Sun, J., Lv, Y., Wang, Y., Feng, G., "Simulation and Research of One-Dimensional Coupling Model of Solid Propellant Electrothermal-Chemical Gun," *IEEE Trans. Magnetics*, v. 41, no. 1, Jan. 2005
- Taylor, M., "Ignition of Propellant by Metallic Vapour Deposition for an ETC Gun System," *Propellants, Explosives, Pyrotechnics*, vol. 26, 2001, p. 137
- Taylor, M.J., "Measurement of the Properties of Plasma from ETC Capillary Plasma Generators," *IEEE Trans. Magnetics*. Vol. 37, Jan. 2001, p. 194
- Taylor, M.J., "Plasma Propellant Interactions in an Electrothermal-Chemical Gun," PhD Thesis, Cranfield University, Royal Military College of Science, Sept. 2002
- Tian, X., Tang, B., and Chu, P.K., "Accurate Determination of Pulsed Current Waveform in Plasma Immersion Ion Implantation Processes." *Journal of Applied Physics*, vol. 86, no. 7, Oct. 1999
- Tsakiris, G.D., Eidmann, K., "An Approximate Method for Calculating Planck and Rosseland Mean Opacities in Hot, Dense Plasmas," *J. Quantitative Spectroscopy and Radiative Transfer*, vol. 38, p. 353, 1987
- van der Mullen, J.A.M., Benoy, D.A., Fey, F.H.A.G., van der Sidje, B., "Saha Equation for Two Temperature Plasmas: Theories, Experimental Evidence, and Interpretation," *Physical Rev. E*, vol. 50, p. 3925, 1994
- Ward, D.A., La, J., Exon, T., "Using Rogowski Coils for Transient Current Measurements," *IEEE Engineering Science and Education Journal*, vol. 2, June 1993

- White, K., Oberle, W., Juhasz, A., Stobie, I., Nekula, K., Katulka, G., Driesen, S., "Electrothermal-Chemical (ETC) Propulsion with High Loading Density Charges," ARL-TR-845, U.S. Army Research Laboratory, Aberdeen Proving Ground, MD, Aug. 1995
- White, K., Stobie, I., Oberle, W., Katulka, G., Driesen, S., "Combustion Control Requirements in High Loading Density, Solid Propellant ETC Gun Firings," IEEE Trans. Magnetics, vol. 33, Jan. 1997, p. 350
- Williams, A. White, K., "Plasma-Propellant Interactions Studies: Measurements of Heat Flux Produced by Hydrocarbon Ablation-Supported Plasmas," IEEE Trans. Magnetics, vol. 37, Jan. 2001, p. 203
- Wilson, D.E., Kim, K., Raja, L.L., "Theoretical Analysis of an External Pulsed Plasma Jet," IEEE Transactions on Magnetics, v. 35, n. 1 Jan. 1999
- Woodley, C., Fuller, S., "Apparent Enhanced Burn Rates of Solid Propellants Due to Plasmas," Proceedings 16th International Symposium on Ballistics, San Francisco, Sept. 1996, p. 153
- Woodley, C.R., Billett, S.J., "Modeling Enhanced Gas Generation Rates in a 155-mm ETC Gun," IEEE Trans. Magnetics, v. 37, Jan. 2001
- Wren, G.P., Oberle, W.F., Hosangadi, A., "Influence of Radiation on Grain Heating in ETC Closed Chambers," IEEE Trans. Magnetics, v. 35, no.1, Jan. 1999
- Yang, M., Ramsey, J.M., Kim, B.J., "Laser-induced Selective Dissociation of Nitro Groups in Nitrocellulose," Rapid Communications in Mass Spectrometry, vol. 10, 1996, p. 311
- Zaghloul, M.R., Bourham, M.A., Doster, J.M., "Semi-analytical modeling and simulation of the evolution and flow of Ohmically-heated non-ideal plasmas in Electrothermal Guns," J. Phys. D: Appl. Phys. v. 34, 2001, p. 772
- Zel'dovich, Ya.B., Raizer, Yu.P., *Physics of Shock Waves and High Temperature Hydrodynamic Phenomena*, Academic Press, New York, 1966

Vita

Michael David Ryan was born in Durham, NC on June 27th, 1978 to David and Carol Ryan. He spent most of his childhood in Cincinnati, OH and graduated from Sycamore High School there in 1996. He attended the University of Florida from 1996-2000 and received a Bachelors of Science in Mechanical Engineering there in May, 2000. In July, 2000 he moved to Austin, TX to attend graduate school at the University of Texas at Austin. For the past six years he has been attending classes and working as a graduate research assistant in the Aerospace Engineering department. With this degree he is moving to Dayton, OH to begin a post-doc position at Air Force Research Labs.

Permanent address: 4782 Horseshoe Bend, Batavia, OH 45103

This dissertation was typed by the author.